Experimental Investigation of the Heat Flux from Laminar Premixed Ethanol/Air and Hydrogen/Ethanol/Air Flames to Walls Using Thermographic Phosphors

Von der Fakultät für Ingenieurwissenschaften

Abteilung Maschinenbau und Verfahrenstechnik

der

Universität Duisburg-Essen

zur Erlangung des akademischen Grades

Doktor-Ingenieur

genehmigte Dissertation

von

Mohammed Ahmed Alkhader Mohammed

aus

Aden / Jemen

Referent: Prof. Dr. rer. nat. Burakl Atakan
Korreferent: Prof. Dr.-Ing. Ernst von Lavante

Tag der mündlichen Prüfung: 15.12.2014

Abstract

Premixed impinging flame jets have been widely used in both industrial and domestic applications because of their advantages in offering high heat transfer rates and simple handling. Nevertheless, for the process of flame impingement on walls, the interaction between the combustion process and heat transfer to the wall is also not sufficiently understood, thus many of the impingement heating systems are not utilized at optimal conditions. In addition, the fuels used in previous work concentrate almost exclusively on methane or natural gas, while other important fuels like ethanol or hydrogen were rarely or never investigated. Furthermore, most recent studies focus on only one geometry, flame impingement normal to a flat surface. Therefore, there is little work on ethanol / air flames that strike normally or at an angle to flat surfaces. Moreover, investigations on ethanol/air flames impinging normally on cylindrical surface have not been reported yet.

In this experimental study, the thermographic phosphor method was implemented to study the heat flux at the stagnation point on the impingement surface. For that purpose, light emitting diodes (LED) were used to excite the phosphorescence of sol-gel deposited chromium-doped alumina (Cr_3:Al_2O_3, ruby) on both sides of solid walls in different experiments. The phosphorescence lifetimes depend on temperature, so they were evaluated to extract the impingement surface temperatures. The heat fluxes were calculated using a one-dimensional conduction equation. Laminar premixed flames that were investigated are ethanol-air flames and hydrogen-ethanol-air flames. The burner exit diameter is 30 mm. Three different types of configurations were studied for impinging flames. These are flame impinging upwards normally on a flat surface, flame striking at different angles on a flat surface and flames impinging upwards normally on cylindrical surfaces (Tube).

In the case of ethanol/air flames impinging normally on a flat surface, the following parameters were investigated: impingement surface thermal conductivity, cold gas

velocity of the air/fuel jet, equivalence ratio of the air/fuel jet, surface-to-burner distance, oxygen amount in oxidizer and enrichment of the mixture ethanol/air with hydrogen. It was found that using zirconia as an impingement surface material instead of alumina under identical operational conditions reduces the heat flux measurement errors from approximately 13% to 2.3%. In a stoichiometric condition, the experimental results were compared with simulated results. It was observed that the results obtained experimentally have smaller values than those obtained from simulation. The highest heat flux was obtained at the equivalence ratio of 1.0. The lowest heat flux was obtained at the lowest applied equivalence ratio of 0.75. The heat flux increased when the plate-to-burner distance was decreased. The use of an oxidizer with a lower percentage of nitrogen than in air enhanced the heat flux. Also, it was found that when hydrogen volume fraction increases, the heat flux increases, and this effect is more significant at high cold gas velocity.

In the investigation of the angle dependent heat flux on the flat plat of stoichiometric ethanol/air flames, it was found that the heat flux in the decreased as the inclination angle was reduced. The maximum heat flux was obtained at the inclination angle of 90°.

In comparison to heat transfer to flat plates, in heat transfer to cylindrical surfaces higher heat fluxes are found. In almost all experimental results, the measured heat flux indicates the change of the flame stabilization mechanism from a burner stabilized to a stagnation plate stabilized flame with increasing cold gas velocity.

Zusammenfassung

Vormischflammen werden zum Heizen sowohl industriell als auch iin Privathaushalten vielfältig eingesetzt. Ihre Vorteile liegen in einer hohen Wärmeübertragungsrate und einer einfachen Handhabung. Dennoch ist der Prozess der der Wechselwirkung zwischen Verbrennungsprozess und Wärmeübertragung an die Wand weiterhin nicht ausreichend verstanden, weswegen die meisten Anwendungen nicht unter den günstigsten Bedingungen betrieben werden. Hinzu kommt, dass sich frühere Arbeiten fast ausschließlich mit der Verbrennung von Methan oder Erdgas, hingegen andere wichtige Brennstoffe wie Ethanol oder Wasserstoff selten oder gar nicht untersuchtwurden. Desweiteren befassen sich die meisten bisherigen Studien mit einer eingeschränkten Geometrie, der senkrechten Strömung der Flamme auf eine ebene Oberfläche. Daher gibt es kaum Arbeiten zu Ethanol/Luft-Flammen, die in verschiedenen Winkeln auf eine ebene Oberfläche treffen. Untersuchungen zum Auftreffen einer Ethanol/Luft-Flamme auf eine gekrümmte Oberfläche sind bisher nicht berichtet worden.

In dieser weitgehend experimentellen Arbeit werden thermograpische Phosphore eingesetzt, um die Wärmestromdichte am Staupunkt einer auf eine Oberfläche treffenden Flamme zu untersuchen. Hierzu werden beide Seiten der später durch die Flamme beheizten Oberfläche mit einem dünnen, polykristallinen Rubin-Film im Sol-Gel-Verfahren beschichtet. Die Phosphoreszenz von Rubin (mit Chrom dotierter Korund; Cr_3:Al_2O_3) wird durch Leuchtdioden angeregt. Die Lebensdauer der Phosphoreszenz ist temperaturabhängig, sodass sich hieraus die Oberflächentemperaturen bestimmen lassen. Die Wärmestromdichte kann hieraus unter Annahme eindimensionaler Wärmeleitung ermittelt werden. Laminare, vorgemischte Ethanol/Luft- und Wasserstoff/Ethanol/Luft-Flammen werden hier untersucht, die von unten nach oben brennen und einen darüber befindlichen Probekörper heizen. Der Brennerdurchmesser beträgt 30mm. Es werden drei Geometrien untersucht: Ebene Platte senkrecht zur Flamme, ebene Platte mit

vorgegebenem Winkel zur Flamme sowie zylindrische Rohre senkrecht zur Flamme. Im Falle der senkrecht angeströmten Platte wurden folgende Parameter untersucht: Plattenmaterial mit unterschiedlicher Wärmeleitfähigkeit, Strömungsgeschwindigkeit des Kaltgases, das Brennstoff/Luft-Verhältnis ϕ, der Abstand von Brenner und Platte, der Sauerstoffgehalt des Oxidators und die Zusammensetzung des Brennstoffs durch Zugabe von Wasserstoff zum Ethanol. Es stellte sich heraus, dass der Wechsel des Plattenmaterials von Aluminiumdioxid zu Zirkoniumdioxid den Fehler der Wärmestromdichtenmessungen von 13% auf 2,3% reduziert. Die experimentell bestimmten Wärmestromdichten der stöchiometrischen Verbrennung wurden mit Simulationsergebnissen verglichen wobei die Werte des Experiments unter denen der Modellierung lagen. Die höchste Wärmestromdichte wurde bei einem Äquivalenzverhältnis von 1,0 ermittelt (stöchiometrische Verbrennung) und die niedrigste bei dem niedrigsten gewählten Äquivalenzverhältnis von 0,75. Die Wärmestromdichte erhöhte sich mit abnehmendem Abstand von Brenner zu Platte. Wurde der Stickstoffgehalt der Luft reduziert, so erhöhte sich die Wärmestromdichte ebenfalls. Ebenso konnte die Wärmestromdichte durch Zugabe von Wasserstoff erhöht werden, wobei dieser Effekt bei höheren Strömungsgeschwindigkeiten stärker war.

Zur Untersuchung des winkelabhängigen Wärmeübergangs auf ebene Platten von stöchiometrischen Ethanol/Luft-Flammen zeigte sich eine Abnahme der Wärmestromdichte bei Abnahme des Winkels.

Im Vergleich zu der ebenen Platte zeigen die Messungen am Zylinder eine höhere Wärmestromdichte, wenn die Flamme am Staupunkt stabilisiert ist. In nahezu allen Messreihen ist der Wechsel von einer brennerstabilisierten Flamme zu einer staupunktstabilisierten Flamme bei Erhöhung der Strömungsgeschwindiugkeit zu erkennen.

Acknowledgement

As the formal completion of my doctoral studies in the Department of Thermodynamic is under way, I am very pleased to have the honor to express my gratitude from the pages of my thesis to all those who were involved in this journey in research and applied knowledge.

Initially, it gives me immense pleasure to express my depth of gratitude and respect toward my supervisor Prof. Dr. rer. nat. habil Burak Atakan for giving me an opportunity to work with him and for his excellent supervision, discussions and suggestions.

I am grateful and indebted to Dr. Ulf Bergmann for all his help and his guidance during this research.

I am also grateful to Mr. Andreas Görnt and Mr. Stephan Steinbrink for the technical support. Last, but not least,

I would like to express my gratitude to all my colleagues who made me feel at home with their love, friendship, and care.

Special thanks are also due to my parents, my wife, and my lovely children from whom I always get support and lovely care.

Finally, I acknowledge supports from Deutscher Akademischer Austausch Dienst (DAAD) for the scholarship in the program Research Grants for Doctoral Candidates under the matriculation: A/09/98497.

Dedication

To

My Parents

My Wife

My Children

Table of Contents

List of Figures

List of Figures

List of Figures

List of Figures

List of Tables

1 Introduction

Combustion plays a major role in modern life, especially in domestic and industrial applications. Many industries rely heavily on combustion, as shown in Table (1.1)

	% Total energy from (at the point of use)		
Industry	**Steam**	**Heat**	**Combustion**
Petroleum refining	29.6	62.6	92.2
Forest products	84.4	6.0	90.4
Steel	22.6	67.0	89.6
Chemicals	49.9	32.7	82.6
Glass	4.8	75.2	80.0
Metal casting	2.4	67.2	69.6
Aluminium	1.3	17.6	18.9

Source: U.S. Dept. of Energy, Energy Information Administration as quoted in the industrial combustion vision, prepared by the U.S. Dept. of Energy, May 1998.

Table 1.1: The importance of combustion to industry

The objective in nearly all industrial combustion applications is to transfer the thermal energy, which is produced from the combustion process, to some type of load. In most of those applications, high heat transfer rates are required—especially in circumstance where the energy consumption is relatively high. Furthermore, high rates of heat transfer lead to short processing time, which is often needed for product quality. Depending on the application, the heat may be transferred indirectly from the flame to the load or directly from the flame to a heat transfer medium such as flame impingement heating.

1 Introduction

1.1 Introduction to flame impingement heating

Flames that impinge on a wall provide an efficient and flexible way to transfer energy in industrial applications. In such processes, a large amount of energy is transferred to the impingement surface. Due to this reason, directly impinging flame jets are widely used as a rapid heating technology in many industrial applications, including heating of metals, tempering glass, annealing of materials and melting of scrap metals. Stagnation flames are also used to modify the surface properties of various materials. For example, premixed methane-air flames can beneficially alter the properties of polymer films[1]. In most of these applications, in order to avoid shifting a flame in an uncontrolled manner, the flame is stabilized by being attached to a simple device known as a burner. Accordingly, it has been concluded that the use of directly impinging flame jets with high velocity burners instead of other techniques, such using as furnaces, has a lot of advantages. First, the heat transfer is enlarged. Second, energy can be saved by switching on the burners only when the heat is demanded [2]. Also, one can avoid materials melting by simply turning off the burners. Finally, the heat can be applied locally.

However, the major disadvantage of flame-impingement heating is the non-uniformity of the heat flux distribution, particularly on a large target surface [3]. As a result, hot spots are often created at the stagnation point, which is a point in a flow field where the local velocity of the fluid is zero. For this reason, the rapid heating technology of flame-impingement heating raises the need for the knowledge of the heat-flux distribution of a flame jet impinging on a product. This way, the optimum firing strategy for a given material can be determined. With this motivation, heat flux distribution on the impingement surface, particularly at the stagnation point, has been studied extensively. Few papers [4-7] have presented comprehensive and informative reviews of the experimental conditions that have been used in flame impingement studies. Many parameters have been proven to exert significant influence on the thermal performance of impinging flame jets. These parameters include equivalence ratio, fuel type, oxidizer composition, plate-to-burner distance and Reynolds number of the air/fuel mixtures. For more details about the comprehensive literature review, see Chapter Two. The majority of these studies have been related to turbulent flames;

there exist few basic studies of laminar flames impinging on walls. Also, in most previous research, either methane or natural gas was used. To my knowledge, for flames impinging normally or at an angle to cylindrical and plane surfaces, no ethanol-air or ethanol-hydrogen air measurements have been made. Therefore, laminar premixed ethanol-air and ethanol-hydrogen air flames were tested in this present work. The motivation of using ethanol stems from the issue of energy resources conservation and environmental concerns that arise from the use of fossil fuels. Most of the existing literature is related to flame impingement normal to a flat surface. Few studies have examined other configurations, such as flame impinging normal to a cylindrical surface and flame striking at some angle to a flat surface. In this present work, these types of configuration were studied.

In terms of measurement techniques, previous studies measured the heat transfer from the flame to a solid wall using two different steady state methods [8]. One method measures the sensible energy gain of the coolant for a cooled solid. This method is simple and relatively low in cost. However, in this method, the results of the heat flux rate then become ambiguous, because the size of the area can be chosen in different ways. In the second method, the local heat flux is determined using a small gauge imbedded in a much larger solid. The hot end of the gauge is exposed to the flame, while the cold end is water-cooled.

Two different variations of this method have been used [8]: a heat flux transducer and a gradient through a thin solid material. A heat flux transducer has good accuracy, high response time and good spatial resolution. Nevertheless, there are some potential concerns with this technique. Calibration is required. This may be complicated in a mixed radiation and convection environment, such as a flame environment, because calibration typically requires a blackbody source. The maximum allowable temperature and heat flux for some of the commercial transducers appear to limit their use in high-intensity flame impingement. For a gradient through a thin-solid-material method, the heat flux is calculated using a one-dimensional conduction equation, based on the measured difference temperature between the hot and cold side. This method is very accurate and simple. Also, the

surface temperature and the heat flux rate can be determined. Therefore, this method was used in the present work. In addition, in this technique, surface temperature measurement is especially crucial for the determination of heat transfer from flames to solid walls. Common methods to measure the surface temperature include thermocouples, thermostat and optical pyrometer. However, each of these methods has its drawbacks. Thermocouples need a good physical bond to surface. This is difficult to achieve, especially when measuring the surface temperature of any moving part. Therefore, pyrometers, which exploit thermal radiation for temperature measurement, are used as an alternative method in such cases; they are non-intrusive and have fast response time. However, this method is difficult to use in radiating environments, such as flames and plasmas. Also, the pyrometers have other disadvantages, such as dependence on the target surface emissivity, which is often not exactly known and which varies with time—especially at high surface temperatures when the sample changes physically or chemically. Furthermore, it is very difficult to use this method for measuring the surface temperature of transparent materials, since the emissivity is very low. All the above techniques' drawbacks may lead to reduction the measurement accuracy.

Thermographic phosphors overcome these above-mentioned drawbacks. Thermographic phosphors are rare earth- or transition metal-doped ceramic materials that fluoresce when exposed to light. The emission wavelength, intensity, and decay rate are all temperature-dependent, so any of these properties can be measured to determine temperature. The change in the emission wavelength is often a minor effect, so high resolution spectrometers are needed for temperature evaluation[9], while emission intensity and decay rate have advantages for different applications. The total intensity is a function of temperature, excitation intensity and thickness of phosphor coating. Therefore, this method is suited for surface temperature measurements, as long as the excitation light intensity is stable and as long as the thickness of the coating remains constant; this is often difficult to achieve. Phosphorescence lifetimes are most often evaluated for temperature measurements, since the excitation intensity plays a minor role. In general, the thermographic phosphor method is good for surface temperature measurements and is proven to be

useful and accurate for a variety of thermal measurement applications [10-13]. This motivated us to use the thermographic phosphor method for measuring the surface temperature, instead of the other traditional methods.

1.2 Research objective:

In view of the very limited and incomplete information to determine the heat flux characteristics of the impinging flame jets the present study was carried out to address this point. Accordingly, the present study mainly focused on an experimental investigation of the heat flux characteristics at the stagnation point for the impinging flame jets, namely the premixed ethanol/air and hydrogen/ethanol/air flame jets, using thermographic phosphors. First, the surface temperatures on the both sides of the impingement surface were measured using thermographic phosphors. Then, based on the surface temperatures' difference, the local heat fluxes were calculated using a one-dimensional conduction equation. The effects of the important parameters, such as overall geometric configuration and some operation conditions that affect the heat transfer between the flame and the impingement surface, were investigated. More specifically, the present work was divided into three sections:

1) Investigation of the heat flux characteristics at the stagnation point of a premixed ethanol/air and hydrogen/ethanol/air flame jets impinging normally on a horizontal flat plate. Influences of impingement surface thermal conductivity, cold gas velocity, equivalence ratio, plate-burner-distance, oxidizer composition and hydrogen addition on local heat flux will be examined, and the fundamental reasons behind these effects will be discussed.
2) Investigate of the heat flux characteristics at the stagnation point of a premixed ethanol/air flame impinging obliquely on a flat plate. The influence of the angle of incidence between the burner and the impingement plate on the stagnation point heat flux will be studied, along with the variations in cold gas velocity and plate-to-burner distance.
3) Investigate of the heat flux characteristics at the stagnation point of a premixed ethanol/air flame impinging normally on a cylindrical surface.

The effects of cold gas velocity on the stagnation point heat flux will be tested with the variations in plate-to-burner distance. The experimental results of the cylindrical surface will be compared with those of the flat plate under identical operating conditions.

1.3 Outline of the thesis

The present thesis includes six chapters and is organized as follows:

Chapter 1 provides a brief introduction and the objective of the present study.

Chapter 2 gives an intensive review of the investigation of heat transfer characteristics of the premixed impinging flame jets.

Chapter 3 presents the background of some concepts that are related to this work. This includes some fundamentals of the laminar premixed flame. It also discusses the flow field and heat transfer mechanism of the impinging flame jet. At the end of this chapter, a brief overview of different temperature measurement methods, with a focus on the thermographic phosphor method, is also presented.

Chapter 4 illustrates the experiments and the methods that were used in the course of this work. This includes the description of the two experimental setups used to determine the stagnation point heat flux of the impinging flame jet on a flat plate and cylindrical surface, respectively. In addition, it describes the calibration method of the thermographic phosphor. Then the methodology applied in this work and the uncertainty analyses are presented. At the end of this chapter, the model applied in this current study is introduced.

Chapter 5 presents the analysis and discussion of all the experimental results obtained in our present work. According to the impinging flame configuration, this chapter is broadly divided into three sections: flame impinging normally on a flat plat, flame impinging obliquely on a flat plate and flame impinging normally on a cylindrical surface**.** In these sections, the effects of different parameters on the heat flux are explored

Chapter 6 concludes the thesis and summaries the results. Finally, future scope expanding on the present work is presented.

2 Literature Survey

Many studies have been carried out on the heat transfer characteristics of flame impingement jets. In this survey, the previous works are categorized in several different ways to illustrate the information available for particular conditions. The review provides a fundamental understanding of thermal characteristics of the flame impingement jet and the influences of experimental conditions on it. Furthermore, it determines the kind of significant information that is lacking in literature.

2.1 Configuration

Many important parameters arise in flame jet impingement processes. The most important aspect is the overall geometric configuration. This includes the shape and the orientation of the target relative to the burner. Different types of configurations have been studied for impinging flames. These are (1) normal to a plane surface (2) normal to a cylinder in cross flow and (3) flame at an angle to a plane surface.

2.1.1 Flame impinging normally on a plane surface

In this configuration, seen in Figure 2.1, flames impinge normally on the plane surface. These types of configurations have been widely used in many industrial applications. Therefore, they have received the most attention in existing research. The previous works are summarized in Table 2.1.

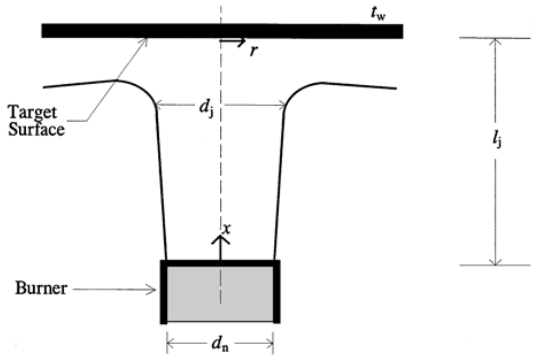

Figure 2.1: Flame impinging normally on a plane surface

Table 2.1: Types of target surface for flame impinging normally on a plane surface

Impingement Surface shape	Impingement Surface material	Surface treatment	Impingement Surface condition	Impingement Surface size	Ref
Rectangular	Copper plate	untreated	(steady state) water cooled	200mm×200mm thickness=8mm	Dong et al. [14]
Circular flat plate	Material: Copper, brass and stainless steel	Untreated	(steady state) water cooled	Ring type calorimeter o.d=105mm	Baukal and Gebhart[15]
Rectangular	Copper plate	Untreated	(steady state) water cooled	200mm×200mm thickness=8mm	Kwok et al. [16]
Rectangular	Copper plate	Untreated	(steady state) water cooled	200mm×200mm Thickness=8mm	Dong et al. [17]
Rectangular	Copper plate	Untreated	(steady state) water cooled	180mm×90mm Thickness=6mm	Anderson and Stressino[18]
Plate	Cooper plate	Untreated Polished copper plate	water cooled	Not mentioned	Van der meer[19]
circular	Aluminum plate	Silver coated	water cooled (steady state)	Radius=15.24cm Thickness=1.5cm	Mizuno et al. [20]
square	Steel plate	coated with lamp black	Cold plate	Side=1.83m	Milson and Chigier [21]

Dong et al. [14, 17] performed an experimental study to investigate the heat transfer characteristics of a pre-mixed butane/air round and slot flame jet, respectively, of low Reynolds number striking normal to a flat rectangular plate. Baukal and Gebhart[15] studied the pre-mixed oxygen enhanced/natural flames impinging normally on a circular flat plate. Van der Meer [19] studied the heat transfer characteristics of the turbulent pre-mixed air/natural gas impinging flame jet. Milson and Chigier [21] investigated methane and methane/air flames impinging normally on a plane surface. They found the presence of a cold central core of unreactive gas around the stagnation point. Although the majority of the previous studies concentrated on heat transfer characteristics for the round flame jet, Zhang and Bray [22] investigated various impinging flame shapes regarding normal flame impingement on a plate surface area.

In this configuration, a complete understanding of the heat transfer characteristics is not yet possible due to the limited information obtainable from the literature. This study found almost no investigations documenting impingement flame jets using ethanol or hydrogen.

2.1.2 Flames impinging normally on cylinders

For this geometry, shown in Figure 2.2, the cylinder axis is usually vertical with respect to the burner axis. Despite the importance of this configuration in many industrial applications such as heating round metal billets, and in fires impinging on pipes in chemical plants, there are scant studies that investigated impingement of pre-mixed flame on cylinder as compared with flame impingement normal to plane surface. A summary of some previous studies are shown in Table 2.2.

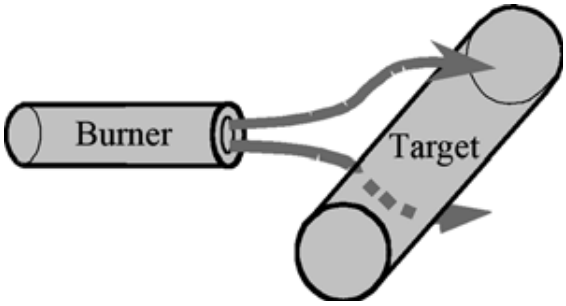

Figure 2.2: Flame impinging normally on a cylinder in cross-flow.

Table 2.2: Types of target surface for flame impinging normally on cylinder

Impingement Surface material	Surface treatment	Impingement Surface Condition	Impingement Surface size	Ref
Copper	Untreated	(steady state) water cooled	180mm×90mm Thickness=6mm	Anderson and Stressino[18]
copper	untreated	Transient caorimeter	outside diameter=22mm	Hargrave et al.[23, 24]

Jackson and Kilham [25] studied the impingement of hot gases on a cylindrical surface at right angles. The cylindrical surface was rotating at 40 rpm. This rotation had no effect on the heat transfer because the tangential velocity of the rotating tube never exceeded 0.1% of the free stream gas velocity. Anderson and Stressino [18] studied the heat transfer distribution of the flame impinging normally on a cylinder surface. The combustion systems studied were oxygen-hydrogen, oxygen-propane, oxygen-acetylene, and air-methane with combustion stream. Hargrave et al.[23, 24] studied heat transfer from premixed methane-air flames impinging normally on a rotating cylinder. Heat fluxes measured at the stagnation point demonstrate that the trends observed in measured heat flux profiles are mainly determined by variations in the mean velocity and temperature within a flame. Chander and Ray [26] investigated the heat transfer characteristics of laminar methane/air flame impinging normally on a cylindrical surface. High stagnation point heat fluxes were obtained when tip of the flame inner reaction zone just touched the target surface.

Considering the dearth of studies cited in the literature related to the flame impingement normally on a cylinder, more study is required for this configuration.

2.1.3 Flames impinging at different angles

In this configuration, shown in Figure 2.3, a flame impinges on the target surface with an oblique angle. In some applications, as a result of the flame impingement shape or difficulties on positioning of the burner, the flame jet may be required to impinge on the target surface with an oblique angle rather than normally. However, very few studies have been carried out to deal with inclining impingement of a flame jets. Yan and Saniei [27] suggested that the oblique angle of the impinging flame jet causes intricacy in fluid flow as well as the heat transfer, which leads to the problem of non-uniformity of heating and cooling in industrial processes. Dong et al. [28] performed a number of experiments to investigate the heat transfer characteristics for premixed methane/air flames, which imping on the inclined plate at different angles. The inclination angles varied, e.g. 57°, 67°, 80° and 90°.

Kremer et al. [29] investigated an impinging turbulent methane air flame jet with oblique angles ranging from 5° to 90°. In both studies, the local heat flux from the flame to the plate was measured using a heat flux transducer. It was found that the heat flux decreased as the jet exit angle was reduced. At the smaller angle, the maximum heat flux position shifted away from the stagnation point at the angle of 90°. The present work was conducted to investigate heat transfer of the laminar premixed ethanol/air flames impinging obliquely upon a water-cooled plate. The inclination angles chosen for our investigation were 50°, 70° and 90°.

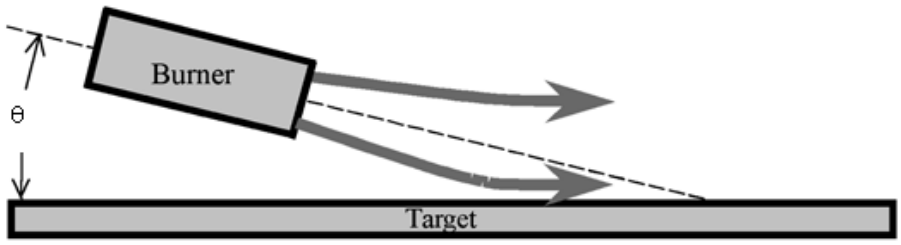

Figure 2.3: Flame impinging obliquely on the flat plat

2.2 Different operating conditions

Operating conditions possess a strong impact on heat transfer intensity and also stability of the flame during heating flame impingement. These operation conditions include oxidizer composition, fuel type, separation distance between the target and the burner, flame equivalence ratio and Reynolds number.

2.2.1 Oxidizer composition and fuel type

The most important variable, after the physical configuration, is the oxidizer composition. The oxygen mole fraction in the oxidizer plays an important role in influencing the intensity of heat transfer. A summary of different oxidizer composition and fuels investigated by different researchers is given in Table 2.3. In the vast majority of previous research, air is used as the oxidizer, except for a few in which oxygen is used. Oxidizer composition affects both the flame temperature and the amount of dissociation in the combustion products. As an example, adiabatic flame temperature of methane, that combust stoichiometrically with air and oxygen are 2220K and 3054K, respectively. Baukal and Gebhart's study of flame impingement heat transfer [15] used oxygen-enriched air and natural gas flames, with oxidizer composition Ω ranging from 0.21 to 1.0. It was found that the heat flux from the flame to the plane surface increased by 54–230% by increasing the oxidizer composition Ω from 0.21 to 1.0. It was reported that the effects of reducing oxygen purity upon the flame impingement heating had not previously been investigated. Baukal and Gebhart also pointed out that it was the first study to investigate a wide range of oxidizer composition between (Ω=0.21) and pure oxygen (Ω=1.0). In this present work, pre-mixed oxygen-enriched air/ethanol flames were investigated, with oxidizer composition ranging from 0.21 to 0.4.

Fuel composition is another parameter of interest. In the gas-fired flame jet studies, various gaseous fuels have been selected to produce the flame jet, see Table 2.3. Dong et al. [14] noted that a majority of the previous research focused on the heat transfer characteristics of flame jets using either methane or natural gas; no studies documented an impingement flame jet using butane gas or propane. Milson and Chigier [21] conducted investigation and comparison of the heat transfer

characteristics between both premixed flame and diffusion flame using methane-air and methane, respectively, and found that the maximum heat transfer occurred with premixed flames. Chigier [30] used another uncommon fuel, coke oven gas and air. Experiments were also conducted with heavily fuel oils in place of coke oven gas. It was concluded that no remarkable difference is identified between the applications of these two fuels. Also, Schulte [31] used acetylene-air pre-mixed laminar flames. He also used other fuels like natural gas and burnt with oxygen. Results showed that the heat-transfer profiles can be relatively flat over a given area and that the best operating condition must be determined experimentally.

There are many fuel type and possible combinations of fuel that have not been tested. They include impinging flames normally on a plane surface with ethanol-air or ethanol-hydrogen-air, to name a few. Considering the importance of ethanol as alternative fuel, this constitutes a troubling research gap.

2.2.2 Equivalence Ratios

This ratio directly influences the sooting tendency and the level of dissociation in the combustion products. Fuel-lean flames ($\phi < 1$) produce only non-luminous radiation, since no soot is generated. Flames at or near stoichiometric equivalence ratio ($\phi = 1$) generate the highest flame temperatures, because of complete combustion. Fuel-rich flames ($\phi > 1$) produce a combination of both luminous and nonluminous thermal radiation. Therefore, it was demonstrated that equivalence ratios have a very important effect on the heat transfer characteristics of an impinging flame jet system, and many studies have been performed to explore its thermal effect. Furthermore, equivalence ratio is proven to have effect on the stability and dynamics of a premixed flame. A summary of the equivalence ratio used by different researchers is given in Table 2.3.

Baukal and Gehbhart [32] pointed out that in most cases, ϕ is taken as 1, since most of the industrial flames generally operate at an equivalence ratio equal to one. Hargrave et al. [23] concluded that the maximum heat flux occurs at an equivalence ratio between 1 and 1.1. It was observed that a fuel/air mixture deviating from

stoichiometric condition will result in a decrease in the maximum rate of heat transfer. In the study performed by Kwok et al. [16] in order to investigate the heat transfer characteristic of a premixed butane/air flame jet impingement, the maximum heat flux occurs when the combustion is performed in a slightly fuel-rich condition with equivalence ratio varying between 1 and 1.1 for the slot jet, and from 1.1 to 1.2 for the round jet of the same Reynolds number. Premixed flame is used in many applications, because it produces very rapid rate combustion, very low soot formation and high heat transfer. Hence, equivalence ratio is of special importance to premixed flame.

Table 2.3: Type of fuel, oxidizer and flame along with operating conditions

Fuel	Oxidizer	Plate-to-burner Distance (H/d)	Equivalence Ratio(ϕ)	Reynolds Number/velocity	Ref
Natural gas	Air		1.00	8855	Mohr et al. [33] And Wu et al.[34]
Natural gas	Air	0.39, 0,59 and 0.785	1.0, 1.5 And 2.0	5253,8855 and 12,456	Mohr et al. [35]
Natural gas	Oxy-enhanced air	0.5-6	1.0	Gas velocity= 1.23-6.17 m/s	Baukal and Gebhart [15]
Methane	Air	$0.04 \leq H/d \leq 8$	1.0	5000-12,000	Mizuno et al. [20]
Methane	Air	Plate-to-burner distance varied from 0 to 160 mm	0.8-1.2	2000-12,000	Haegrave et al. [23, 24]
Methane	Air	10 (premixed) 16(diffusion)	Air/methane (2.0/1.0)	7000 (premixed)	Milson and Chigier [21]
Butane gas	Air	1-8	0.7-1.1	600-2500	Dong et al. [14]

Butane gas	Air	2-13	1.0	800-1700	Dong et al.[28]
Butane gas	Air	2 and 5	1.0	900	Dong et al.[36]
Butane gas	Air	1 and 5	1.0	2500	Dong et al. [14]
Coke-oven gas	Air	Plate-to-burner distance=234 cm		Air flow rate =178kg/h and gas flow rate 390kg/H	Chigier [30]
Acetyllene	Oxygen	Not mentioned	Volume ratio 1:1	Not mentioned	Woodruf and Giedt [37]

2.2.3 Burner-to-plate distance and its effects

The separation distance between the burner exit and the target surface can significantly affect the impinging flame structure, and thus heat transfer characteristics. A number of studies were cited in the literature showing the effect of separation distance, and an overview of a few is given in Table 2.3. It is observed that the heat flux at the stagnation point is measured in the majority of the research.

Baukal and Gebhart[15], in their research of oxygen-enhanced natural gas flames impinging on a flat plate surface, showed that a shorter nozzle-to-plate distance results in higher impingement heat flux. Also, they found that if the separation distance between the burners and the surface is large, there will be little benefit of increasing the O_2 content in the oxidizer because the benefit will be marginal. Minzuno et al. [20] observed that as the distance between the burner tip and the surface is decreased, the heat flux increased because, in smaller separation distances, there is less entrainment of cold air into the flame and temperature becomes high. Hargrave et al. [23, 24] summarized the nozzle-to-plate distance that matches to maximum heat flux under various Reynolds numbers and equivalence ratios. It was

found that the maximum heat flux generated by a circular burner occurred at H/D= 2.5 when Reynolds number is 2000. Nevertheless, Van der Meer [19] concluded that peak heat flux happens when H/D=5 for a circular flame jet working under a Reynolds number varying from 1771 to 2700. Schulte [31], in his study of small natural gas/oxygen and acetylene/air flames impinging on flat surfaces, found that although the heat transfer rate can be changed by changing the length of the primary cone, the distance between the torch and the target surface also must be changed so as to maintain a relatively flat heat transfer profile. Hou and Ko [38] studied the effect of heating height on the flame characteristics of a domestic gas stove. Results showed that flame structure, temperature distribution and thermal efficiency are greatly influenced by the heating height. With increasing heating height, the thermal efficiency first increases to a maximum value and then decreases. .Furthermore, Hou and Ko observed that the optimum heating height, described as the widest high-temperature zone and highest thermal efficiency, was obtained when both the inner cone and the outer diffusion flame are intercepted by the target surface. The results provide good insight into development and improvement of energy efficient gas stove burners.

However, there are many possible combinations of fuel, plate-to-burner distance and equivalence ratio that have not been tested, e.g. hydrogen-enriched ethanol/air flames.

2.2.4 Reynolds number

Reynolds number of the air/fuel jet is defined as:

$$Re=du/\nu$$

where d diameter of burner, u velocity of mixture gases and ν kinematic viscosity.

A broad range of Reynolds numbers at the burner (Re) has been used. They vary from 350 to 35.300, as seen in Table 2.3. It was observed that the Reynolds number was not always given. For a number of studies, the flows are pointed out to be either

laminar or turbulent. In other studies, only the flow velocity is mentioned. Dong et al. [14] conducted experimental studies on impinging flame jet systems working under laminar and transitional flow conditions with Re < 2300. It was observed that the Reynolds number has a strong influence on the heat transfer rate; increasing the Reynolds number enhances the heat transfer rate at both the stagnation point and the wall jet region. Hargrave et al. [23, 24] studied forced convection heat transfer from premixed methane / air impinging flames, and their results are in good agreement with those presented by Dong. Malikov et al. [39] investigated the direct flame impingement heating for rapid thermal material processing using an array of flame jets. A burner exit velocity varied from 150 to 200 m/s for ambient air. It was found that very high jet velocities (Mach number up to 1) can achieve a rapid, high efficient and uniform heating of the load without causing instability of the flame. Mizuno [20, 40] found that whenever the mixture is become leaner, the gas temperature decreases; however, increasing the Reynolds number increases the convective heat transfer and appears to dominate the effect of decrease in temperature.

The number of investigations in which the flame is laminar very few. Thus there is a need for more in depth studies on laminar flame impingement.

2.3 Target material and surface preparation

In most previous studies, the most commonly used target materials were brass, stainless steel, copper and aluminum. Tables 2.1 and 2.3 show the different target materials used in the previous investigations. For example, Zhao et al. [40] studied flames impinging normally on brass, bronze and stainless steel, respectively. It was observed that when using a metal impingement of high internal thermal conductivity, faster conduction, and thus overall heat transfer through the impingement target, can be achieved due to the very low thermal resistance encountered. In spite of that, these materials have a relatively low melting point. For this reason, especially at high surface temperature, they have not been used. Refractory materials, such as alumina (Al_2O_3) and sillimanite (Al_2SiO_5), were used.

Stationary impingement targets have been used in most reported studies, because that is the common situation in real-life application. Most of the target surfaces were untreated. Nevertheless, in a few works, the surfaces were coated or treated, in order to investigate a specific surface effect. Baukal and Gebhart [32] investigated different surface treatments (untreated, polished and blackened to study the effect of surface emissivity). It was found that the blackened and the polished surfaces have the highest and lowest value of heat flux, respectively, while the untreated surfaces is of a value between them. Furthermore, they investigated the catalytic effect using alumina-coated (nearly non-catalytic), untreated, and platinum–coated (highly catalytic) impingement plate surfaces. The heat flux received by the platinum-coated surface is found to be the highest, whereas the heat flux received by the alumina-coated surface is similar to that received by untreated surface. In their study, Kiham et al. [41] coated the impingement surface with different oxides. The aim of this was to estimate the emissivity of the coatings.

In our present study, i studied flame impinging normally on aluminum oxide and zirconium oxide, respectively; both plates were coated with thermographic phosphor. The objective of coating was to measure the surface temperatures of the plates.

2.4 Surface temperature measurements

In flame impingement heating applications, surface temperature plays a main role as an indicator of the condition of a product or piece of machinery, both in manufacturing and quality control. Accurate measurement of temperature helps to improve the product quality and increase the productivity. Downtimes are decreased, since the manufacturing processes can proceed without interruption and under optimal conditions. Also, if the surface temperature is correctly measured, the heat flow at the surface can be calculated. In their comprehensive review, Baukal and Gebhart [42] reviewed the surface temperature measurements on the experimental studies of jet systems. It was noted that the surface temperature on the hot side ranged from 290 K to 1900 K. In most measurements, a cold side surface temperature, $T_{w,}$ was maintained below 373K, using a water-cooled target. In some studies, the surface temperature level was actually for the heat flux gage, and not the

target. For example, Fairweather et al. [43] reported a maximum surface temperature of 1600K. However, the target was made of brass, which melts at about 1300K. A stainless steel heat flux gage imbedded in the brass target was used to measure the heat flux. Stainless steels have a melting point of about 1700K.

In most studies, two traditional methods were used to measure the surface temperature [44]: probe techniques, often thermocouples and IR- methods.as mentioned previously, Thermocouples have several advantages that make them popular in many applications such as industrial, medical, and home appliances. In some applications, however, thermocouples have some disadvantages. Thermocouples probably have an effect on the flow field and the temperature field around them. Also, the temperature gradient close to the surface is very strong for the product subjected to flames. Thus, it is very important that the thermocouples are in good contact with the surface, and this is not easy in some cases. For a product that is melting, cracking or burning, the position of the thermocouple related to the surface may change leading to problems due to correctly defining the position of the thermocouple [45]. IR- methods, e.g. those using pyrometers that measure the black body radiation from the surface, are good for many purposes. However, this method has problems dealing with varying emissivity and radiation from flames interfering with the surface radiation [44].

Recently, the phosphorescence technique has been developed for remote measurements of surface temperature. It has mainly been used in scientific and industrial applications of surface thermometry to complicated geometries, e.g., turbine engines [46] and rotor engines [47]. Other quantities such as heat flux through a surface have been investigated, because of its high importance to science and engineering community [48, 49]. In the last decade, as the applications of thermographic phosphors have expanded, few attempts have been implemented in combustion environment [50]. A comprehensive review on the topic of phosphor thermometry will be found in this article [9, 51, 52].

Phosphors are thermographic if they exhibit emission-changing characteristics with temperature. A phosphor becomes highly fluorescent or phosphorescent when it is excited by appropriate source, e.g. electron beam or ultraviolet radiation. Phosphorescence has longer excited state lifetimes than fluorescence; it is usually this that is used for determining temperature in a thermographic phosphor system. Thermographic phosphor provides a good accuracy and fast response. Also, it allows non-disturbed gas movements close to the surface, does not interfere with emissivity and radiation from flames, and covers a wide range of temperature up to higher 1700 K. Thus, to address the disadvantages of using traditional methods for measuring the surface temperature, especially in a flame environment, thermographic phosphor is preferred .

Therefore, in this work, thermographic phosphors were used to measure the surface temperature of the flame impingement plate.

2.5 Heat transfer measurements methods

For most flame impingement heating applications, the total heat flux represents the most important factor in designing the system. Total heat flux (i.e. the combination of radiation and convection) is the total rate of heat energy transfer through a given surface, per unit surface area.

The total steady- state heat flux has been measured using different methods. Among these methods are measuring the sensible energy gain of coolant for a cooled solid. In their study, Baukal and Gebhart [15, 32] calculated the average heat flux over the entire solid surface from the sensible energy gain of cooling circuits. Another method is determining the heat flux using a small gauge embedded in a much larger solid. The hot end of the gauge is exposed to the flame, whereas the cold end is water-cooled. Two different variations of this method have been used: a heat flux transducer and a temperature gradient through a thin rod solid. For the heat flux transducer, an electrical single is generated and proportional to the heat flux. Dong et. al. [14, 17] used an impingement plate, evenly cooled at its back side (non-flame-side) by a steady supply of cooling water. The local heat flux transfer to the surface

was determined with a small ceramic heat flux transducer. Van der Meer [19] used heat flux transducer- impeded flush with the surface of a water- cooled flat plate. Schulte [31] determined the heat-transfer profile of small natural gas-oxygen and acetylene-air flames to a flat cooled surface using a water cooled heat flux transducer. This technique is simple and has both good accuracy and fast response time. However, the maximum allowable temperature and heat flux for the most of the existing commercial heat flux transducer seem to limit their use in high-intensity flame impingement.

For the gradient through a thin solid rod, thermocouples are used to measure the temperature gradient through the solid. The heat flux was calculated using a one-dimensional conduction equation. In most previous measurements, the probe has shields to reduce the heat flux from the sides. For example, Beer and Chigier [30] used uncoated stainless steel probes to measure the heat flux from the flame to the point on the open-hearth furnace.

In this study, thermographic phosphors are used to measure the temperature gradient between the two surfaces, hot side and cold side, of a water-cooled ceramic plate. The heat flux is calculated using a one-dimensional conduction equation.

2.6 Summary of literature survey

To summarize, a number of studies have been conducted on impinging flame jets to investigate the influences of the main parameters on their thermal performance. It has been shown that the different operation conditions, e.g. plate-burner-distance, equivalence ratio and Reynolds number, have strong influences on the flame-impinging thermal performance. In the majority of the studies, either methane or natural gas was used. Most of the studies are related to flame impinging normally on a flat surface. However, there are many possible combinations of fuel, oxidizer and equivalence ratio that are of much interest from an applications view point but have not been tested so far. For flames impinging normally on a plane surface, no ethanol-air or ethanol-hydrogen-air measurements have been made. Also, laminar premixed flames are scarcely investigated. Other configurations studied, e.g. flame striking at

angle to a flat plate or normally to cylindrical, are very few. The present study aims to help fill this gap by studying the heat flux for laminar premixed ethanol/air and hydrogen/ethanol/air flames at the stagnation point, using thermographic phosphor. Flame impinging normally on flat and cylindrical surfaces is studied. Next chapter identifies and reviews theoretical concepts that are related to the work presented in this thesis, such as laminar premixed flame, flame impingement and thermographic phosphor.

3 Theoretical Backgrounds

This chapter reviews the theoretical concepts that are related to the work presented in this thesis. This chapter consists of four main sections. In the first section, fundamentals of laminar premixed flames are presented, such as flame classification, premixed flame structure, laminar burning velocity, flame temperature, stability of laminar premixed flame and the governing equations. In the second section, characteristic regions and the heat transfer mechanism in flame impingement are illustrated. The third section gives an overview of different temperature measurement methods. In the last section, thermographic phosphor techniques are explained in detail.

3.1 Fundamentals of laminar premixed flames

First, in order to obtain a basic understanding about laminar premixed flames, this section includes a brief explanation of some of the related fundamentals and concepts.

3.1.1 Flames and their classification

Combustion is defined as a rapid exothermic reaction that liberates substantial energy as heat and flames as combustion reactions [53]. Combustion can occur in either a flame or non-flame mode. A flame is a self-sustaining propagation of a localized combustion zone at subsonic velocities. There are several key words in this definition. First, a flame has to be *localized*, i.e., the flame occupies only a small portion of the combustible mixture at any one time. The second key word is *subsonic*. A discrete combustion wave travels subsonically is termed a deflagration [54]. Flames may be either stationary flames on a burner with propagation into a flow of gas from a burner tube, or they may be freely propagating flames traveling in an initially quiescent gas mixture [55]. In general, flames are almost always divided according to their premixed nature and flow type. With respect to premixed- ness, stationary flames are of two general types:

(a) Premixed flames where the fuel and oxidizer are perfectly mixed before approaching the flame reaction region. These flames can only be obtained if the initial fuel and oxidant mixture lies between certain composition limits called the composition limits of flammability.

(b) Non-premixed flames or diffusion flames, where the reactants are initially separated, and reaction occurs only at the interface between the fuel and the oxidizer.

The two types of flames are also differentiated physically in that, for defined thermodynamic starting conditions, the premixed system has a defined equilibrium adiabatic flame temperature. For an idealized situation of planar flame in a one-dimensional flow field, it has a defined adiabatic burning velocity or equivalent mass flux in a direction normal to its surface**.** An unstrained diffusion flame has no such simply defined parameters [53]. Premixed and diffusion flames can be seen in Figure 3.1. The most important property of premixed-gas flames that distinguishes them from non-premixed flames (e.g., gas-jet flames, liquid fuel droplet flames) is the fact that in premixed flames the flame front propagates relative to the gas. This is because premixed flames are not constrained to follow a contour of stoichiometric composition. In contrast, with non-premixed flames, the fuel and oxidant must mix in stoichiometric proportions before a chemical reaction can occur. The propagation speed of the premixed flame with respect to the unburned gases is called the burning velocity, SL

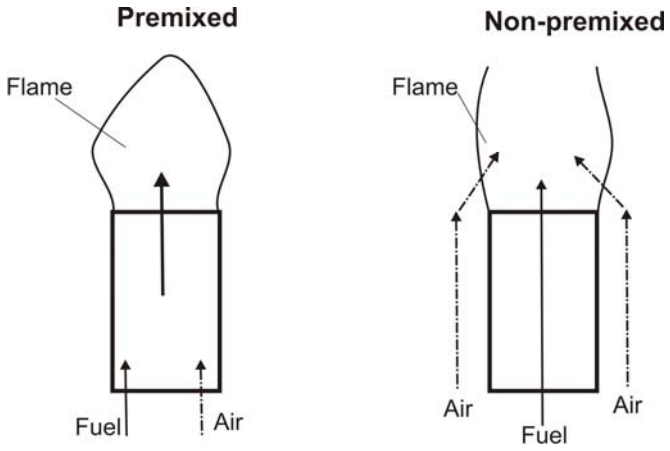

Figure 3.1: Schematic illustrations of laminar flames

3.1.2 Laminar premixed flame structure

The temperature profile through a flame is perhaps its most important characteristic. Figure 3.2 illustrates a typical flame temperature profile, together with other essential flame features. To understand this figure, it is necessary to create a reference frame for our coordinate system. A freely propagating flame occurs when a flame is initiated in a tube containing a combustible gas mixture. The appropriate coordinate system would be fixed to the propagating combustion wave. An observer riding with the flame would experience the unburned mixture approaching at the flame speed, S_L. This is equivalent to a flat flame stabilized on a burner. Here, the flame is stationary relative to the laboratory reference frame and, once again, the reactants enter the flame with a velocity equal to the flame propagation velocity, S_L [54] . In both cases, it is assumed that the flame is one- dimensional and that the unburned gas enters the flame at direction normal to the flame sheet. In other words, we consider that no radial velocity. Since a flame heats the products, the product density is less than the reactant density.

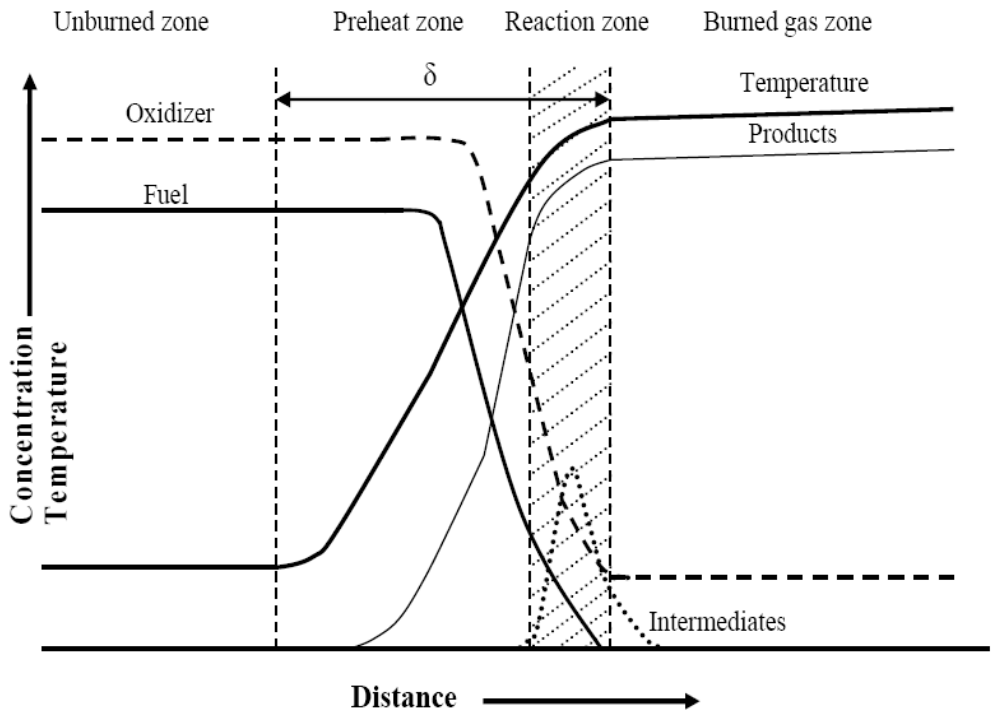

Figure 3.2: Sketch of a premixed flame structure

Thus, continuity requires that the burned gas velocity be greater than the velocity of the unburned gas:

$$\rho_u S_L A \equiv \rho_u v_u A = \rho_b v_b A, \tag{3.1}$$

where the subscript u and b refer to the unburned and burned gases, respectively. Thus, the flow of gas across the flame has considerable acceleration.

Building on the foundation of the hydrocarbon oxidation mechanism, It is possible to characterize the flame as consisting of four zones[54]: unburned zone, preheat zone, reaction zone and burned gas zone. Figure 3.2 shows schematically the structure of a laminar premixed flame. The unburned mixture of fuel and oxidizer is delivered to the preheat zone at ambient conditions, where the mixture is warmed by upstream heat transfer from the reaction zone. Thus, in the preheat zone, the temperature of the reactants increases gradually from the unburned mixture temperature to an elevated temperature near the reaction zone. As the reactant temperature approaches the ignition temperature of the fuel, the chemical reactions become rapid, marking the front of the combustion reaction zone (flame). The thickness of the flame front (δ, see Figure 3.2) is ~ 0.5 mm at atmospheric pressure and ~ 5 mm at 25 Torr and depends not only on pressure but also on initial temperature and equivalence ratio [54, 56]. Inside the flame, the reaction rate increases rapidly and then decreases as fuel and oxidizer are consumed and products produced. Because of the species concentration gradient, the reactants diffuse toward the reaction zone, and their concentrations in the preheat zone decrease as they approach the reaction zone.

Various species in the reaction zone are excited at high temperatures and emit radiation at different wavelengths that give flames different colors. For lean mixtures of hydrocarbon fuels and air, the bluish color is due to radiation from excited CH radicals, while radiation from CO_2, water vapor, and soot particles produce a reddish orange color. For rich mixtures, a greenish color from excited C_2 molecules is also observed. Flame propagation through the unburned mixture depends on two

consecutive processes. First, the heat produced in the reaction zone is transferred upstream, heating the incoming unburned mixture up to the ignition temperature. Second, the preheated reactants react in the reaction zone. Both processes are equally important and therefore one expects that the flame speed will depend on both transport and chemical reaction properties.

3.1.3 Laminar burning velocity

The flame velocity – also called the laminar burning velocity, normal combustion velocity, or laminar flame speed – is more precisely defined as the velocity at which unburned gases move through the combustion wave in the direction normal to the wave surface [57]. It is only unambiguously defined in a one-dimensional (1D) situation. Clearly, it is also the volume of combustible mixture, at its own temperature and pressure, consumed in the unit area of the flame front. Figure 3.3 shows a freely propagating 1D flame. A fuel-oxidizer mixture enters the system at the unburnt side with velocity U_g. A flame front propagates with velocity S_L in the unburnt mixture. The flame will remain at a fixed position in space only when the gas velocity U_g equals the laminar burning velocity SL exactly. The burning velocity of flame is independent of flow rate and burner size. However, it is affected by flame radiation, and hence by flame temperature, by local gas properties such as viscosity, thermal conductivity and diffusion coefficient, and by the imposed variables of pressure, temperature, air-fuel ratio and heat of reaction of mole of mixture.

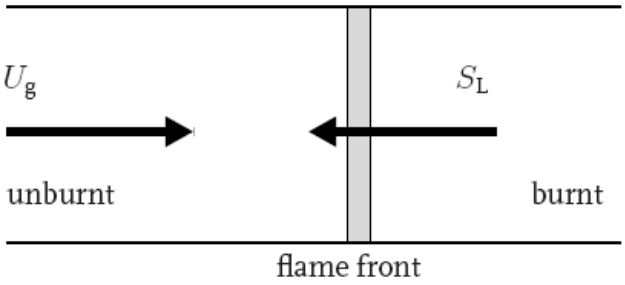

Figure 3.3: Freely propagating one-dimensional adiabatic flame.

Also, phenomena such as flame cooling and flame stretch have an important influence on the burning velocity [58, 59].

3.1.4 Flame temperature

Another important combustion parameter is the flame temperature. The flame temperature (T_f) is determined by the energy balance between the reactants and the products at equilibrium. If the reaction zone is spatially very thin in comparison to the rest of the domain of interest, then it is a common practice to denote the maximum temperature in the reaction zone to be the flame temperature. If the combustion process takes place adiabatically, and with no work, or changes in the kinetic or potential energy, then the flame temperature is referred to as the adiabatic flame temperature (T_{af}). Experimental measurements of T_{af} are very difficult and in most cases a calculated value is more reliable than the experimental measurements. For stoichiometric mixtures of most of the common fuels with air, the flame temperature is about 2000 K. Near the flammability limits, the calculated temperature is lower, about 1400-1500 K.

There are many factors that determine the flame temperature, such as fuel type, stoichiometricity, pressure, atmospheric temperature and percentage of oxygen content of the atmospheric. The flame temperature has a substantial effect on the flame speed. Also, it significantly influences the formations of the products of combustion.

3.1.5 Stability limits of laminar premixed flames

There are two types of stability criteria related to laminar flames. The first criterion is concerned with the ability of the combustible fuel-oxidizer mixture to support flame propagation and is strongly related to the chemical rates in the system. In this case, a point can be reached for a given limit mixture ratio in which the rate of reaction and its subsequent heat release are not sufficient to sustain reaction and, thus propagation [56]. This kind of stability limit includes:

(1) Flammability limits, in which gas-phase losses of heat from limit mixtures reduce the temperature, the rate of heat release and the heat feedback, so that the flame is not permitted to propagate;

(2) Quenching distances, in which the loss of heat to a wall and radical quenching at the wall reduce the reaction rate so that it cannot sustain a flame in a confined situation, such as propagation in a tube.

The second type of stability limits is related to the velocity of mixture flow and its relationship to the laminar flame velocity itself. This stability limit, which involves the phenomena of flashback, blowoff, and the onset of turbulence, identifies the restrictions of stabilization of a laminar flame in a real experimental situation.

3.1.5.1 Flammability limits

If small quantities of flammable fuel gas or vapor are added progressively to air, a point will be reached at which the mixture just becomes flammable. At this point, the percentage of fuel-gas mixture is called the lower flammable limit or lean flammable limit (LFL). If more fuel is added, another point will ultimately be reached at which the mixture will no longer burn. At this point, the percentage of fuel-gas mixture is called the upper flammable limit or rich flammable limit (RFL). Figure 3.4 shows the flammability limit of methane gas. It can be seen that when the combustible mixture gets too rich or too lean, the flame temperature decreases; consequently, flame speed drops significantly. Thus, eventually the flame cannot propagate when the equivalence ratio is larger than an upper limit or smaller than a lower limit. These limits are also referred to as explosion limits in some engineering applications. For hydrocarbon fuels, the mixture at the RFL contains about twice the amount of fuel compared to stoichiometric conditions. At the LFL, the mixture contains about half of the fuel as at stoichiometric. The flammability limits are often measured at ambient pressure using a tube with a spark plug at one end. When the temperature and pressure change, the flammability limits will also change because they affect the rate of the reaction [57]. Also, adding inert or dilution gases to a combustible mixture will reduce the flammable region.

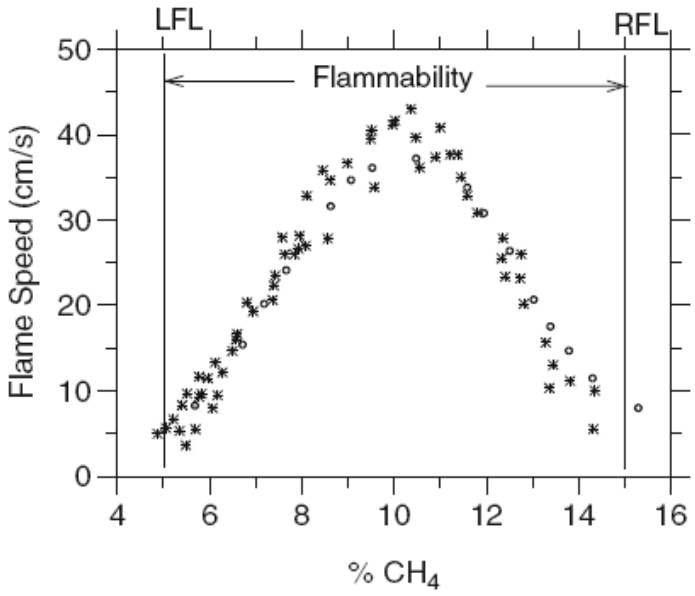

Figure 3.4: Sketch of lean flammability limit (LFL) and rich flammability limit (RFL) [59]

The range of flammability becomes wider as the temperature of the unburned mixture increase. Also, an increase in pressure above atmospheric usually widens the range of flammability.

3.1.5.2 Flame quenching

A relevant phenomenon is that of quenching. A flame close to a conducting material loses heat to the material, reducing the temperature of the reaction and consequently its reaction rate. If the heat losses are significant, the reaction may not be able to continue and the flame is quenched. Although the loss of active species may also occur in quenching, the nature of the surface does not appear to affect its quenching properties and it seems that quenching is primarily due to heat loss; differences in thermal conductivity between various surfaces are unimportant because the heat capacities of solids are high compared with those of gases. The main physical effect lies in the balance between the heat generated by the combustion reaction and the heat lost to the adjacent material. One of many examples of flame- quenching encountered in life is when firemen pour water on a fire. The quenching diameter, d_T, of a particular gas mixture is the minimum diameter of tube through which a flame in the stationary gas mixture can propagate. The quenching distance, d_Q, is a related quantity and refers to flame propagation between parallel plates [60]. Thus the

quenching distance or diameter d_T, is the diameter of the tube that just prevents flashback. Intuition would suggest that an inverse relationship would be obtained between flame speed and quenching diameter. Since flame speed varies with equivalence ratio ϕ, so should d_T vary with ϕ; however, the curves of d_T would be inverted compared to that of flame speed, as shown in Figure 3.5.

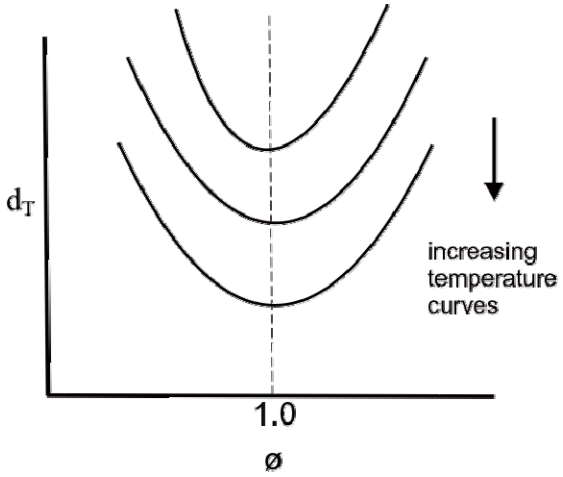

Figure 3.5: Variation of quenching diameter d_T as a function of equivalence ratio

3.1.5.3 Laminar Flame Stabilization

It is well known that a combustion wave moves at a characteristic burning velocity. Thus, a stationary flame may be achieved by flowing of the pre-mixed gases at the same speed in the opposite direction. Such a flame would have only neutral stability and its position would shift in an uncontrolled way.

In many industrial appliances, flame stability is obtained by attaching the flame to a simple device known as a burner. Regarding a typical laminar premixed flame, the burner accomplishes three jobs: the burner is configured so that the fuel and air become a homogeneous mixture in the appropriate proportions before they exit the burner. The most important aspect of the burner is that it acts as a heat sink that restricts movement of the flame and it also provides a suitably- shaped section to provide laminar flow. The actual stabilizing effect of the burner is provided by the rim alone and a simple metal ring will perform the same function.

The effect of the rim on the gas-mixture velocity is to reduce it to zero at the wall due to viscous drag, whilst its effect on the burning velocity is to reduce it due to quenching, i.e. the removal of heat and possibly active species in its vicinity [53]. Thus, if a combustion wave is situated immediately above the burner rim, then its position will be determined by the relative magnitude of the burning velocity, U_l and the flow velocity, U_g. If the burning velocity is greater than the flow velocity, the flame will move downwards until the burning velocity equals the flow velocity. Alternatively, if the flow velocity exceeds the burning velocity, the flame will lift until the two become equal. Thus, with in certain flow velocity limits, the flame will be held in place above the rim as shown in Figure 3.6.

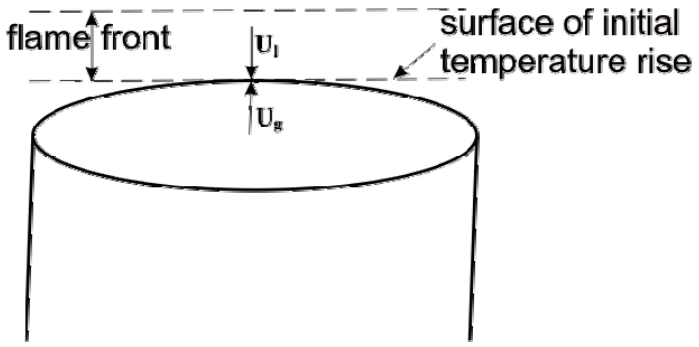

Figure 3.6: Burning velocity and flow velocity for flat flame

The flame is only stabilized on the burner within certain flow velocity limits. Outside these limits; various forms of instability are possible, such as flashback and blow-off. When the premixed-gas flow is low, the burning velocity U_l is greater than the flow velocity U_g over almost the entire cross-section of the burner; hence the flame propagates back down the burner to produce flashback. On the other hand, when the flow is very high, U_g is greater than U_l over the entire cross-section, producing blowoff. When $U_g = U_l$, the flame will keep its position relative to the burner surface, and becomes aerodynamically stabilized.

3.1.6 The governing equations

The primary objective of this subsection is to present the simplified governing equations expressing the conservation of mass, species and energy for reacting flows.

The governing equations in a flame system take the simplest form for steady state one-dimensional flames. In a one-dimensional steady flame at constant pressure, the effects of viscosity, radiation and gravitation are generally neglected [56, 61]. In this case, the governing equations can be written as shown below.

1) The equation of overall conservation of mass

The general equation of mass conservation is seen below in equation (3.2):

$$\frac{\partial \rho}{\partial t} + \nabla \cdot (\rho V) = 0 \tag{3.2}$$

where ρ is density, t is time and V is flow velocity. This equation is often referred to as the continuity equation. To derive the continuity equation of a one-dimensional steady state flame from the general equation (3.2), the conservation of total mass then becomes:

$$\frac{d(\rho V)}{dx} = \frac{dM}{dx} = 0 \tag{3.3}$$

where x is the distance along a stream line to the stagnation point normal to the burner surface. From equation (3.3) it follows that the product of the density and the velocity, the mass flux per unit area, is constant and independent of x.

2) The equation of momentum

$$\frac{d(\rho V)}{dt} = -\nabla P + \mu \nabla^2 V + \rho g \tag{3.4}$$

where μ is dynamic viscosity and g is gravity of Earth

3) The equation of conservation of a particular species

$$\frac{d}{dx}\left[y_i \rho\left(V + V_i\right)\right] = R_i \qquad i = 1,\ldots.n \qquad (3.5)$$

where y_i is the species mass fraction, and V_i is the species diffusion velocity, expressing the molecular transport caused by concentration gradients of species i. When the concentration of i^{th} component is low, Fick's law [56] can be used to calculate Vi. An important property is that the system of equations (3.3), (3.4) and (3.5), contains n linearly independent equations. Because the chemical reaction does not change the elemental composition, the total mass production rate $\Sigma R_i = 0$. Therefore, summation of equation (3.4) over n yields equation (3.3).

4) The equation of energy conversation

The conservation of energy for stagnation point along stream line is expressed as:

$$\frac{d}{dx}\left[\Sigma y_i \rho_i H_i\left(V + V_i\right) - \lambda \frac{dT}{dx}\right] = 0 \qquad (3.6)$$

where H_i is the specific enthalpy of species I, λ is the thermal conductivity coefficient, and T is the temperature. The conservation of energy states that the sum of energy transport by means of convection (first term), diffusion (second term) and conduction (third- term) must be equal to zero. With proper choice of the boundary conditions for one-dimensional flame, it is possible to solve the governing equations [56].

5) The equation of state

The equation of state for compressible flow is given by:

$$P = RT\Sigma \frac{m_i \rho}{M_i} \qquad (3.7)$$

Where P is the pressure, R is the universal gas constant and M_i is the molar mass of species i, assuming that the dependence of the diffusion velocity V_i on the flame temperature and the species concentration is known, the above described system

consists of (n+1) linearly independent equations and contains (n+2) unknown parameters: y_i, v, ρ and T. Thus, the system contains more unknown parameters than equations and a solution is only possible if one of the parameters is specified, or if an extra equation is added to the system, such as the equation for the conservation of energy.

3.2 Impinging flame jets

In this section, the flow characteristics of an impinging flame jet are presented. Then, heat transfer from an impinging flame jet is explained in more detail.

3.2.1 Impinging flame jets structure

The flow structure of an impinging axisymmetric flame jet on a flat plate is basically divided into four characteristics regions: the flame jet region, the free jet region, the stagnation region and the wall jet region. A generalized picture of a single circular flame jet is shown schematically in Figure 3.7.

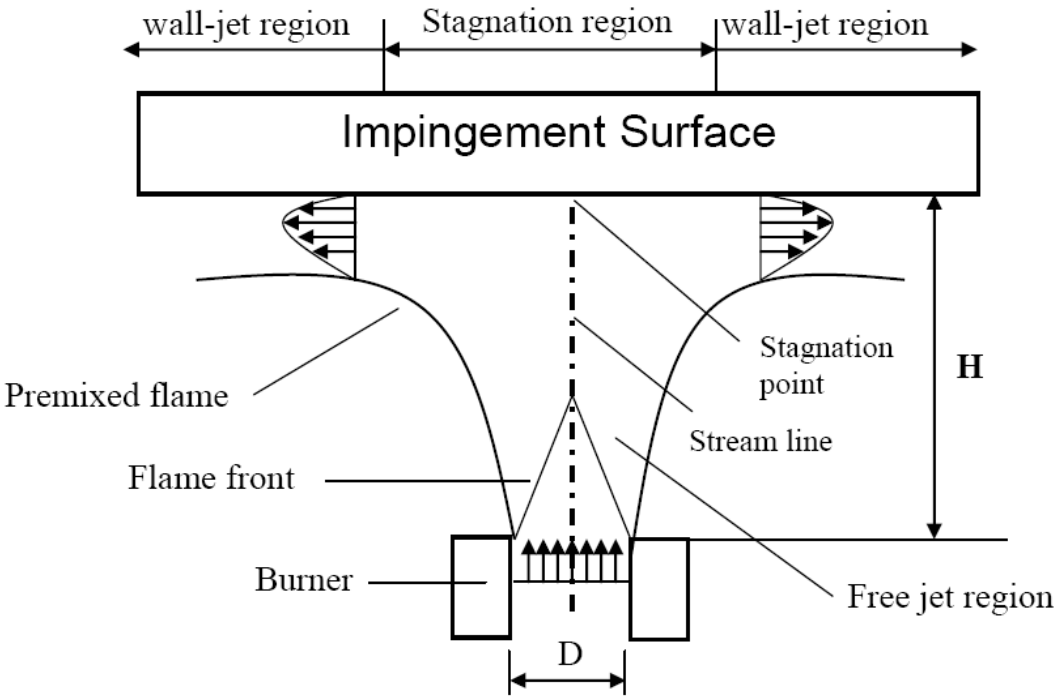

Figure 3.7: Schematic overview of a stagnation flame impinging on a plane surface

Once an unburned gas mixture exits the burner nozzle, it enters the flame jet region. Thus, it faces a sudden expansion as the gases react in the flame front. Then, the resulting burnt gas mixture enters the free jet region. The free jet region potentially consists of a core and a fully developed region. The potential core plays an important role in ignition and flame stability. The fluid in the potential core is not affected by contacting with surrounding fluid, and has characteristics such as the flow in the nozzle [62]. The jet flow in the fully developed region is of a constant velocity profile. In general, in a free jet region, the velocity remains constant for the laminar case if the plate has no perceptible influence on the flow. The stagnation region is also known as the impingement region. The stagnation region is characterized by a pressure gradient, in which the velocity of the mixture decreases in the axial direction due to the influence of the plate on the flow. Also, the static pressure distribution around the impingement surface is used to determine the extent of the stagnation region. Close to the plate, a viscous boundary layer will develop that has approximately a constant thickness in the impingement zone [63]. Once the jet turns in a radial direction and the gases enter the wall jet region, the viscous boundary layer thickness will increase.

Furthermore, the characteristics of the stagnation flow region depend strongly on the separation distance between the burner and the plate. In the wall jet region the fluid spreads out radially over the surface in a decelerating flow. The wall jet region has been regarded as half a free jet, with an inner layer near the wall [64]. In this zone, the temperatures are relatively low due to a fuel-lean combustion, with excess ambient air entrained [21, 65].

Figure 3.8 illustrates the flow structure of an impinging axisymmetric flame jet on a cylindrical surface. In this case, the flow structure can also be divided into four regions: the flame jet region, the free jet region, the stagnation flow region, and the wall jet region. The free jet region and flame jet region are approximately independent of the impingement surface shape. Therefore, the free jet region and flame jet region are similar to those obtained from flame impinging on a plane surface. On the contrary, the average flow field in the stagnation region is dependent

of the shape of the impingement surface. As the fluid approaches the front side of the cylinder, the fluid pressure rises from free stream value to the stagnation point value. The high pressure forces the fluid to move along the cylinder surface and boundary layer develop on the both sides. As is well known from the literature [66], the laminar boundary layer over the front stagnation point of a cylinder in cross-flow is the thinnest and its thickness increases with displacement downstream. Separation of the laminar boundary layer takes place when low velocity fluid close to the tube wall cannot overcome the adverse pressure gradient over the rear portion of the cylinder and eventually the flow stops and begins to move in the opposite direction. Fluid movement starts to curl and gives rise to vortices that shed from the tube. The flow pattern is dependent on the Reynolds number. At low Reynolds number (Re < 4) the fluid completely warps around the body. At higher Re numbers, the fluid is too fast to remain attached to the surface as it approaches the top of the cylinder. Thus, the boundary layer detaches from the surface, forming a wake behind the body. This point is called the separation point.

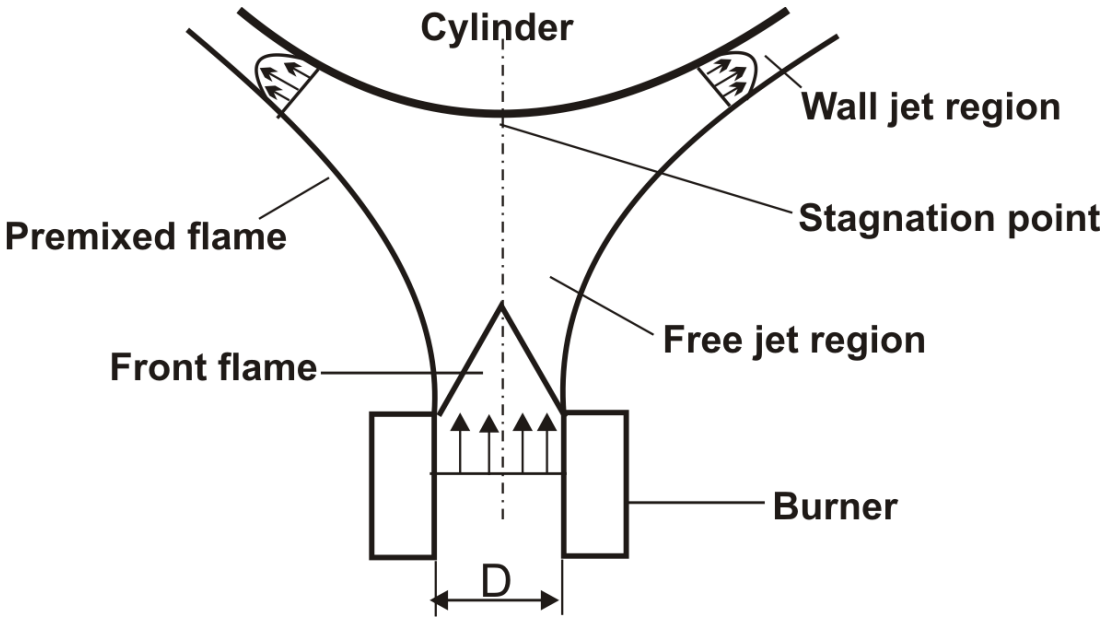

Figure 3.8: Schematic overview of a stagnation flame impinging on cylindrical surface

During the flow of a fluid normal to objects, such as cylinder and a plane surface, the solid wall of the object exerts drag on fluid. For flow over cylinder, the total drag is generated by the friction forces and pressure forces acting on the wall surface. At very low Reynolds number, the drag is mainly due to friction. With an increase of Reynolds number the contribution of the inertia force begin to grow so that at high Reynolds numbers the skin friction constitutes just a few per cent of the total drag. For a plate whose surface is perpendicular to the oncoming flow, all of the drag results from unbalanced pressure forces, with no contribution from fluid friction. One way of expressing drag is by using drag coefficients. The drag coefficient is a dimensionless number used to represent the overall effects of shape, inclination, and other flow conditions. The drag coefficient is defined as follows:

$$C_D = \frac{F_D}{\frac{1}{2}\rho U_\infty^2 A} \tag{3.8}$$

where F_D is the drag force, ρ is the fluid density, U_∞ is the free stream velocity and A is the projected area of the object. Different shaped objects with same Reynolds number and identical frontal area can have very different drag force and drag coefficients. In the range $4\times10^3 \leq Re \leq 1.5\times10^4$, C_D is about 2.0 for a flat plate perpendicular to flow . For cylinder in cross flow, C_D is about 1.2 [67].

The structure of an impinging hot air jet is relatively simple than, but is rather similar to that of impinging flame jet. The major difference between these jets is the existence of a reaction zone in the stagnation region and viscous boundary layer. Relatively a few researchers have studied the structure and aerodynamics of the flame jet and the isothermal air jet. Milson and Chigier [21] found that the pressure distribution and the axial velocities of a flame jet were similar to those obtained with an isothermal air jet. As reported by Viskanta [62] in his review that the aerodynamic of a single impinging flame jet is similar to those of an isothermal air. In his experiments, Van der Meer [2] showed that the radial velocity gradient for the isothermal and flame jet at the stagnation point are found to be equal.

One big difference however exists between flame jets and isothermal jets if we look at the heat transfer mechanisms for these jets. The main heat transfer mechanism for impinging flame jets is forced convection. Increasing the oxidizer composition results in a higher flame temperature and burning velocity and therefore a higher gas velocity. Not only forced convection will be enlarged, but the heat transfer mechanism called thermochemical heat release starts to play an important role [32]. These flames contain a lot of free radicals such as O, H and OH. When these radicals enter the cold boundary layer, they exothermically recombine and augment the heat transfer. This process has also been called chemical recombination or convection vivre. In the following subsections several heat-transfer mechanisms will be discussed more extensively. Let us first consider some non-dimensional numbers that are commonly used in heat transfer analysis:

The Reynolds number (Re) gives a measure of the ratio of the inertial force to the viscous forces in a flow:

$$\mathrm{Re} = \frac{\rho U \ell}{\mu} = \frac{U \ell}{\nu} \tag{3.9}$$

Here, ρ the fluid density $\left(\mathrm{kg/m^3}\right)$, U the fluid velocity, ℓ the characteristic length scale (usually the diameter of burner), μ the dynamic viscosity $[\,\mathrm{kg/(m \cdot s)}\,]$ and the ratio $\nu = \mu/\rho$ is termed the kinematic viscosity $[\,\mathrm{m^2/s}\,]$. The Reynolds number is used to check whether the flow is laminar or turbulent. For turbulent flows, the Reynolds number will be high. The Reynolds number will be low for laminar flows, while a transition flow appears in between. When the Reynolds number is below 2,500, an impinging jet is considered to be laminar [68].

The Prandtl number (Pr) determines the ratio of momentum diffusivity (kinematic diffusivity) to thermal diffusivity. It is defined as:

$$\mathrm{Pr} = \frac{\nu}{\alpha} = \frac{C_p \mu}{\lambda} \tag{3.10}$$

Here, $\alpha = \lambda/(\rho \cdot C_p)$ is the thermal diffusivity (m^2/s), with λ the thermal conductivity $[w/(m \cdot K)]$ and C_p the specific heat at constant pressure $[J/(kg \cdot K)]$. The Prandtl number contains no length scale in its definition and is dependent only on the fluid and the fluid state.

The Nusselt number (Nu) is defined as the ratio of the convective to the conductive heat transfer rates:

$$Nu = \frac{h\ell}{\lambda} \tag{3.11}$$

with h the heat-transfer coefficient [W/(m^2·K)]. The Nusselt number is typically a function of Re and Pr for forced convection flows and is used to determine the convective heat-transfer rate.

The stagnation point heat flux can be correlated in terms of a relationship between the Reynolds number and the Nusselt number. As mentioned previously, the heat flux is determined from Fourier's law by evaluating the temperature gradient at the surface:

$$q = -\lambda \frac{dT}{dx} = -\lambda \frac{\Delta T}{\ell} \frac{dT}{dx} \tag{3.12}$$

where T and x are the non-dimensional variables of temperature and position and q (W/m^2) is the heat transfer rate in the x direction per unit area perpendicular to the direction of transfer. The heat flux can also represented in terms of a heat transfer coefficient in a form of Newton's law of cooling as:

$$q = h\Delta T \tag{3.13}$$

Combining these provides a relationship for the Nusselt number, which is a non-dimensional heat-transfer coefficient:

$$Nu = \frac{h\ell}{\lambda} = -\frac{dT}{dx}$$

Equivalence Ratio is a comparison of the actual fuel/oxidant ratio to the stoichiometric one, i.e.

$$\phi = \frac{(\text{Fuel/Oxidant})_{\text{actual}}}{(\text{Fuel/Oxidant})_{\text{stoich}}} \tag{3.14}$$

The equivalence ratio, ϕ, is commonly used to indicate quantitatively whether a fuel-oxidizer mixture is rich $(\phi \rangle 1.0)$, lean $(\phi \langle 1.0)$, or stoichiometric $(\phi = 1.0)$.

3.2.2 Heat transfer mechanism of the impinging flames

The heat transfer characteristics of the impinging flames on water cooled surfaces appeared to be relatively complex and there were several heat transfer mechanisms reviewed in the literature. Six heat transfer mechanisms have been identified in previous studies [4, 69]. These mechanisms include convection (forced and natural), conduction (steady-state and transient), radiation (surface, luminous, and non-luminous), thermochemical heat release (TCHR) (equilibrium, catalytic, and mixed), boiling (internal and external) and water vapor condensation. These mechanisms are shown schematically for a water- cooled target in Figure 3.9.

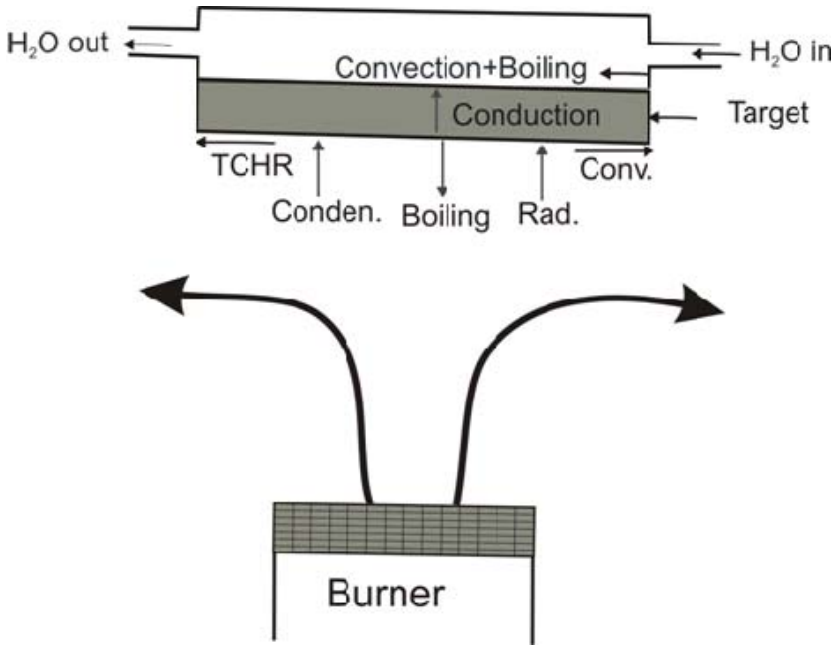

Figure 3.9: Heat transfer mechanisms in flame impingement on a water-cooled target.

It has been verified that forced convection is the predominant mechanism and naturel convection is only important in the case of very low velocity flame. TCHR contributes a large fraction of the total heat flux when the oxidizer is pure oxygen. Surface radiation plays a significant role for applications where the target is located inside a hot furnace. Condensation occurs when the temperature of impingement surface is lower than the dew point temperature of the combustion gases. Boiling does not occur unless the impingement surface is hotter than the jet. The importance of each mechanism varies significantly with the operating environment and a general discussion of them will be given in the following subsections.

3.2.2.1 Convection

Convection heat transfer is caused by fluid motion past a material**,** where the fluid is either at a lower or higher temperature than the material. In a flame impingement heating application, the fluid is mostly at a higher temperature than the medium. Convection is not really a detached mode of heat transfer, but rather a subgroup of conduction due to the fact that the energy still conducts from the fluid to the material. Convection can be forced by movement of a fluid by means other than buoyancy forces; this is called forced convection. In some cases, natural buoyancy forces alone are entirely responsible for fluid motion when fluid is heated, and this is called natural convection. Force convection is the dominant mechanism for flames with temperatures up to 1700 K [70]. Burner exit velocities typically are high enough, so buoyancy effects can be neglected. For such a low temperature flame impingement with no furnace enclosure, the share of forced convection may be 70 − 90% [21, 65]. Therefore, for these flames, forced convection has generally been the only mechanism considered. The heat release from flame chemical reactions at or near the target is not taken into account for this case; therefore, this mechanism is sometimes referred to as frozen flow [71].

Previous studies found that the convection heat transfer depends on several factors, such as the separation distance between burner and target, the aerodynamic of the jet, the stoichiometry, the shape of the target, the fluid-oxidizer combination, recombination of radicals at the target and whether the jet is a premixed or diffusion

flame [62]. The results of experiments [72] show that the equivalence ratio influences the local heat flux distribution, because it impacts the entire combustion process. Also, the effect of the equivalence ratio was studied by Hargrave et al. [24]. The results show that variations in equivalence ratio away from approximately stoichiometric conditions lead to a shifting of the flame reaction zone downstream and to a decrease in the maximum rate of heat transfer from the flame.

3.2.2.2 Conduction

Heat conduction is the transfer of heat energy by microscopic diffusion and collision of particles or quasi-particles within a body due to a temperature gradient. Thermal conduction is often disregarded when evaluating heat transfer in combustion system. Although it is not an important heat transfer mode in the combustion space, it is important in identifying the heat loss through the refractory wall. Furthermore, thermal conduction has played an important role in many flame impingement heating applications. In a number of applications, e.g. rapid reheat furnaces, high thermal conduction rates are preferred. Here, the main target is to raise the temperature of metal parts. Because metals mainly have a high thermal conductivity, heat can be rapidly conducted via the parts. This minimizes the temperature gradient between the outer and inner surface of the part. Accordingly, the higher temperature gradient could lead to damage or deformation of the part. In other applications, e.g. thermal spallation, low thermal conduction is preferred. In this process, a high-intensity flame impinges directly on a solid that has a low thermal conductivity. The heat transfers slowly into the solid, due to its low conductivity. The surface is very hot. Just below the surface, the solid is near ambient temperature. This results in very large internal temperature gradients, which produce high thermal stresses. These stresses cause the solid to fracture. Besides transferring the heat through the target, conduction has been used to measure the heat flux in flame impingement experimental studies. Therefore, in our present study, conduction heat flux through the impingement walls was determined. The heat flux of one-dimensional flat premixed flame was determined from Fourier's law of conduction by evaluating the surface temperatures on both sides of the impingement wall. Different impingement walls are used, i.e. flat plate and cylinder. The local heat flux $\dot{q}$ at the stagnation

point of the impingement wall, which is equal to the amount of heat transfer by convection from the flame to the wall under a steady flow condition, is given by:

For flat wall: $$q^{\cdot} = \frac{Q}{A} = -\lambda \frac{\Delta T}{L} \quad (3.15)$$

For cylindrical wall: $$q^{\cdot} = \frac{Q}{A} = -\frac{\lambda \Delta T}{r \ln(r_2 / r_1)} \quad (3.16)$$

Where λ is the thermal conductivity, L is thickness of the flat wall, r_2 is the outer radius of cylinder, r_1 is the inner radius of cylinder and ΔT is the temperature difference.

3.2.2.3 Radiation

Radiation is a unique heat transfer mechanism as no medium is required for energy transport — it can be transmitted through a vacuum or through a medium. Radiation is simply the transmission of energy by electromagnetic waves. In the heating process, the effect or radiation is highly dependent on whether the target is isolated or placed in an enclosure. There are two main components that contribute to the thermal radiation heat transfer at the target surface, if the target isolated: nonluminous radiation and luminous radiation. Luminous flames are produced by the continuous radiant emission of particles in the flame, such as soot.

Nonluminous radiation is produced by gaseous combustion products such as carbon dioxide and water vapor. These are two of the main constituents in the products of combustion of typical hydrocarbons. Nonluminous radiation is commonly small compared to convective even at high flame temperatures, as the emissivity of the gases is very low. Luminous radiation is produced by continuous radiant emission of particles in flame, such as soot, which are nearly as radiant blackbodies. This mechanism is usually only important for liquid and solid fuels. It is not usually important if gaseous fuels are combusted, except when diffusion flames are applied or if the flames are very fuel- rich. In most previous studies, which used gaseous

fuel, the effect of radiation heat transfer from non-luminous flames has been neglected [4, 24, 73, 74]. Milson and Chigier [21] found that pre-mixed methane/air flames were entirely non-luminous as compared to methane diffusion flames. In their experimental works, Dong et al. [14, 17] ignored the influence of radiation in the case of flame impingement heating, stating that the contribution is very small. Van der Meer [2] reported that non-luminous radiation is negligible due to the very low emissivity of a hot gas layer of small thickness. However, few studies show that nonluminous radiation quantity is a significant part of the total heat flux to the target [75].

3.2.2.4 Thermochemical Heat Release

This mechanism of heat transfer indicates the exothermic release of energy from reacting gases during cooling. It is called Thermochemical Heat Release (TCHR). This name includes the aspects of chemical reaction and exothermic energy release. In many combustion processes, the products usually contain dissociated species. The level of such dissociation rises as the flame temperature increases. When a flame impinges on a cool target, these species diffuse in the direction of the concentration gradients, toward the lower temperature regions. Hence, these species cool down and exothermically recombine into more stable products, while simultaneously releasing energy. The amount of this energy depends mainly on the flame temperature. At the adiabatic equilibrium temperature of 3054 K, the sensible energy and chemical energy are nearly the same [71]. Therefore, at a high gas flame temperature, TCHR is approximately of the same order of magnitude as force convection.

Three chemical mechanisms are identified that imitate the thermochemical heat release: equilibrium TCHR, catalytic TCHR and a mixed TCHR. Equilibrium TCHR plays a main role when the reaction time scale is much less than the diffusion time scale. In this mechanism, the chemical reactions take place in the boundary layer. In the case of catalytic TCHR, the chemical reaction times are much greater than the transit time for the diffusing species to reach the surface. There is insufficient time for the radical species to react before reaching the surface. In this case, recombination may take place at the surface. Mixed TCHR is a combination of

equilibrium and catalytic TCHR. Nawaz [76] showed that a combination of equilibrium TCHR and catalytic TCHR can occur as well. In this case, the chemical reaction time scale is of the same order of magnitude as the diffusion time scale. Some of the dissociated species react in the boundary layer; others react catalytically at the surface.

Similarly to the flat plate, for flame impingement on a water-cooled cylinder, the above mentioned heat transfer mechanism also exists. However, unlike jet impingement on a flat surface, flow fields in axial and angular direction are different for cylindrical surfaces resulting in considerable difference in the heat transfer characteristics. The heat transfer coefficient varies around the perimeter of the cylinder in cross flow, with the greatest local heat transfer coefficient at the leading stagnation point. At the rear of the cylinder, the heat transfer coefficient is the lowest due to boundary layer separation in the wake of the flow. Flame impinging normal to a flat plate and normal to cylinder have been studied experimentally by numerous investigators (see chapter two), and several empirical correlations have been developed for the heat transfer coefficient. For the Nusselt number in the stagnation point, Kays [77] gave this equation:

$$\mathrm{Nu} = 0.763\,\mathrm{d}\left(\frac{\beta}{\nu}\right)^{\frac{1}{2}}\mathrm{Pr}^{0.4} \tag{3.17}$$

where β is the velocity gradient outside the boundary layer and ν is the kinematic viscosity. For a cylinder and plane surface the values of β are known, leading to the corresponding stagnation point heat transfer results:

Cylinder: $\beta = \dfrac{3.63\,U_\infty}{d}$ $\mathrm{Nu} = 1.09\ \mathrm{Re}^{0.5}\,\mathrm{Pr}^{0.4}$ (3.18)

Plane surface: $\beta = \dfrac{3.63\,U_\infty}{d}$ $\mathrm{Nu} = 0.763\ \mathrm{Re}^{0.5}\,\mathrm{Pr}^{0.4}$ (3.19)

where U_∞ is the uniform flow velocity.

In this current work, according to an analysis of the heat transfer mechanism involved in the present gas-fired impinging flame jet system, heat transfer due to condensation and TCHR can be considered negligible. The heat transfer of the system can be described as in Figure 3.10. From Figure 3.10, it can be clearly seen the types of heat transfer mechanisms: conduction, convection and radiation. On the water-side of the impingement plate, the boundary temperature can be considered to be uniform because the cooling water is maintained at uniform temperature through experimental investigation. For the edges of the impingement plate, the boundary condition is assumed to be a thermally isolated surface because of the negligible thickness. On the flame-side of the impingement plate, convection and radiation heat transfer play a dominant role. In view of the of the negligible heat loss to the surroundings, it can be assumed that for the present system, heat transfer by conduction through the impingement plate will be equal to the total heat transfer by convection and by radiation to the flame-side of the plate.

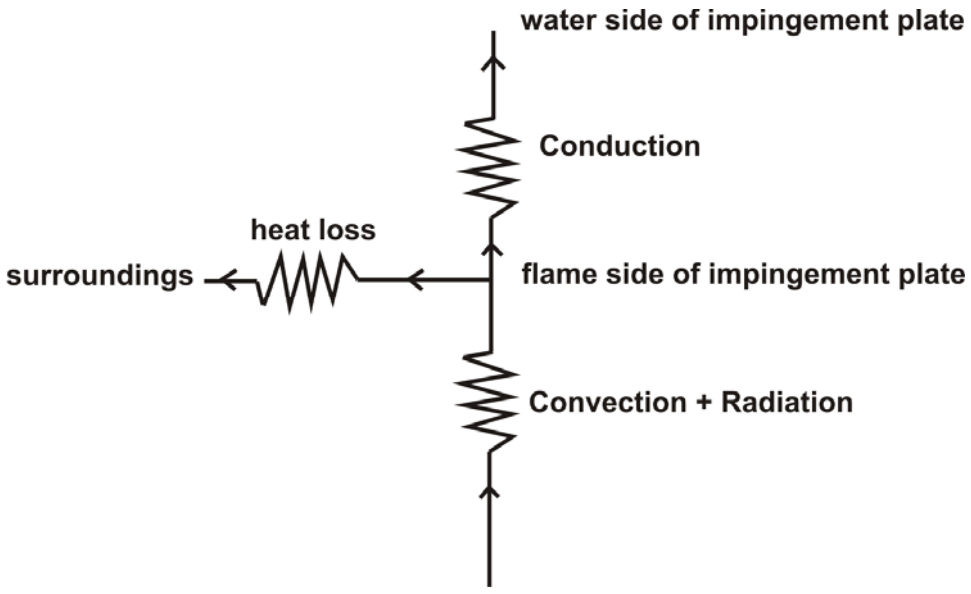

Figure 3.10: Heat transfer mechanism of the impingement flame jet system

3.3 Temperature measurement methods

In this section, an overview of common temperature measurement methods is given, including working principles, and advantages and disadvantages of those methods

3.3.1 Introduction

Temperature measurement in today's industrial environment encompasses a wide variety of needs and applications. Hence, the accurate measurement and the control of temperature become of great importance. The proportion of the temperature sensor is estimated to be 75%-85% of the total sensors produced worldwide [78].

To measure and compare the temperature, it is necessary to define a measuring scale. Alongside some common and widespread empirical temperature scales, which were set arbitrarily as the Celsius scale (°C) or Fahrenheit scale (°F), there is the thermodynamic temperature scale. The unit of thermodynamic temperature is the Kelvin (K) and is defined in terms of the interval between the absolute zero and triple point of pure water, 273.16 K; Kelvin, is the fraction 1/273.16 of that temperature [78, 79]. The current international temperature scale, ITS-90 [79], defines a scale of temperature in five overlapping ranges. These are:

1. 0.65-5 K using vapor pressures of helium,
2. 3-24.5561 K using gas thermometer with constant volume,
3. 13.8033-273.16 K using the ratio of platinum resistor to other material resistor at its triple point,
4. 273.15-1234.93 K using platinum resistance thermometers calibrated at fixed freezing and melting points, and
5. above 1234.93 using the Planck law of radiation.

As already indicated in the previous section, there are different methods of measuring temperature. Thus, it is possible to use inter alia to measure the temperature such as; thermoelectricity, temperature dependent variation of the resistance of electrical conductor, fluorescence properties and spectral characteristics. Additionally, temperature measurement techniques may require direct contact with the medium. Alternatively, this may not be possible or desirable; and a noninvasive method may be used. Therefore, according to the nature of contact

between the measuring device and the medium, various measurement techniques can be classified into three categories: invasive, semi-invasive and non-invasive.

3.3.2 Invasive measurement method

In this method, the temperature sensors require direct contact with the medium of interest, e.g., a thermocouple in a gas stream. The disadvantage is that the measurement environment is disturbed and so the results will be incorrect. In addition, an invasive sensor measures only its self-temperature and not that of the measurement object. The most common invasive measurement methods not include only the instrument-based ones on thermal expansion, but also thermoelectric sensors and devices based on the change in electrical resistance. Besides these methods, there are also semiconductor devices, which have temperature-dependent characteristics, as well as the noise thermometry[78, 80].

3.3.3 Semi-Invasive measurement method

As mentioned in the previous section, in many applications the contact between the measuring instrument and the medium is not desirable. In those cases, semi-invasive measurement technique is used. This technique is usually applied to some of the temperature-sensitive material on the surface. The change of surface coating optical properties can be observed remotely. These surface coating methods are classified as semi-Invasive, since the technique involves modification of the component of interest and therefore some disturbance to the temperature field [78]. There are several heat-sensitive materials, including thermochromic liquid crystals, heat-sensitive crystalline solids and paints, and thermographic phosphors. They are available for a temperature range of 40 ° C to 1350 ° C and have uncertainty of ± 5 ° C [78].

3.3.4 Non-Invasive measurement method

The disadvantage of invasive and semi-invasive measurement methods lies in the exposed environmental conditions of the measurement object. For example, measurement of temperature in very hot mediums such as flames or plasmas represents a particular challenge. Not all measuring devices have the capability to

survive in such conditions. This is a major advantage of non-invasive methods, because they are not bound by this constraint. Similar to the semi-invasive methods, they can be useful in detecting the temperature of moving components. It is possible to use them over a large distance because there is no need for contact with the measured object. The majority of non-invasive techniques measure temperature based on the electromagnetic spectrum. This method is relatively more expansive.

As demonstrated in previous sections, there are a wide variety of temperature measurement methods. Each method has its advantages. Thus, individual methods can be applied where others fail or if they offer higher measurement accuracy of less than ±1K. Thermographic phosphors offer new possibilities in comparison to other methods. Thermographic phosphors, for example, allow for measurements in the glowing media, where conventional pyrometers fail. In this method, further knowledge of the emissivity is not necessary and thus reduces measurement errors. In similar environmental conditions such as flame impingement, it is assumed that measuring the surface temperature could be improved by replacing the traditional methods with thermographic phosphor. Hence, this study chose thermographic phosphor. The basic principle of thermographic phosphor is discussed in the following section.

3.4 Thermographic phosphor

This section introduces the fundamental physics of thermographic phosphor. It will attempt to explain various responses that change with temperature, giving phosphors their sensing properties.

3.4.1 Introduction

The thermographic phosphor is composed of a host material that is doped with some activator material. The activator is often a rare earth or transition metal ion. The doping concentration should be small enough to ensure that the activator atoms are isolated from each other by the host matrix. The host material is generally translucent to radiation.

Activators are mostly responsible for absorption and emission of this radiation. Thermographic phosphors are usually produced as a powder and then fixed to the surface with an adhesive. The disadvantage of this method is that the particles partially do not stick well. Also, most adhesive materials cannot survive at high temperatures. In addition, when applying the powder, the layer thickness is difficult to control. Thus, in this present work, thermographic phosphors were directly deposited using a thin film technology method, i.e. the sol-gel method [81]. The sol gel method is a wet chemical deposition process for preparation of thin films.

Using sol-gel helps avoid all the disadvantages mentioned above. Most of the phosphors used for thermometers are excited by a light source (e.g. laser or LED) to emit light, so that the emitted light phosphorescent can be measured. Phosphor thermometry takes advantage of the thermal dependence of the phosphorescence properties, such as wavelength, intensity and lifetime. Usually the phosphorescence lifetime, also known as decay time, is the parameter that is measured to determine the temperature. This technique offers high sensitivities and accuracies. Therefore, it has been used in different combustion environments (e.g. see[12, 82]).

3.4.2 Physical principles

Luminescence is the phenomena in which electronic states of solids are excited by the light of a particular energy; the excitation energy is released as light. The wavelength of emitted light generally is equal to or longer than that of the exciting light (Stoke's law). This difference in wavelength is caused by a transformation of the exciting light into non-radiative vibration energy of atoms or ions [83, 84].

In luminescence spectroscopy, photons with energy greater than the band gap of the material studied are directed onto its surface. The incident photon beam is partially reflected, absorbed, and transmitted by the material being probed. The absorbed photons create electron-hole pairs in the semiconductor. The electrons are excited to the conduction band, or to the energy states within the gap. These electrons can lose part of their energy that transfers from the conduction band to energy levels within the gap. Photons produced as a result of the various recombinations of electrons and

holes are emitted from the sample surface and it is the resulting photon emission spectra.

There are a number of routes by which an excited electron loses energy. These processes are shown in Figure 3.11, and are widely known as the Jablonski diagram. If the photon emission occurs between levels having the same spin states, e.g., S1 → S0, this is called fluorescence. If the spin states of the initial and final energy levels are different, for example, T1 → S0, the emission is termed as phosphorescence. The phosphorescence is statistically much less likely than fluorescence. The lifetime of phosphorescence is much longer than fluorescence. It can vary from 10^{-3} to 100 sec, while in fluorescence, the life time is typically less than 10^{-8} sec [51]. Apart from these two radiative transitions, three nonradiative deactivation processes are also significant as shown in Figure 3.11.

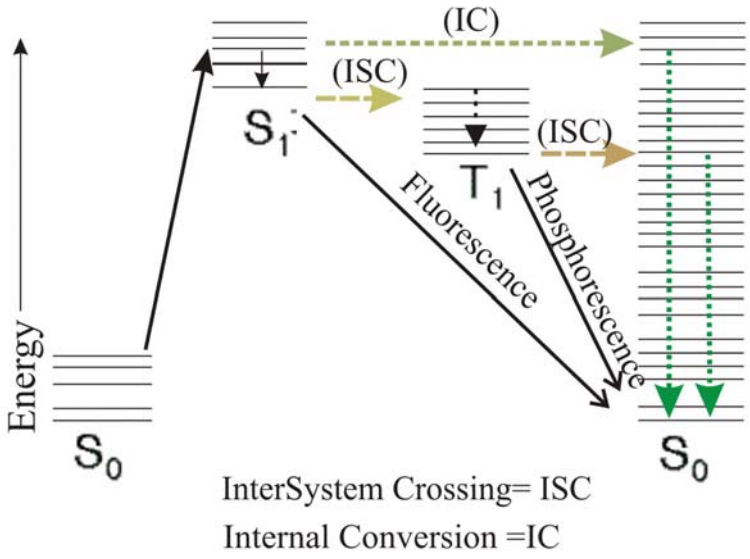

Figure 3.11: Partial energy diagram for a photoluminescence system (Jablonski diagram)

These are internal conversion (IC), intersystem crossing (ISC) and vibrational relaxation. The lifetime, τ, of the emission is determined by the rates, W, of all decay

processes, both radiative and non-radiative. The measured emission intensity *I* is proportional to the rate of change excited luminescence centre N_1

$$I\,\alpha\,\frac{dN_1}{dt} = -\left(W_{Radiative} + W_{non-radiative}\right)\cdot N \tag{3.20}$$

where $W_{Radiative}$ and $W_{Non\text{-}radiative}$ are the transition rates of radiative and non-radiative mechanisms, respectively, N_1 is the number of excited luminescence centers, and the negative sign indicates emission.

The transition are usually treated as a single term, known as the overall lifetime, τ, such that [85]

$$\tau^{-1} = W_{Radiative} + W_{Non-Radiative} \tag{3.21}$$

In general, this lifetime is temperature-dependent. When the excitation source is removed, the number of excited atoms/ ions N1 is governed by the differential equation

$$\tau(T)\frac{dN_1}{dt} + N_1 = 0 \tag{3.22}$$

Where $\tau(T)$ is the electron lifetime, which is a function of temperature that can change in time. Assuming the electron lifetime is constant during the decay, the solution to equation 3.22 is given as

$$N_1(t) = N_1^{\circ}\exp\left(-\frac{t}{\tau}\right) \tag{3.23}$$

Where N_1° is the number of electrons at t = 0, which is when the excitation source is Switched off. By differentiating equation 3.23 and recalling equation 3.20, the intensity can be expressed in terms of decay time as

$$I(t) = I_{\circ} \exp\left(-\frac{t}{\tau}\right) \tag{3.24}$$

where $I_{\circ}$ is the initial emission intensity when the excitation source is removed, at time t = 0. The mono-exponential 3.24 is used to describe the decay phosphor of the intensity in non-contact thermometry. If the temperature is constant, then the decay time τ , which is a function of temperature, also remains constant. The emission intensity of a phosphor at a given temperature is recorded, and the decay time is extracted from the emission data by using fitting procedures.

In this study the chromium–doped aluminium oxide (ruby) is used for the surface temperature measurements. The phosphorescence of ruby is quite strong and can be excited in the green and in the blue spectral range. In addition, it is stable at high temperatures, and its luminescent properties are well known. The temperature of the surface, coated with thermographic phosphor, is determined by measuring and evaluating the lifetime of phosphorescence after LED excitation.

3.5 Summary

This chapter presented the fundamentals of laminar premixed flame, the flow field structure and the heat transfer mechanism of flame impingement both were explained, and an overview of surface temperature methods. In addition, the physical principles of thermographic phosphor were explained. Further details of the experiments, experimental setups and methods used in this study are discussed in the next chapter.

4 Experimental Setup and Methods

This chapter introduces a general description of the experimental setups and the methods that were used in the present work. The first section describes the main experimental setups used for measuring the heat flux from the flame to the wall. These include two main experimental setups: the flame impinging on a flat plate and the flame impinging on a cylindrical surface. In addition, it describes the calibration of some experimental devices, such as mass flow controller, and measuring of the thermal conductivity. In the following sections, the preparation and calibration procedures of the thermographic phosphor coating will be explained. The experimental procedure, lifetime decay analysis and heat flux calculation will also be presented. Particular attention will be dedicated to describing the detailed estimation of experimental uncertainty. Finally, the modeling used will be presented.

4.1 Flame impingement experimental setups

In this section, I present the description of the experimental setups, i.e. flame impinging on a flat plate and flame impinging on a cylindrical surface. These experimental setups are designed to identify the influence of different parameters: cold gas velocity, equivalence ratio, and burner-to-plate distance on the heat flux characteristics of the impinging flame jet. Furthermore, it allows for obtaining more accurate measurements for the surface temperature using the thermographic phosphor technique, and thus a more accurate calculation of the heat flux.

4.1.1 Flame impinging on a flat plate

The experiment was designed in such a way that one-dimensional stagnation point geometry is approximated. The structure of this experiment is composed of two main structural components: the heat receiver as a heat absorption system, and the burner as a heat generation system, as shown schematically in Figure 4.1. Also, Figure 4.2 shows the photograph of this experimental setup.

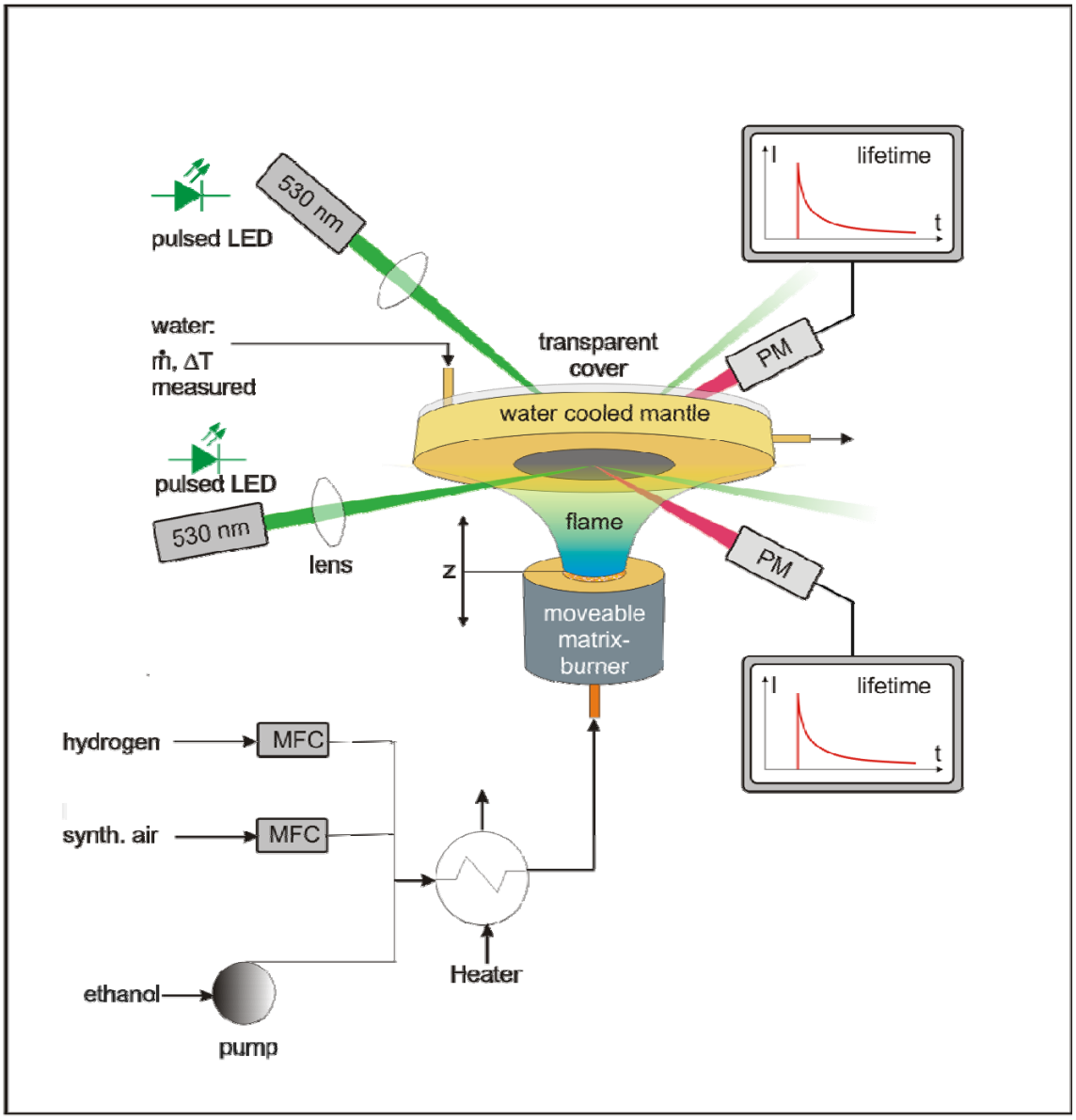

Figure 4.1: Schematic of the flat plate experimental setup

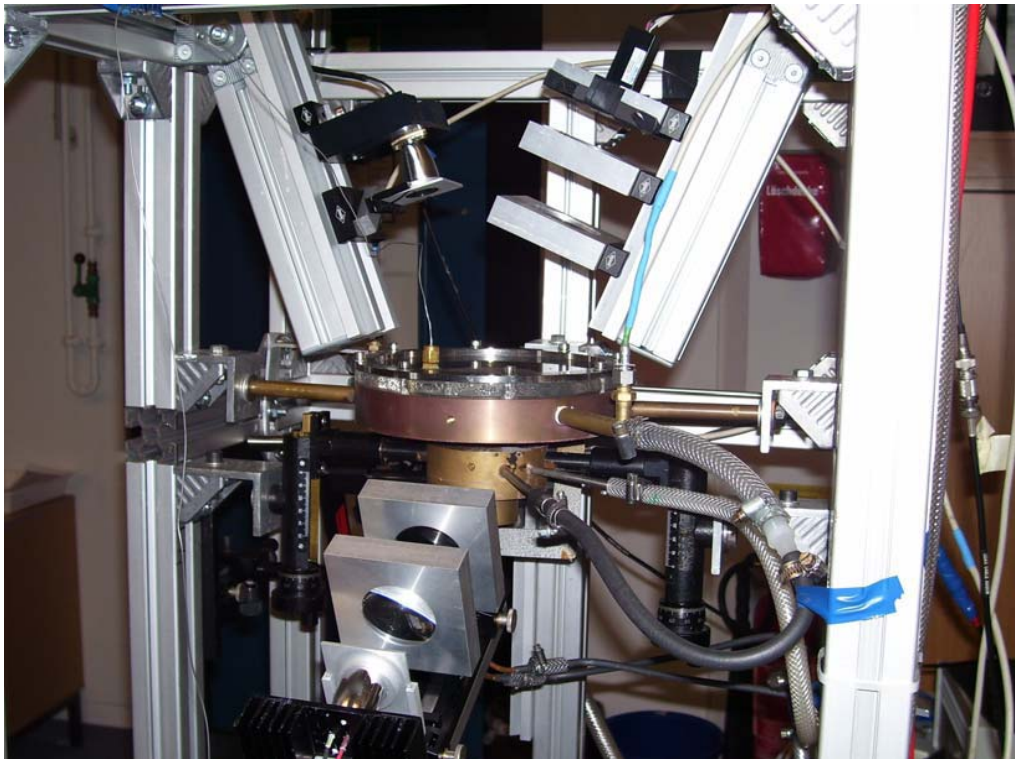

Figure 4.2: the flat plate experimental set up

The flame holder of the heat generation system used in this experiment is a moveable 45 µm sintered bronze type (SKA-B 20) burner with a diameter of 30 mm and with porosity of 38% surrounded by a water cooling jacket. The water jacket is made of brass and provided with circumferential channels for circulating cooling water in a circuitous path around the burner. The burner is attached to a two-dimensional positioner, so the burner has the possibility to be fixed at a desired position relative to the impingement surface.

In this experiment, in an attempt to obtain a laminar one-dimensional flame for different fuel air mixtures velocities, two different burner types were used: a matrix flat burner and a nozzle burner. Like the matrix flat burner, a nozzle burner is equipped with 45µm sintered bronze with a diameter of 30 mm and with porosity of 38% surrounded. The outlet of the nozzle burner has diameter of 20 mm.

A matrix flat burner was used for lower fuel air mixture velocity (0.1 m/s to 0.5 m/s). In this range of velocity or flow rate, a simple one-dimensional flow is observed, as shown in Figure 4.3. Once the flow rates of gas mixture exceed this range, when the cold gas velocity is higher than the free flame velocity, the flames show cellular structures on the matrix burner. Thus, at high flow rates, a simple one-dimensional flow is not observed using the flat burner. For this reason, at higher flow rates, a nozzle burner is more suitable to obtain one-dimensional flow. Thus, in this work, a nozzle burner was used for higher fuel air velocities (0.6 m/s to 0.9 m/s), as shown in Figure 4.4; However, a nozzle burner is not appropriate at a lower velocity, as the flame will stabilize inside the tube.

Figure 4.3: Photograph of flat burner flame (v=0.4 m/s)

Figure 4.4: Photograph of nozzle burner flame (v=0.9 m/s)

In general, the use of both burners helps in providing a one-dimensional flame. Two mass flow controllers (MKS instruments) with a volume of 100, 5 liters were used to control the flows of air and hydrogen respectively, as shown in Figure 4.1. A defined amount of liquid ethanol was continuously fed by a HPLC pump (Knauer Smartline pump 1000) to the evaporator submerged in a thermo-bath (Thermo Haake dc 30), which helps to control the temperature, also as shown in Figure 4.1. In addition, to illustrate more, Figure 4.5 shows a photograph of HPLC pump, evaporator and thermo- bath.

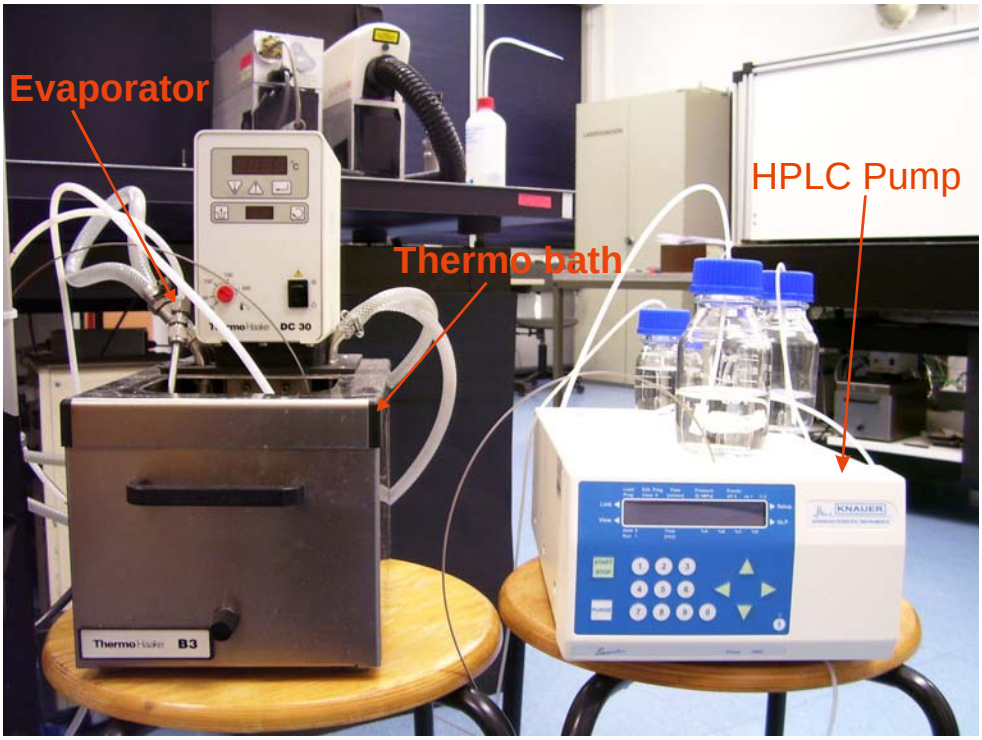

Figure 4.5: photograph of HPLC pump, thermo bath and evaporator

The heat receiver is made of a hollow water-streamed disc of 30 mm thickness, 180 mm inner diameter and 200 mm outer diameter. It has a brass ring as a frame for the ceramic plate on the flame side. The top plate of the cooling-water jacket was made of transparent acrylic glass to enable the water flow to be visible. Furthermore, the acrylic glass allows for a good transparency in the range of the phosphorescence and excitation wave lengths, and is stable in the temperature range of interest (below 120°C on the pressurized water-cooled side).

The ceramic plate, or impingement surface, was evenly cooled on the back side with the pressurized cooling water (ca. 3bar), as shown in Figure 4.1. As a result, the temperature of the heated side of the plate was kept relatively low (T< 520 K). Two flat plates of different ceramic materials were used separately as impingement surfaces to validate and improve the accuracy of measurements. The materials were aluminium oxide (λ=22.2 W/(m·K)) and yttria-stabilized zirconium oxide (YSZ) (λ=2.5 W/(m·K)). These plates were of 6 mm thickness and 80mm diameter, and were coated on the both sides with chromium-doped aluminium oxide (ruby) (1.1% Cr) using the sol-gel method.

For the temperature measurement on the flame side and cooled side, both sides were excited with a green LED array (Opto Technologies Inc., OTLH-0020-GN) at a peak wave length of 525 nm, emitting a typical power of 2.4 W. Two fast pulse generators (Toellner, TOE7404) were used to provide the input for the green LED. Phosphorescence signals from the measurement area, on both sides of the plates, were collected with lenses on to the photomultiplier (PM) tubes (Hamamatsu H6780-03). Spectral filtering of the phosphorescence signal was performed using band pass filters centered at 689 nm (23 nm bandwidth) were placed in front of the photomultiplier tubes. The output from the photomultiplier tube is most often in the form of a weak electric current: that is, the photomultiplier tube is a current generator. This signal was recorded through direct coupling to the digital oscilloscope (Tektronix TDS 2024), and then transferred to a personal computer after typically averaging for 128 pulses.

Inlet and outlet temperatures of the cooling water, upper surface temperature of the ceramic plate (i.e. on the cooling water side), and the flat burner surface temperature were measured with platinum resistance thermometers (PT100) and thermocouples (K-type), respectively. A LABVIEW program was used to measure and record all the mentioned temperatures. The flow of cooling water was metered by a water flowmeter (Interin, FD-1250), and was kept constant (20L/h) for all experiments. The purities of the used chemicals were ethanol 99.5%, hydrogen 99.99% and synthetic air (21% O_2 79% N_2).

As mentioned before, these experiments were designed to identify, respectively, the influence of cold gas velocity, plate-to-burner distance and equivalence ratios on the heat flux of an impinging flame jet.

4.1.2 Flame impinging on a cylindrical surface

The flame jet impingement system was composed of two main parts: the heat generation system and the heat absorption system. This is shown schematically in Figure 4.6. The heat generation system of this experimental setup is similar to the system used in previous setup (for further details see section 4.1.1), which include a burner, an evaporator, thermobath, HPLC pump and gas flow controller.

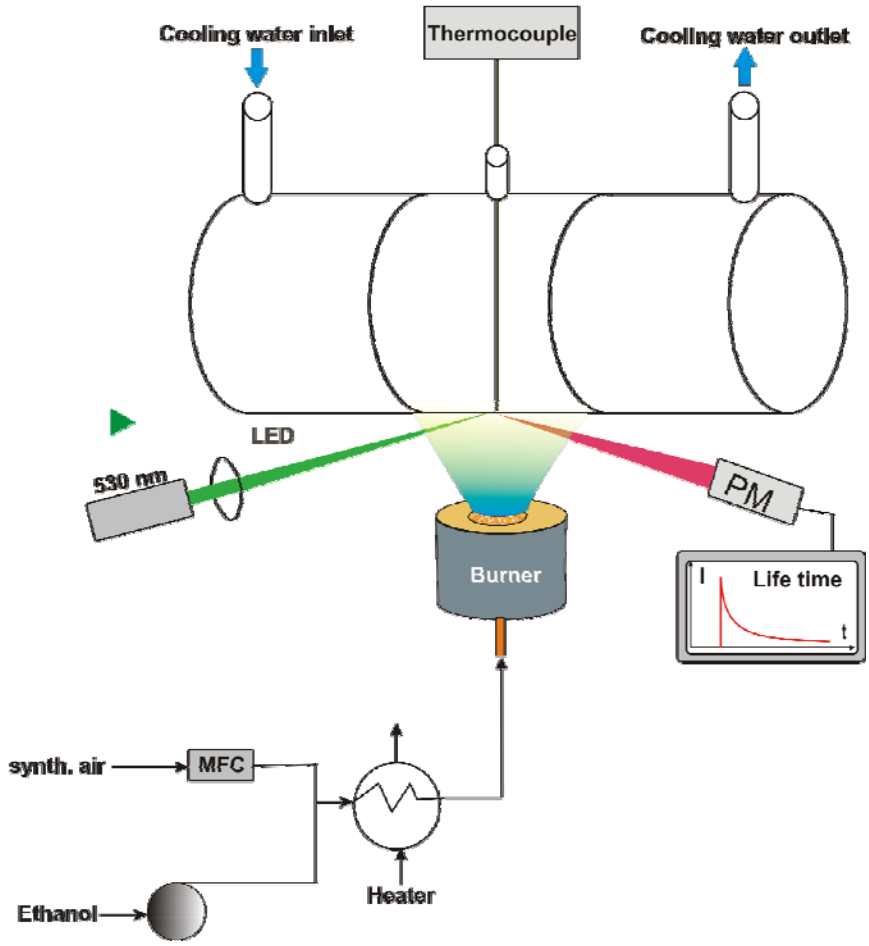

Figure 4.6: Schematic of the experimental setup for flame impinging on a cylinder

The heat absorption system, i.e. the heat receiver system, is made of a hollow ceramic cylinder of 60 mm length, 50 mm inner diameter and 60 mm outer diameter. Two brass flanges are connected to the ceramic cylinder using thermal glue (J-B Weld), which can withstand a constant temperature of 320 C°. Figure 4.7 shows the photograph of the experimental setup for flame impinging on a cylinder.

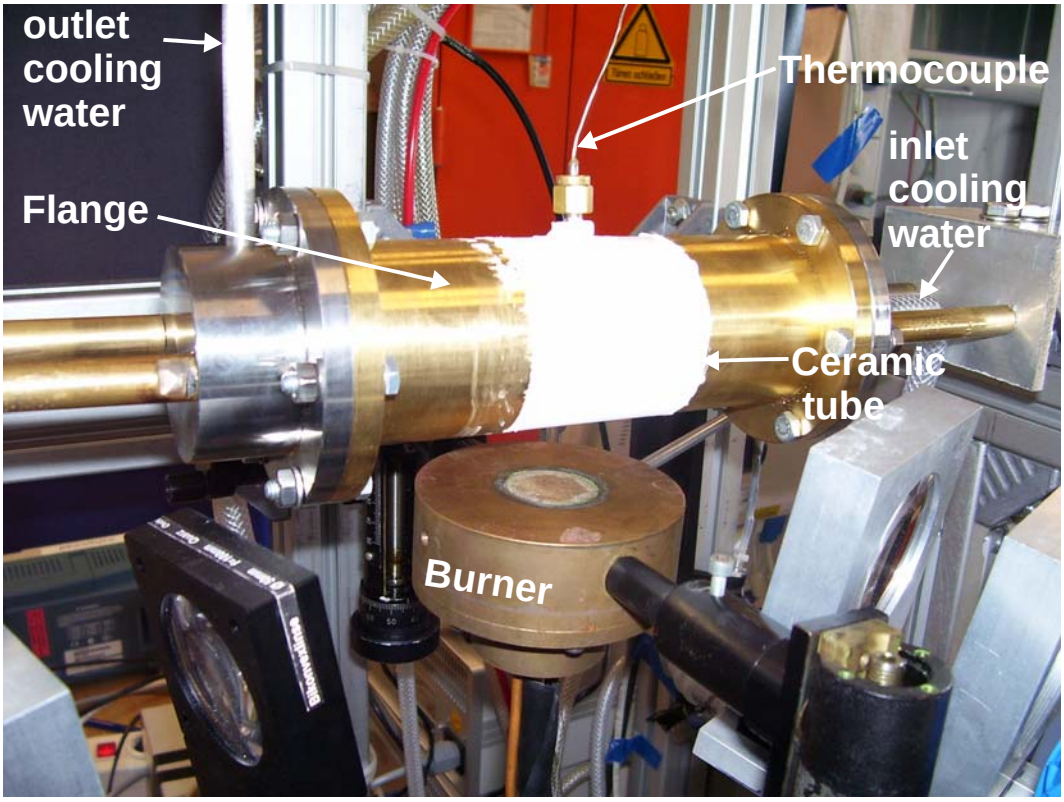

Figure 4.7: Photograph of the experimental setup for flame impinging on a cylinder

The cylinder was drilled from the top to allow the passage of a thermocouple, which is used to measure the temperature of the inner surface at a point corresponding exactly to the stagnation point. The outer surface of the ceramic cylinder was coated with chromium-doped alumina (ruby) (1.1% Cr) using the sol-gel method. The thermal conductivity of the ceramic cylinder was measured using thermal conductivity meter (TCT 426). Axial Flow Methods was used for thermal conductivity testing.

In this, the principle of the measurement lies with passing the heat flux through a known sample and an unknown sample and comparing the respective thermal gradients, which will be inversely proportional to their thermal conductivities. In this work, the unknown is sandwiched between two known samples. The tests were conducted in the temperature range of 20 – 400 C°. The thermal conductivity was nearly constant as at 3.4 W/mK, as shown in Figure 4.8.

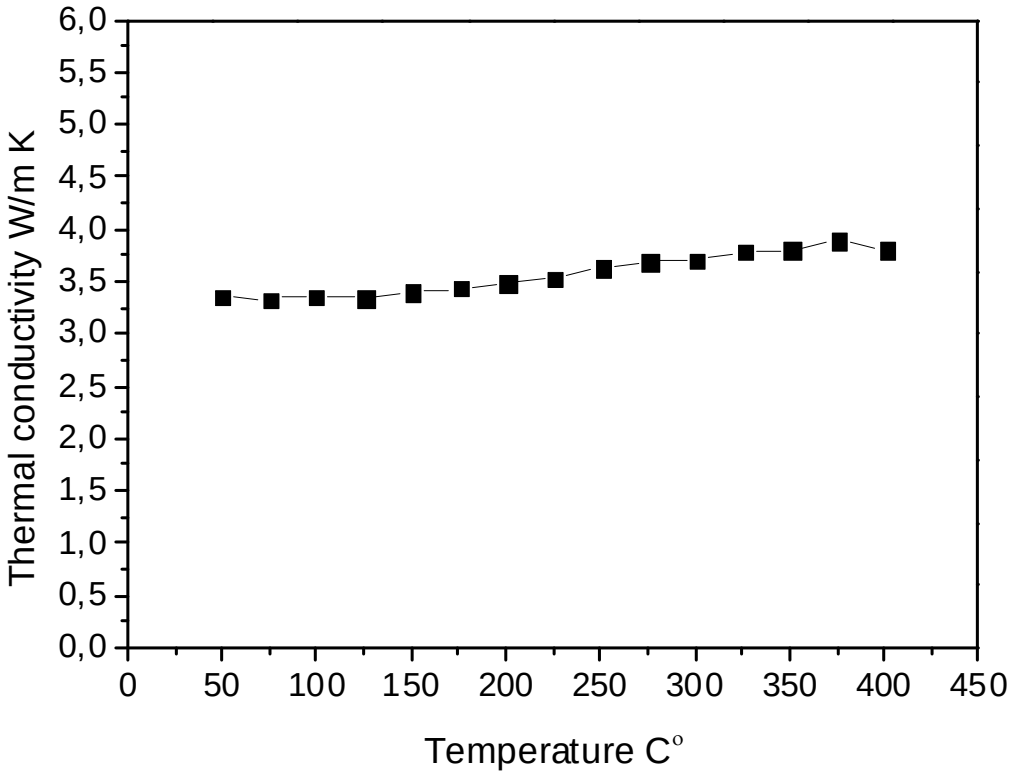

Figure 4.8: Effect of temperature on the thermal conductivity

The inner surface of the cylinder was cooled with pressurized cooling water, and the inlet and outlet temperature of the cooling water was measured using a platinum resistance thermometer (PT 100).

For the temperature measurement on the hot side, or the outer surface, the phosphor coating was excited with a green LED array at peak wavelength of 525 nm, emitting a maximum power of 2.4 W. The rise and the decay time of the LED is in the order of 10ns, which is a magnitude faster than the expected and measured life times. The light was focused using two lenses. The emitted phosphorescence signals from the

measurement area (78mm^2) were focused by lenses through a bandpass filter onto a photomultiplier. Also, as mentioned before, the electronic signal from the photomultiplier tube (PM) was then measured and stored by a digital oscilloscope and transferred to a personal computer after typically averaging for 180 pulses.

4.1.3 Calibration of the measurement instruments

In order to reduce systematic error that is a type of error that deviates by a fixed amount from the true value of measurement, it was necessary to calibrate some of the measurement instruments before starting the experiments. Thus, all gas mass flow controllers were well calibrated using a bubble flow meter (Gilian, the Gilibrator). This device is a high-accuracy electronic bubble flow meter that provides instantaneous air flow readings and a cumulative averaging of multiple samples. It was found that the errors were less than 6% for all gas mass flow meters. For example, the calibration curve of the gas mass flow controller 1179B (0.01-20L/min) is shown in Figure 4.9.

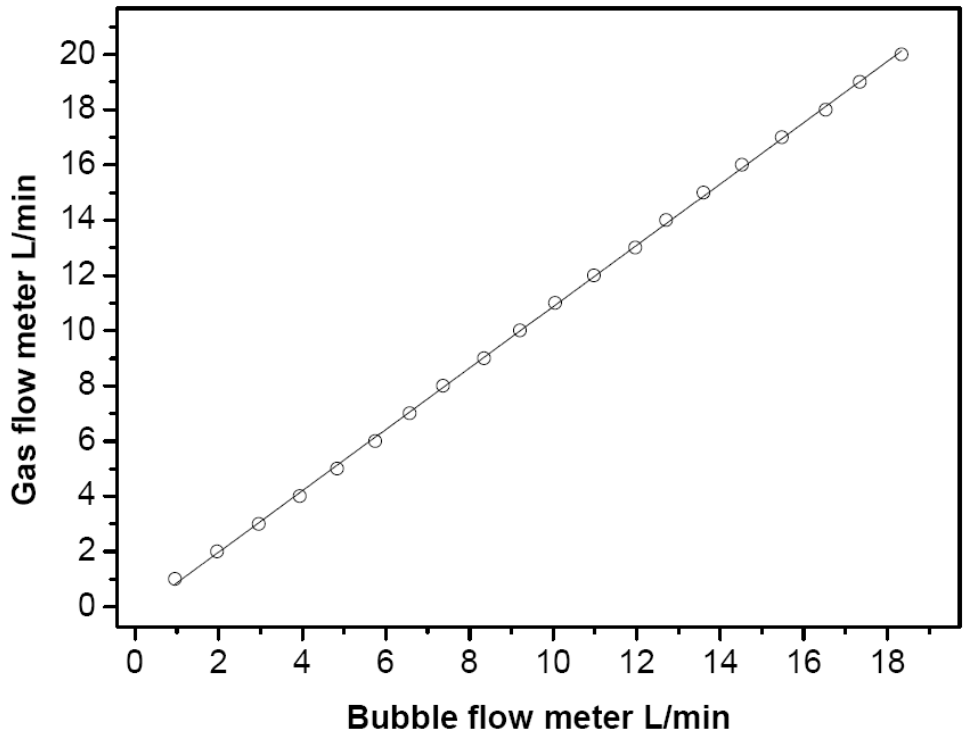

Figure 4.9: Calibration curve of gas mass flow controller 1197B (0.01-20L/min)

Also, to observe any fluctuating in cooling water flow rate, water flow monitoring was performed using an impeller flow sensor, which was installed after the outlet of the water flow controller.

4.2 Coating the stagnation surfaces using sol-gel method

Sol-gel processing is now accepted as a technology for forming thin films and coating. It is a wet chemical deposition process. Also, sol-gel process is the name given to any of a number of processes involving a solution, or sol, that undergoes a sol-gel transition [86]. A solution is truly a single-phase liquid, while a sol is a stable suspension of colloidal particles. At the transition, the sol becomes a macroscopic material (gel), which is interpenetrated by a liquid. In the deposition process, once the liquid evaporates, a thin layer of the coated material remains. The un-doped aluminum oxide is stable at high temperatures and chemically rather inert, which makes it suitable to be used. Sol gel processing has the following distinctive advantages in comparison with other deposition methods: 1) since liquid precursors are used, it's possible to coat complex shapes, 2) precise doping is easily achieved and 3) Simple operative procedure (no complex reactor system). Nevertheless, the sol-gel method still has some limitations. Solvents, such as alcohol and water, are involved in the process, so it's not appropriate for fabrication of substrates, which are very sensitive to solvents. Additionally, stress-induced cracks appear after pre-heat treatment and remain even after densification. Still, the sol-gel method is a very simple and flexible method for fabrication of thin films that possess properties (precise dopant concentration) not attainable by other methods. Therefore, this method was used in our current work.

In this present study, as mentioned earlier, the ceramic flat plates and the ceramic cylinder, which act as a stagnation surface, were coated on both sides with a well-established phosphor, chromium-doped aluminum oxide Al_2O_3:Cr (ruby) (chromium concentration = 1.1%). The sol-gel dip coating technique was used to prepare Cr^{+3} doped Al_2O_3 films. The preparation relies on a method of Bahlawane [87], which was developed for the depositing of pure α-Al_2O_3 as an oxidation-resistant coating of graphite.

The method is based on the use of aluminum tri-isopropoxide (ATI) as the aluminum source, diethylene glycol monoethylether (C6 H_{24} O_3) as the solvent, and acetic acid (CH_3 COOH) as the catalyst. In the present case, a small amount of chromium acetyl-acetonate ($Cr(acac)_3$ was added as a chromium source. For preparation of the sol, 937,157 mg aluminum tri-isopropoxide (ATI) was dissolved in 25 ml of diethylene glycol monoethylether (C_6 H_{24} O_3), and then 791,175 µl of acetic acid (CH_3 COOH) were added to the solution. The concentration of Cr^{+3} in Al_2O_3 was obtained by the relation ($X_{Cr(acac)3}$) / X_{ATI}), where X is the molar ratio. In our case, the chromium concentration was 1.1%, because the highest intensity of phosphorescence is at this ratio [88]. Figure 4.10 shows a flowchart of the procedure that was used for synthesizing the chromium-doped Al_2O_3 film using the dip coating technique. Before starting the coating process, the substrates surfaces were roughened about 1 µm using sand blasting, in order to ensure sufficiently good adhesion of the coating to the substrate. After that, substrates were fully cleaned in ethanol by an ultrasonic bath for 10 minutes, and subsequently weighted before and after deposition with high-precision balance.

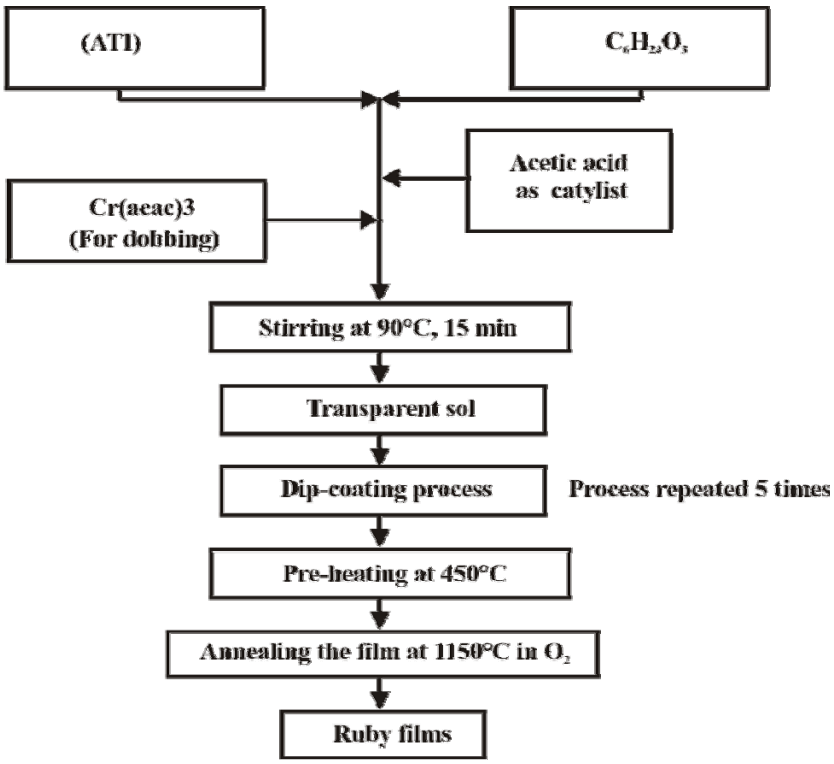

Figure 4.10: Flowchart showing the sol-gel procedure for preparing the chromium doped Al_2O_3 film

The substrates were coated using a dip coating method, as shown in Figure 4.10. In additional, Figure 4.11 shows in details the photographs of the preparation sequences of the dip-coating technique.

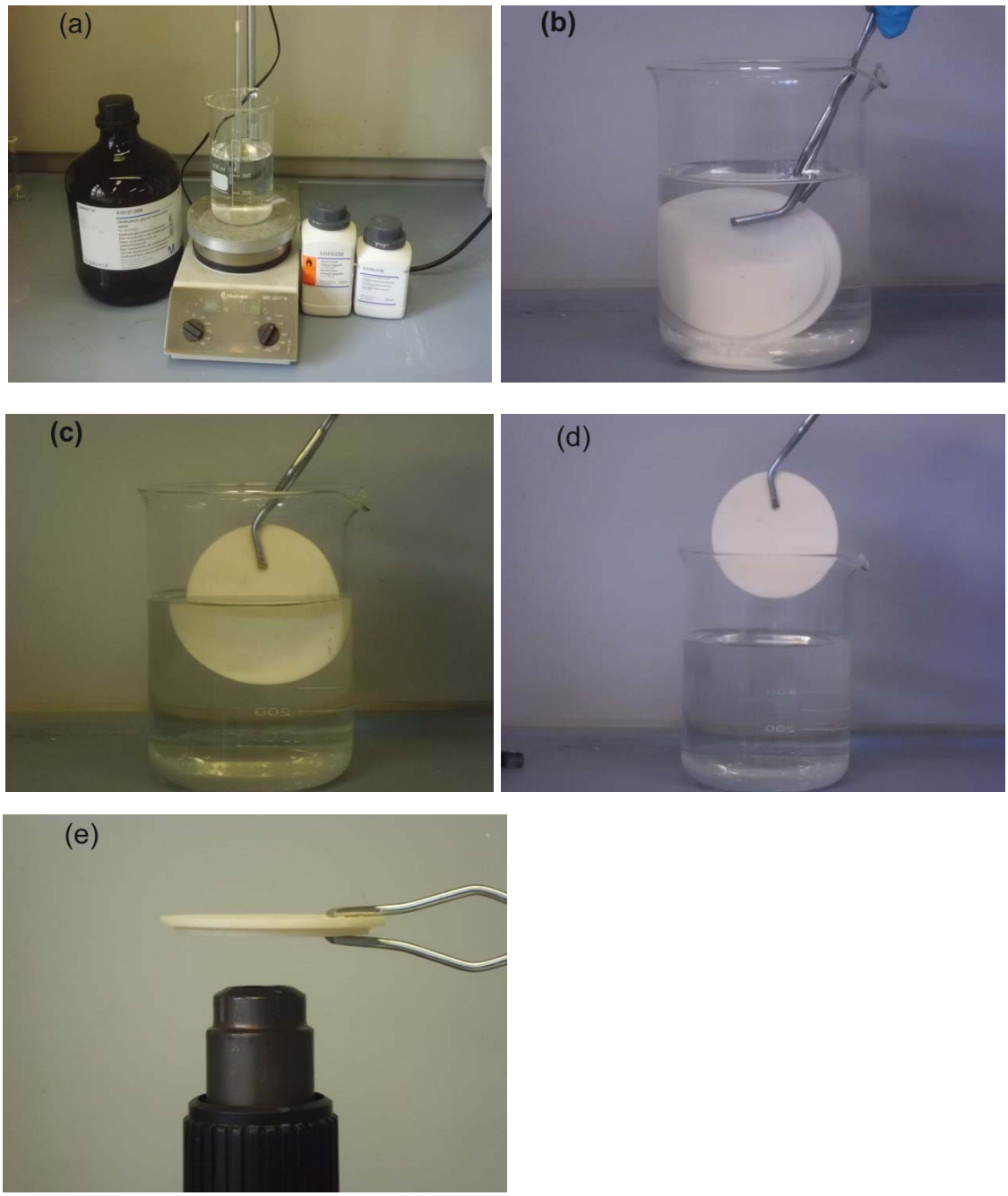

Figure 4.11: Dip coating technique (a) Sol-preparation; (b)-(d) Dip- coating process; (e) Drying the coating substrate

In this method, the substrates were just wetted with a liquid sol at room temperature, subsequently annealed in air at 563 K while forming an amorphous aluminium oxide film, and then finally annealed in a tube furnace (Carbolite) at 1403 K for two hours in order to obtain the stable α-phase of aluminum oxide. The thickness of film coating was of around 6 μm; the thickness was calculated from the changes in the mass samples during sol-gel deposition (~9.2 mg), the area of the deposition (~38.46cm^2) and the density of α-Al_2O_3 (3.99g/cm^2).

The structure of the coated ceramic plate was analyzed using X-ray diffraction (XRD). Figure 4.12 shows the patterns for the coated plate, which indicated that the α-phase of alumina (α-Al_2O_3) was the dominant crystalline phase, which is important to obtain reproducible phosphorescence.

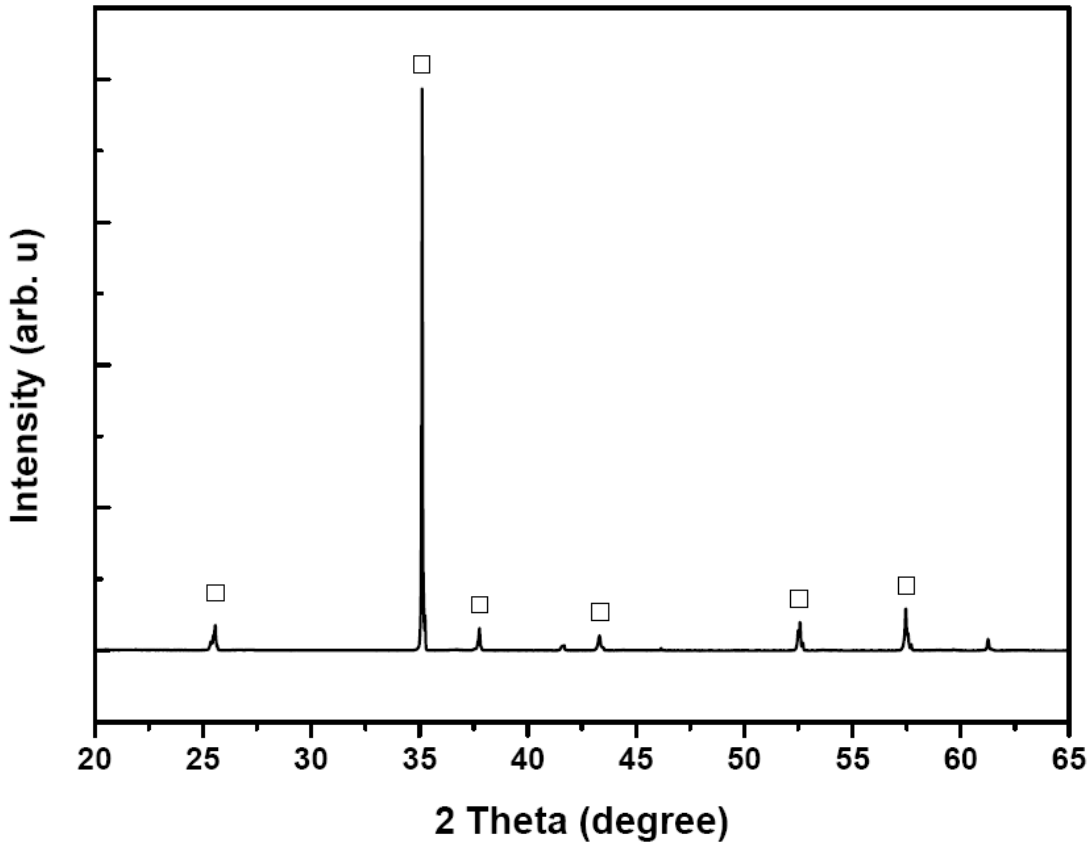

Figure 4.12: XRD patterns Cr^{+3}-doped aluminium oxide film on Al_2O_3 plate; α-Al_2O_3 reflection (□)

4.3 Calibration of thermographic phosphors

Several phosphorescence parameters are temperature dependent and are therefore in principle suited for the evaluation of surface temperatures: the phosphorescence lifetime, the total intensity, and the wavelength of the R-lines. Nevertheless, the latter is only slightly temperature dependent; e.g. a line shift of 0.685 nm is observed between 193 K and 293 K [89]. Phosphorescence lifetimes are most often evaluated for temperature measurements, since the excitation intensity for many phosphors play a minor role as long as the damage threshold is not exceeded [90]. Lifetime measurements are most often applied in the literature. Lifetimes are in the range from millisecond to below microseconds, so that data acquisition is relatively simple with standard laboratory equipment. Therefore, in this work, the film temperature was evaluated from the phosphorescence lifetime.

For calibration, the substrates — which are ceramic plates and a ceramic tube — were placed inside a tube furnace (Carbolite), where they were stepwise heated until the stationary temperatures were reached. The surface temperatures of the substrates were measured using a thermocouple in direct contact with the surface, while the phosphorescence from the measured area at the surface was detected. Figures 4.13 and 4.14 show the schematic and photograph for the calibration setup, respectively. The phosphorescence was excited with a green light-emitting diode (LED) with a peak wavelength at 525 nm (±45nm) in the range of 295-580 K, emitting maximum power of 2.4 W. The rise and the decay time of the edges of the LED is on the order of 10ns. This time is considerably shorter than the expected and measured lifetime. Subsequently, the phosphorescent signal was collected using two biconvex lenses and focused onto a photomultiplier (PM). The unwanted radiations, such as reflected LED, were blocked using a bandpass filter placed in front of the entrance of the photomultiplier.

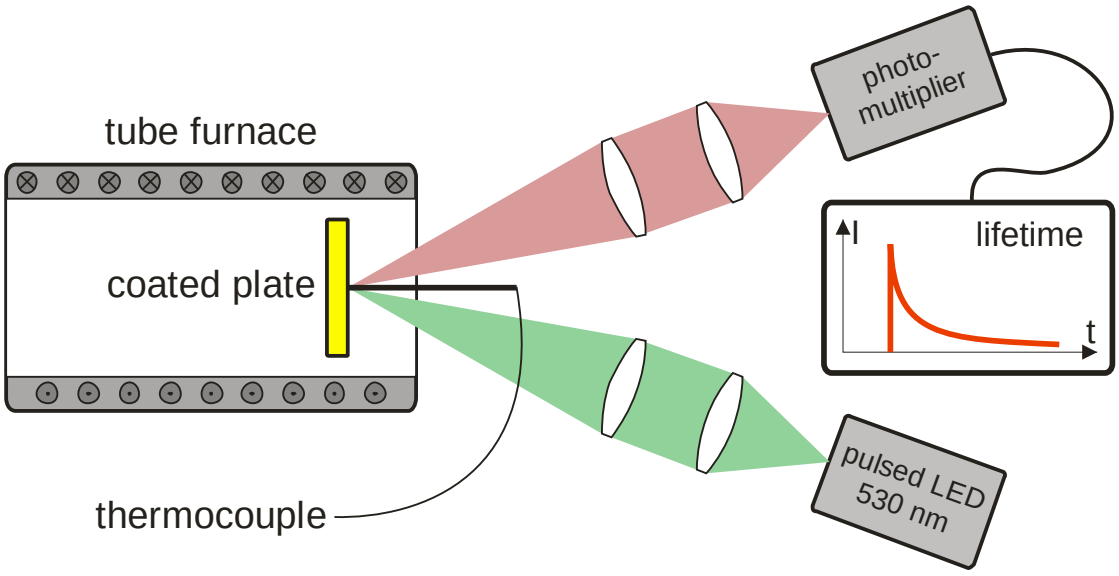

Figure 4.13: Schematic of the calibration set-up

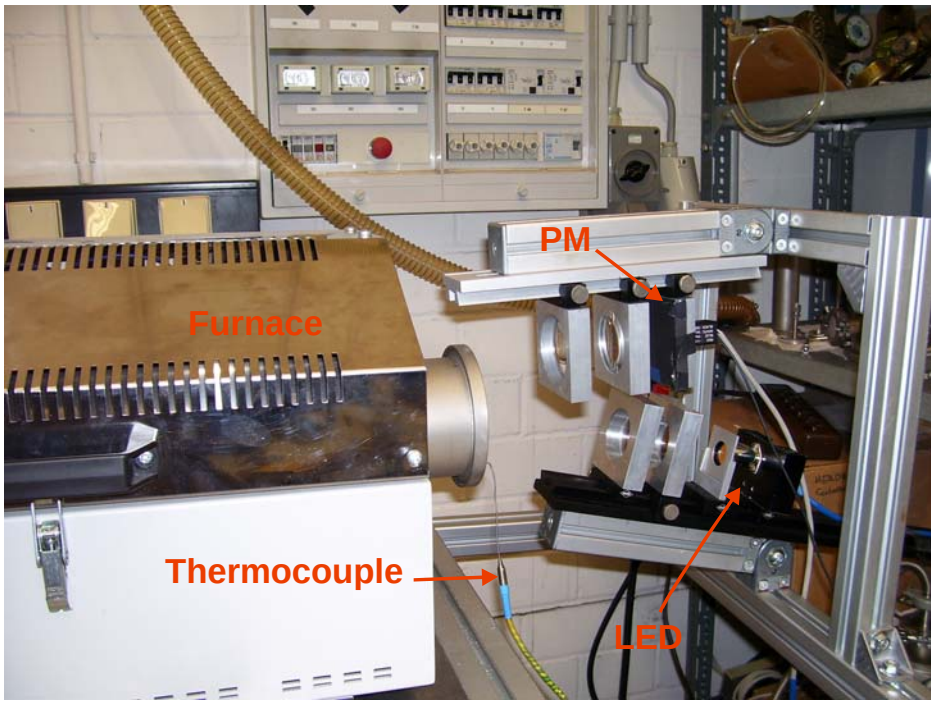

Figure 4.14: Photograph of the calibration setup

For each measurement, the emission signal of the phosphorescence was recorded and the decay time was evaluated. The temperature-dependence of the phosphorescence lifetime was determined for both sides of the ceramic plate. In the case of the ceramic cylinder, it was determined only for the outer surface. Figure 4.15 shows the calibration curve on which the phosphorescence lifetime was measured as a function of temperature ranging from 3450 μs at 293 K to 210 μs at 580 K.

In order to validate the calibration data, they were fitted to Seat-Sharp Model [91], which shows a good agreement. This model is relatively accurate for ruby lifetime decay from 300 to 800 K. With proper choice of fit parameters this model can give a very accurate prediction of temperature-dependent fluorescence lifetime. The obtained fitted parameters were later used to determine the surface temperature on both sides of the plate.

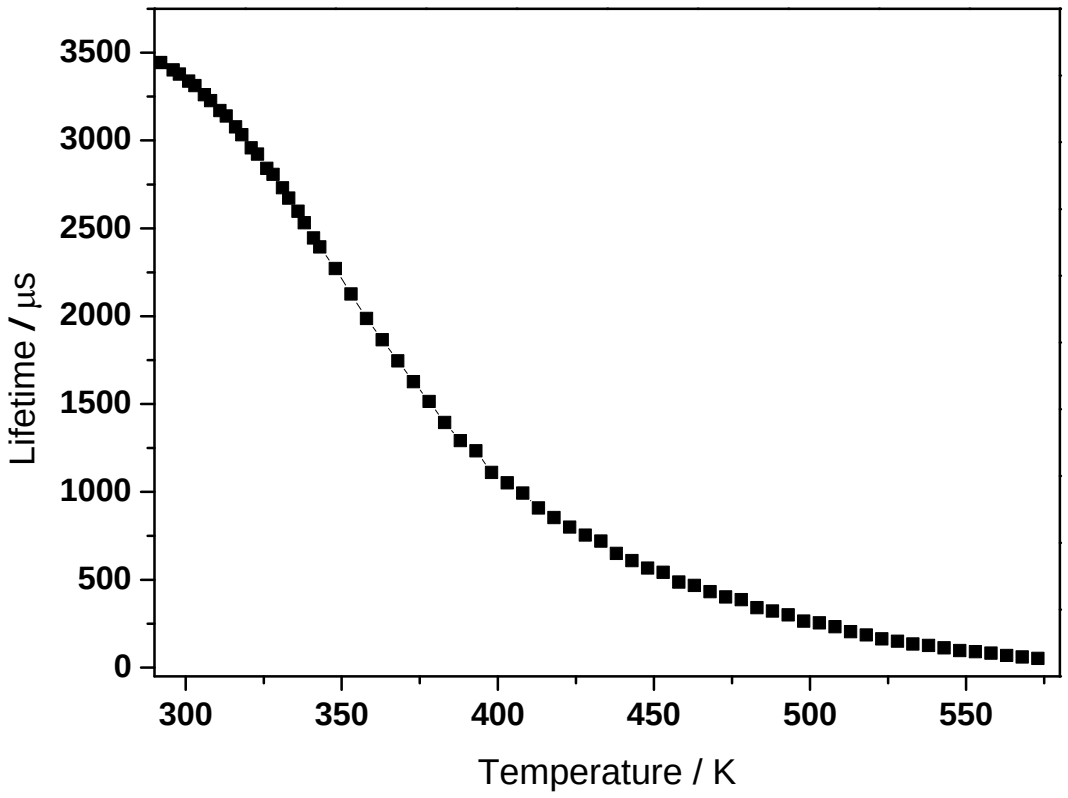

Figure 4.15: Lifetime decay of Cr:Al_2O_3 at different temperatures

4.4 Experimental procedure

In order to achieve the temperature uniformity in the impingement wall, the flow of cooling water was started 20 min before the fuel gas was ignited. The temperature and flow rate of the cooling water set to ensure the impingement surface temperature was higher than the dew point of the combustion products to avoid condensation. Before ignition of the gas mixture, the lifetime of the phosphorescence from both sides of the plates was measured in order to verify that the lifetime at cooling water temperature matches the calibration curve. After that, the premixed fresh gases, i.e. ethanol, hydrogen and air, enter the burner and are ignited. Once the flame was ignited, the steady-state operation conditions could be reached in several minutes, that is, when the temperature of the outlet cooling water became constant. It is very important for the measurements to be conducted after the steady-state conditions are established. Hence, all the lifetime measurements for the burning flame were measured under steady state conditions. The phosphorescence signal from both sides was recorded simultaneously; three individual tests were conducted at the same operation condition. The average of these tests was taken for further evaluation. This permitted a check on repeatability and improved accuracy.

As stated earlier, two different types of burners were used. A flat burner was used for low cold gas velocities of 0.1 m/s to 0.5 m/s (in steps of 0.1 m/s). In this range, the free flame velocity for stoichiometric flame is higher than the cold gas velocity, which leading to a burner stabilized flame. Once the cold gas velocities exceed 5 m/s, the flames show cellular structure on the burner. Hence, to avoid this problem, the nozzle burner was used at higher velocities of 0.6 m/s to 0.9 m/s (in steps of 0.1 m/s). Also, two different configurations of the impinging surface were used, i.e. flat plate and cylinder. In this experimental work, the most basic measurement required is the surface temperature on the both sides of the impinging plate. Measuring the surface temperature is very important, as it is needed for the calculation of the heat flux. Thus, in this case, the accuracy of temperature measurement is very important.

Experiments were designed to investigate the influence of some major parameters on the heat transfer characteristics of the impinging ethanol/air flame. These major

parameters are: cold gas velocities, the equivalence ratio, plate-to-burner distance and oxidizer composition. The range of cold gas velocities varied from 0.1 m/s to 0.9 m/s. The different equivalence ratios were stoichiometric (φ =1), lean (φ = 0.75) and rich (φ = 1.25), at the smallest burner-to-plate distance (H=15 mm). The burner-to-plate distances, namely H = 30 mm and H = 60 mm, are for stoichiometric flame. Moreover, ethanol-oxygen enhanced air flames were investigated, to measure the influences of the oxidizer composition. The oxygen concentration in oxidizer composition ranged from 21% to 40% by volume. In addition, hydrogen-enriched ethanol/air flames, which impinge on the flat plate, were investigated to find the effect of hydrogen addition on the heat flux of the impinging flame. The values of hydrogen content in the mixture, with respect to the ethanol, varied from 10% mol to 75 % mol. For hydrogen/ethanol/air flames, the experiments were performed at two different equivalence ratios: stoichiometric (φ =1) and lean (φ = 0.75). Additional experiments were also carried out to verify the effect of inclination on the heat flux between a flat plate and an impinging ethanol/air flame. The inclination angles chosen for investigation were 45°, 75° and 90°. For flames impinging normally on a cylindrical surface, also, the experiments were performed to verify the effect of some operation condition, such as cold gas velocity, burner-to-surface distance and equivalence ration, on the heat flux of the impinging flame. Moreover, these experimental results were compared with results obtained from the flame impinging normally on a flat plate, at the same operation condition.

4.5 Life time decay analysis and heat flux calculation

As mentioned before, this study's objective was to measure the surface temperatures, required to derive the heat flux at the stagnation point. For this purpose, a thermographic phosphor method was used. The main principle of this technique is based on the exciting the thermographic phosphor on the target surface with a pluse light and then measuring the phosphorescence lifetime decay of the emitting signal. The lifetime strongly depends on the temperature; thus, the temperatures can be extracted from the time-dependent phosphorescence intensity.

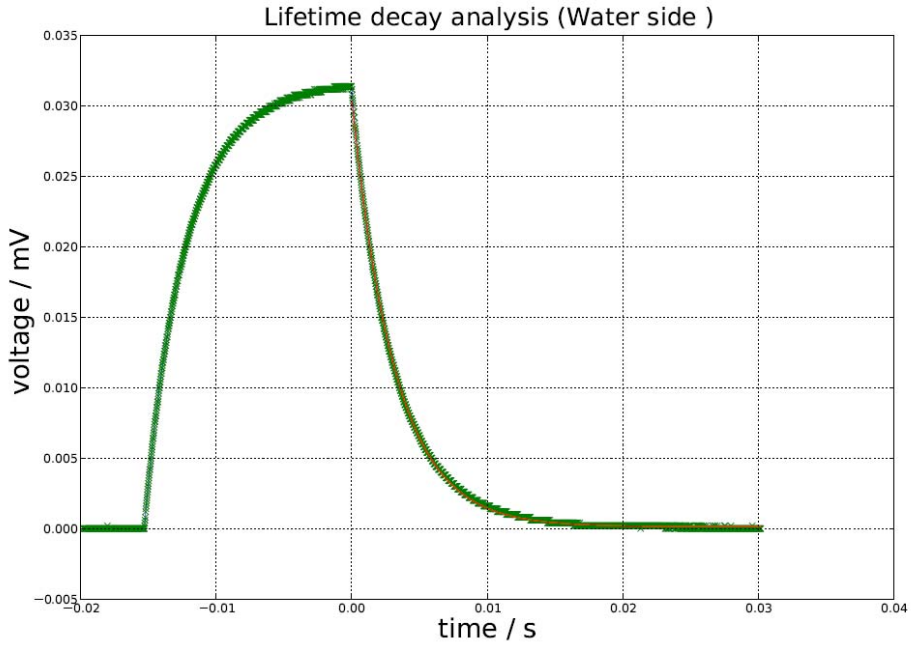

Figure 4.16: Lifetime analysis for the zirconium oxide plate, cooled side (green: fit, red: measured)

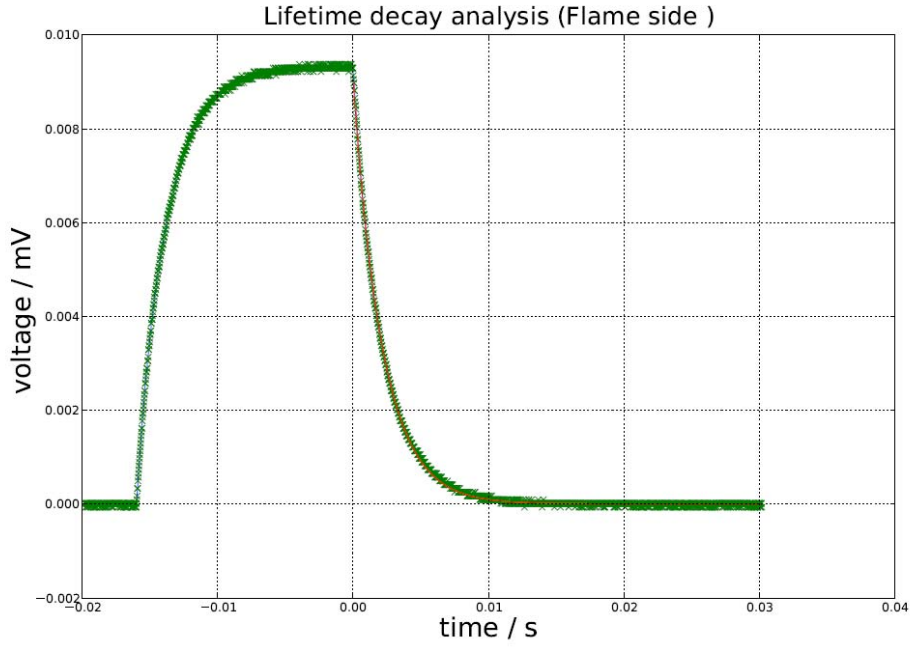

Figure 4.17: Lifetime analysis for the zirconium oxide plate, flame side (green: fit, red: measured)

A more frequently used approach to the decay analysis in phosphor thermometry is the fitting of a mono-exponential model to experimental decay transients, where the decay time (τ) can directly be attributed to a corresponding calibration temperature.

Thus, as mentioned in chapter 3, the lifetime (τ) can be deduced from the following expression:

$$I(t) = I_{\circ} \exp(-t/\tau) \tag{4.1}$$

Figures 4.16 and 4.17, for example, show typical phosphorescence signals on the cooled side (water side) and on the hot side (flame side) of the stagnation plate, leading to temperatures of 306.6 K and 362.65 K, respectively.

Heat flux at stagnation point was calculated based on the calculated temperature difference, using a one-dimensional heat conduction equation. The heat flux was calculated through two different configurations, i.e. ceramic plate and ceramic cylindrical , were calculated.

As mentioned in 3.2.2.2, the one-dimensional heat conduction equation for flat plate:

$$\dot{q} = \frac{Q}{A} = -\lambda \frac{\Delta T}{L}$$

And for cylindrical surface:

$$\dot{q} = \frac{Q}{A} = -\frac{\lambda \Delta T}{r \ln(r_2/r_1)}$$

4.6 Uncertainty analysis

In this section, the following subsections will include detailed estimation of error in this present work, including lifetime calibration data, surface temperature measured on both sides of the plate, and the heat flux.

4.6.1 Error estimation of the calibration data (lifetime decay)

As explained in section 4.3, the life time decay of the excited phosphor coating was calibrated, inside the tubular furnace, at different temperatures before it was used for surface temperature measurements. The procedure was repeated three times and then the errors were estimated. Figure 4.18 and table 4.1 show the lifetime relative errors, which are below 2.2%. This small value of the relative error demonstrates the excellent repetitions of the results.

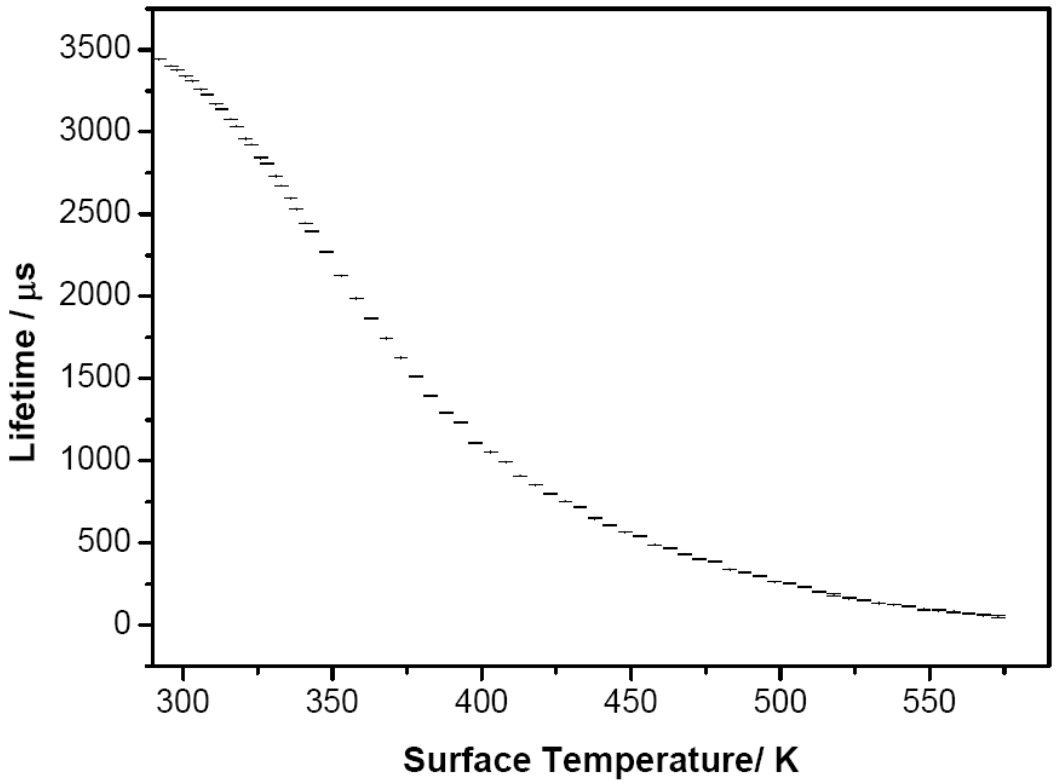

Figure 4.18: Life time decay of Cr^{+3}:Al_2O_3 at different temperatures

Table 4.1: Lifetime decay calibration errors of Cr^{+3}:Al_2O_3 (ruby) at different temperatures

Plate surface temperature (K)	Lifetime First Measurements (μs)	Lifetime second Measurements (μs)	Lifetime Third Measurements (μs)	Error (μs)	Relative Error %
298.15	3380.407	3378.37	3372.8	4.049	0.11
303.15	3310.262	3312.54	3318	9.03	0.27
308.15	3231	3226.5	3253	14.41	0.44
313.15	3130	3139	3179	26.13	0.82
318.15	3032	3035	3092	34.35	1.12
323.15	2921	2922	2978	32.82	1.11
328.15	2786	2807	2851	32.82	1.16
338.15	2516	2532	2546	14.66	0.57
348.15	2237	2271	2280	22.34	0.98
353.15	2114	2126	2108	9.306	0.43
358.15	2019	1986	1995	16.99	0.84
363.15	1886	1865	1850	18.15	0.97
368.15	1743	1745	1730	8.5	0.49
373.15	1601	1626	1590	18.59	1.15
378.15	1474	1514	1500	20.03	1.33
388.15	1307	1291	1280	14.03	1.08
393.15	1181	1234	1200	26.82	2.22
398.15	1131	1110	1120	10.78	0.96
403.15	1025	1051	1031	13.96	1.34
408.15	982	992	980	6.8027	0.69
413.15	917	908	905	6.502	0.71
418.15	846	853	840	6.79	0.8
423.15	789	799	793	4.806	0.6
433.15	691	719	700	14.2	2.01
438.15	627.4	649.7	633	11.62	1.82
443.15	601.2	608	600	4.78	0.79
448.15	562.8	566	569	3.06	1.08
453.15	536.49	541	544	3.84	0.71
458.15	498	486	493	5.98	1.21
463.15	451	467	463	8.14	1.76
468.15	415	432	425	8.306	1.95
473.15	381	395	388	6.935	1.78
483.15	338	340	339	1.02	0.3
488.15	314	321	318	3.54	1.11
493.15	299	302	295	3.955	1.32
498.15	261	263	265	1.622	0.61

4.6.2 Error estimation of the experimental measurements

In this subsection, the detailed estimation of heat flux errors for the two kinds of impingement surfaces, zirconia plate and alumina plate, are presented. As mentioned in section 3.2.2.2, the one dimensional heat flux through the flat plate is calculated using the formula:

$$\dot{q} = \frac{\dot{Q}}{A} = -\lambda \frac{\Delta T}{\Delta x}$$

where Δx is the thickness of the plate and ΔT the temperature difference between the two surfaces i.e. the flame side and the water side.

To calculate the heat flux error, it is necessary to calculate the errors in temperature difference (ΔT), thermal conductivity λ, and plate thickness (Δx). Hence, According to the root-sum-square method (Kline and McClintok) [92] the error in the heat flux is given by:

$$\delta \dot{q} = q \sqrt{\left(\frac{\delta \Delta T}{\Delta T}\right)^2 + \left(\frac{\delta \lambda}{\lambda}\right)^2} \qquad (4.2)$$

4.6.2.1 Thermal Conductivity (λ) error estimation

Thermal conductivity of alumina is strongly dependent on the temperature. It turns out that the published absolute thermal conductivities of alumina were obtained from three different techniques; namely, calorimetry, hot-wire, and Laser-flash [93]. The thermal conductivity values, which were used to calculate the heat fluxes in the current study, were obtained using Laser flash thermal technique. The Laser-flash technique yielded average calculated thermal conductivity values ranging from 22.2W/mK at 298 K to 10 W/mK at 673 K. In calculating the values of the thermal conductivity integrals presented in this study, a linear interpolation was assumed between these temperatures (298K – 673K). Thus, the interpolating equation for thermal conductivity λ of alumina has the form

$$\lambda = 22.2 - 0.0325\left(T - 298\right) \tag{4.3}$$

In this current study, the averages of the thermal conductivity of both sides of the plate were taken for heat flux calculation.

$$\lambda_{average} = \frac{\left(\lambda_{flameside} + \lambda_{waterside}\right)}{2} \tag{4.4}$$

Hence, it was necessary to calculate the thermal conductivity errors. Table 4.2 shows the estimated relative errors of the alumina plate's thermal conductivity due to surface temperature variation. Their relative errors were relatively small, lower than 0.16%. The average values of thermal conductivity on the both sides of the used alumina plate were used.

For the zirconia plate, the thermal conductivity remains approximately constant, at 2.5 W/m·K, in the temperature range from 293K to 480K. Therefore, the error in the zirconia thermal conductivity was negligible.

Table 4.2: Thermal conductivity (λ) errors on both sides of the alumina plate

Gas cold velocity (m/s)	Average λ1 (W/m.K)	Average λ2 (W/m.K)	Average λ3 (W/m.K)	Average λ (W/m.K)	Error (W/m.K)	Relative Error %
0.1	21.7	21.7	21.7	21.7	0.015	0.07
0.2	21.2	21.2	21.2	21.2	0.014	0.06
0.3	20.6	20.6	20.7	20.6	0.034	0.16
0.4	20.1	20.1	20.1	20.1	0.01	0.05
0.5	19.7	19.8	19.8	19.8	0.014	0.07

4.6.2.2 Temperature error estimation

The errors in the measured plate surface temperatures were estimated. Figure 4.19 shows the relative errors for surface temperature measurement on both sides of the alumina plate and zirconia plate. There are some possible sources for these errors, such as very small changes in the cooling water flow rate. Additionally, changes in the flame structure are difficult to control. As seen here, the errors are relatively small. However, these types of errors will increase the total errors in the heat flux, especially for the materials with relatively high thermal conductivity (such as alumina).

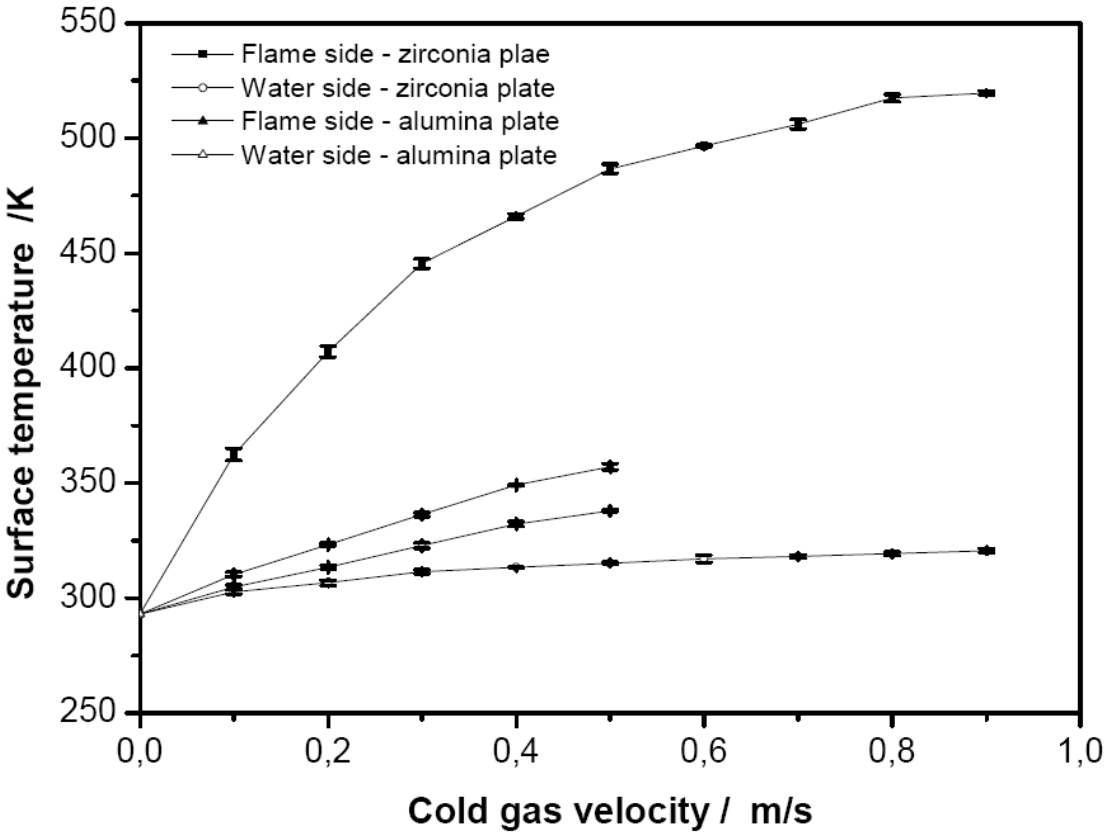

Figure 4.19: Surface temperature measurement on both sides of the alumina plate and zirconia plate (at ϕ = 1.0 and H =15mm)

4.6.2.3 Temperature difference (ΔT) error estimation

Temperature difference error (δΔT) is one of the most significant factors that affect the heat flux error estimation. Therefore:

$$\Delta T = T(FS)_{average} - T(WS)_{average} \tag{4.5}$$

and,

$$\delta\Delta T = \sqrt{(\delta T(FS))^2 + (\delta T(FW))^2} \tag{4.6}$$

Where, FS and WS are the heated side (flame side) and cooled side (water side) of the plate respectively. Tables 4.3 and 4.4 show the surface temperature difference (δTΔ) errors for the alumina and zirconia plate, respectively.

Table 4.3: Surface temperature difference (δTΔ) errors for alumina plate

Cold gas velocity (m/s)	ΔT (K)	Error (K)	Relative error %
0.1	5.5	0.7	12.65
0.2	9.9	0.5	5.59
0.3	13.4	0.8	5.69
0.4	16.9	0.5	3.09
0.5	19.1	0.7	3.81

Table 4.4: Surface temperature difference (δTΔ) errors for zirconia plate

Cold gas velocity (m/s)	ΔT (K)	Error (K)	Relative error %
0.1	59.7	1.3	2.3
0.2	100.5	1.3	1.3
0.3	134.1	1.1	0.8
0.4	152.7	0.5	0.3
0.5	171.5	1.03	0.6
0.6	179.7	0.8	0.4
0.7	188.0	1.1	0.6
0.8	198.2	0.9	0.4
0.9	199.1	0.6	0.3

It was clear that the relative errors for temperature difference are less than 12% for the alumina plate, and less than 2% for the zirconia plate. This is because the thermal conductivity of the plate material is inversely proportional with the temperature gradient through the plate.

4.6.2.4 Heat flux error (δΔq) estimation

Based on the estimated errors for the temperature difference and thermal conductivity, the heat flux errors were calculated using the root square method, as noted in section 4.6. Figure 4.20 shows the stagnation point heat flux errors for the zirconia plate and alumina plate. It is clear that the heat flux is relatively higher in the alumina plate, at less than 13%. It is less than 2% in the zirconia plate. This may stem from the values of temperature difference between both sides of the plate and also from the value of thermal conductivity.

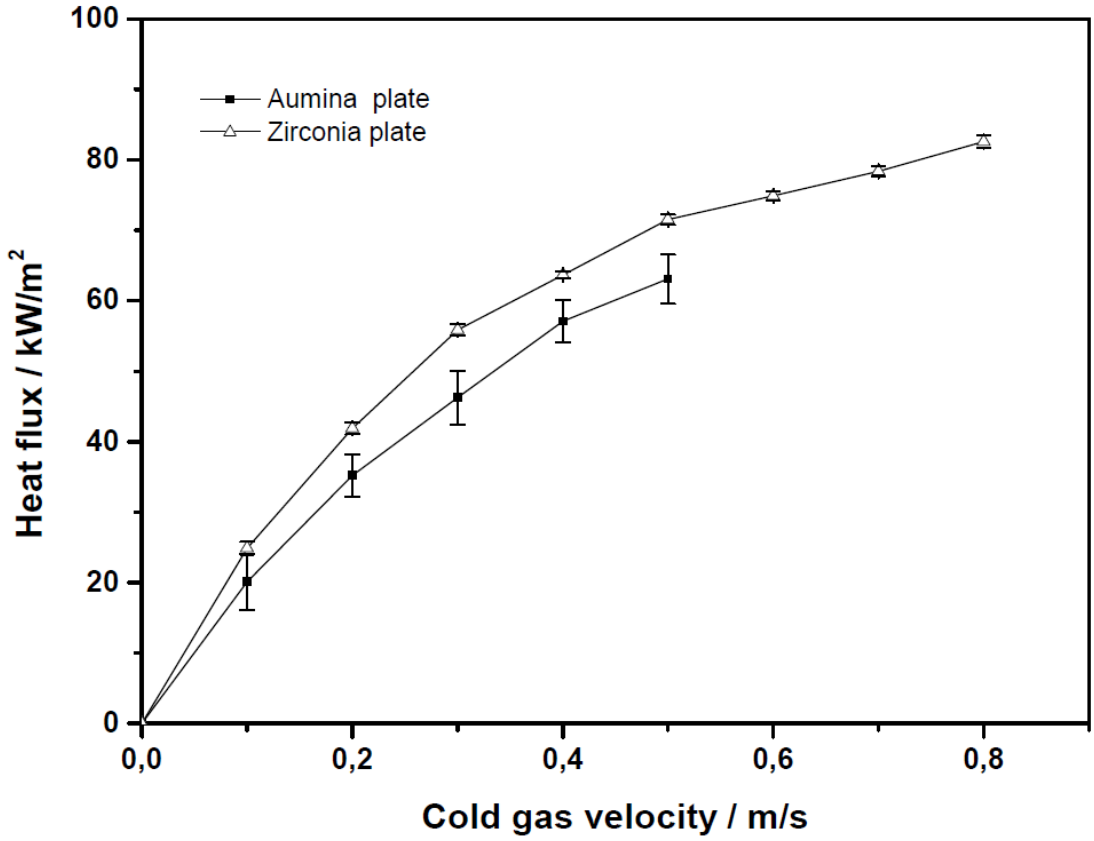

Figure 4.20: Stagnation point heat flux for stoichiometric ethanol flame (ϕ=1.0 and H=15mm)

4.7 Modeling

The stagnation point flames were modeled as one-dimensional flows with detailed chemistry and transport processes by B. Atakan [contact] using the premixed stagnation flame code in the Cantera reacting flow software [94], where the similarity solution for the flow is implemented. The mechanism used was GRI-Mech 3.0 (GRI), which is a detailed kinetic model including 325 reactions of 53 species .The program solves the one-dimensional balances for momentum, energy and species. Regarding the transport coefficients, two models were implemented in Cantera: a mixture-averaged model and a multispecies model. Calculations were

performed using both, leading to similar results. The simpler mixture-averaged model results are presented here.

The temperatures at the stagnation plate and at the burner surface were supplied as boundary conditions, whereas no surface reactions were included. Because it was found that the changes in temperatures at the boundaries within 20-40K did not affect the results strongly. Thus, the burner surface temperature at z=0 was fixed to 338 K, in agreement with a thermocouple measurement. The calculations were repeated for many stagnation surface temperatures, but once more found that the calculated heat flux rates were only weakly influenced by the exact value.

To obtain the heat flux from the model, the convective heat flow to the surface had to be evaluated. Moreover, the temperature gradient at the impingement surface on the gas side had to be evaluated as well as the conductivity (k) of the resulting gas mixture adjacent to the stagnation surface. The no-slip boundary condition at the surface is directly applied. The conduction heat transfer mechanism is the remaining mechanism. Using Fourier's law for the gas phase:

$$\dot{q} = \lambda_{gas}\left[\frac{dT}{dz}\right]_{gas,z=Surface} \tag{4.7}$$

The gradient was evaluated from the temperatures of the final three grid points adjacent to the surface. The point next to the surface was fixed to a distance of 1μm, while the next points were typically at distances between 10 and 100μm, which ensured that flow velocities contributions to heat transfer at these positions were negligible. A polynomial was calculated from them, and the slope at the surface was taken from the first derivative at the location of the surface. No radiative heat flux is included in the energy balance of the flame model, thus the heat flux may be underestimated. Nevertheless, an estimation using the values from text books showed that the error should, at most, be in the area of a percentage of the total calculated heat flux.

4.7 Summary

The experimental set-ups used for measuring the flame impingement heat flux have been outlined. Also, the preparation and calibration procedures for thermographic phosphor coating are presented. Moreover, the experimental procedure and the method for measuring the flame impingement heat flux are explained. At the end of this chapter, the experimental uncertainty analysis and the modelling used are briefly explained. In the next chapter, the experimental results and detailed explanation of these results are presented accordingly.

5 Results and Discussion

This chapter presents the analysis and discussion of all the experimental results obtained in our present work. The experimental results mainly include study the effect of some operating conditions such as cold gas velocity, plate-to-burner distance, equivalence ratio, oxidizer and fuel on the heat flux of the flame jet system. In all experiments, laminar premixed flames were used. In this work, three different types of configuration were studies for impinging flame. Accordingly, this chapter is divided into three sections: (i) flame impinging normally on a flat plate, (ii) flame impinging on a flat plate at different angles, and (iii) flame impinging normally on a cylindrical surface.

5.1 Flame impinging normally on a flat plate

This type of configuration has been widely applied in many industrial processes. Hence, it has attracted much research, described in section 2.1.1. In this present work, flames impinging normally on a flat plate were investigated. Laminar premixed ethanol /air flames and hydrogen/ethanol/air flames were used in this study.

5.1.1 Laminar premixed ethanol/air flame

As one of the most promising clean alternative fuels, ethanol has already been used in many applications such as a fuel for internal combustion engines [95]. Therefore, the heat flux of a one-dimensional premixed ethanol/air flames impinging normally on a flat plate were measured, at the stagnation point. The effect of impingement surface thermal conductivity was examined. In addition, the influences of some key parameters were investigated; namely, flame stoichiometry, distance between burner and plate and oxidizer composition.

5.1.1.1 Influence of the impingement surface thermal conductivity

In order to validate and improve the accuracy of measurements, two flat plates of different materials were used separately as impingement surfaces; namely, alumina (λ=22.2 W/(m·K)) and yttria-stabilized zirconia (YSZ) (λ=2.5 W/(m·K)). For comparison purposes, both plates were used under the same operational conditions. Thus, the flames investigated were stoichiometric ethanol/air and the separation distance between the burner and plate was set at 15 mm.

Figure 5.1 shows the surface temperature measurement on both sides of the alumina plate and the zirconia plate as a function of feed gas velocity. As mentioned earlier, the flat burner was used for cold gas velocity below 0.5 m/s and the nozzle burner for higher cold gas velocity. There was no observable effect from replacing the flat burner with the nozzle burner regarding the slope of the surface temperature vs. cold gas velocity curve, as shown in Figure 5.1. As expected, the measurements indicate that the surface temperatures on both sides of the plates increased along with increasing the cold gas velocity. This occurred, because the increase of the cold gas velocity leads to the increase of flame temperature. However, in the case of the zirconia plate, as seen in Figure 5.1, it can be observed that the cold side's surface temperature is slightly influenced by increasing the cold gas velocity; this is due to the high convective nature of the cooling water. Furthermore, as velocity of the fresh gases increases, the temperature difference increases. In the case of the alumina plate, the temperature differences between both sides vary between 5.4 K and 21 K. In the case of the zirconia plate, temperature differences vary from 59.8 K to 199.7 K (except for the cold gas measurement with a mass flux of 0). As anticipated, it can be seen that the temperature difference between the heated side and the cold side is much higher for the zirconia plate. This is mainly because the zirconia material has relatively low thermal conductivity.

In order to reduce the uncertainty and prove the reproducibility of the measurements, they were repeated several times; the relative errors in the lifetime measurement were below 0.4% at temperatures below 520 K. The relative errors of the temperature difference can be determined with an absolute value better than ±2 K. For further

details about uncertainty estimation, see chapter 4. The relative error of the temperature difference is crucial for determining the accuracy of the calculated heat flux. Accordingly, it was found that the using the zirconia plate instead of the alumina plate improves the heat flux accuracy from 12.7% for the alumina plate to 2.3% for the ziroconia plate.

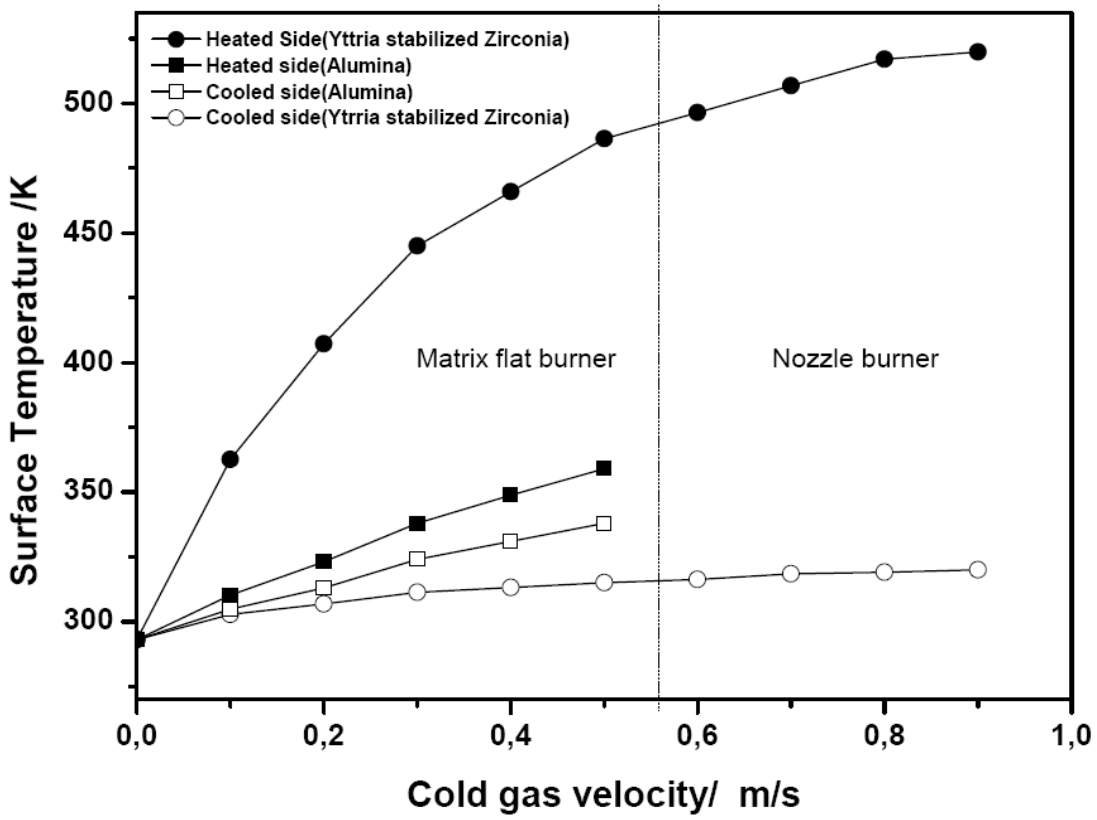

Figure 5.1: Surface temperature measured at H=15 mm for stoichiometric ethanol/air: Comparison of using alumina and zirconia as impingement surface

Based on the measured temperatures on both sides of the ceramic plates, the heat fluxes were calculated. Figure 5.2 shows the comparison between the modeling and the experimental heat flux calculated for a stoichiometric ethanol flame at a small distance between burner and plate (15 mm). It can be seen that the modeling and the experimental results have approximately the same trends. However, the results

obtained experimentally have values less than those obtained using modeling. On the other hand, the experimental results are in good agreement within their error limits. A possible reason for the discrepancy between the model and the measurements could be that the flame speed is not reproduced correctly by the model. Obviously, as mentioned above, the results obtained from the yttria-stabilized zirconia plate improve the experimental accuracy considerably. Hence, this material was used in all following investigations.

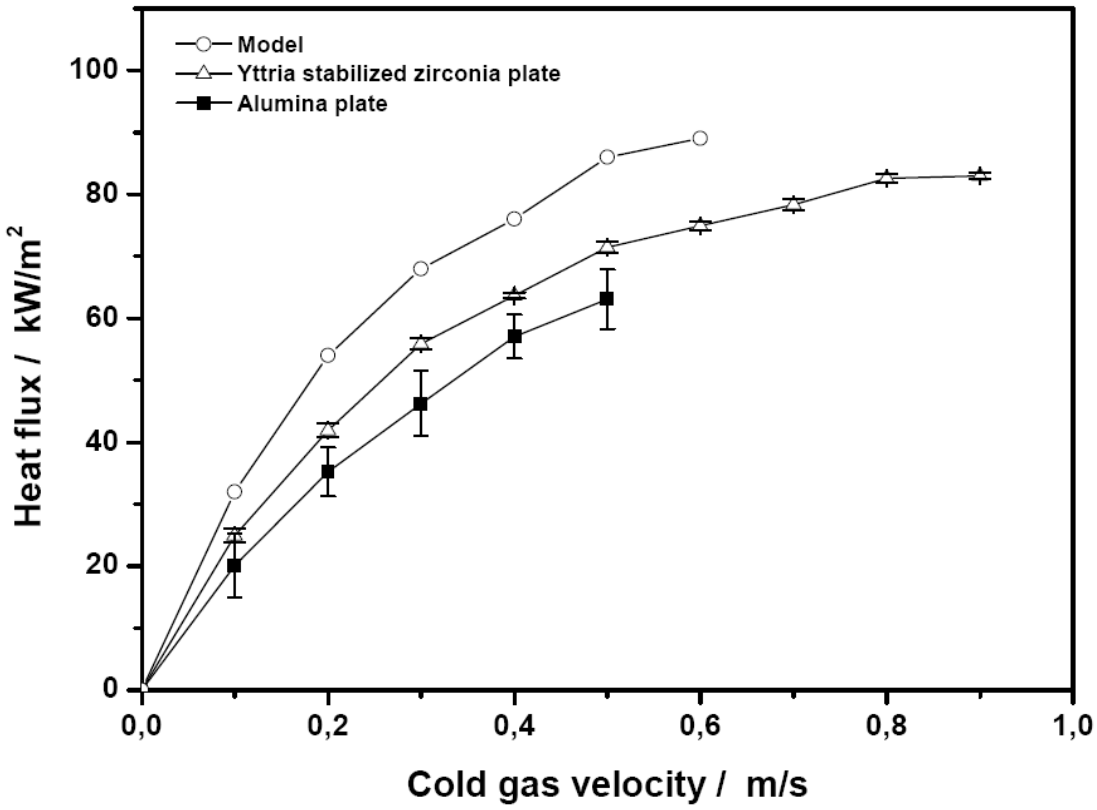

Figure 5.2: Stagnation point heat flux at (H=15mm) for stoichiometric ethanol/ air, comparison of experimental measurements (alumina and zirconia) and model

It is clearly seen that the heat flux from the flame to the plate increases with the velocity of the feed gas. Viscous effects are more dominant at lower feed gas velocity, so boundary layer thickness is reduced at the stagnation region as the feed gas velocity increases and consequently the heat flux is enhanced.

Furthermore, according to Kwok et al [96], length of luminous reaction zone would be increased by increasing the feed gas velocity; therefore the flame's hottest inner reaction zone would be closer to the impingement surface when plate-to-burner distance was kept constant.

5.1.1.2 Effect of equivalence ratio

The equivalence ratio is proven to have very important influence on the heat transfer characteristics of an impinging flame jet system, and many studies have been conducted to explore its thermal effects. For more details see section 2.2.2.

In this study, the heat fluxes from ethanol/air flames with three different stoichiometries on the impingement plate were investigated. Figure 5.3 shows the surface temperature measurement on both sides of the zirconai plate as a function of methane-air mixture velocities and with stoichiometries of 0.75, 1 and 1.2 at a distance of 15 mm. The highest flame temperature is expected for the stoichiometric flame (T_{ad} = 2598 K), because the fuel can be burned completely in contrast to the rich flame (T_{ad} = 2503 K for φ = 1.2), while there is no additional air to heat up and lower the reaction enthalpy as in the lean flame (T_{ad} = 2166 K for φ = 0.75). The measured surface temperature should reflect this tendency. As expected, it can be seen in Figure 5.3 that the surface temperature on the hot side is much lower for the lean flame than for the stoichiometric flame. Also, the surface temperatures for the rich flame were found to be very close to the stoichiometric flame. This tendency is also reflected in the heat fluxes, as shown below. On the cold side, the equivalence ratio slightly influence on the surface temperature, because the thermal resistance of the impingement surface is relatively high.

Chander [97] found that the rich methane/air flame temperature is relatively close to stoichiometic flame temperature. He surmised that since the flame was burning at ambient conditions, additional air may have led to lower real stoichiometries. However, in the given case, even if air entrainment plays some role, it is unlikely that air from the surrounding area can contribute considerably to the stoichiometry at the investigated small distance of 15 mm, considering the burner diameter of 30 mm.

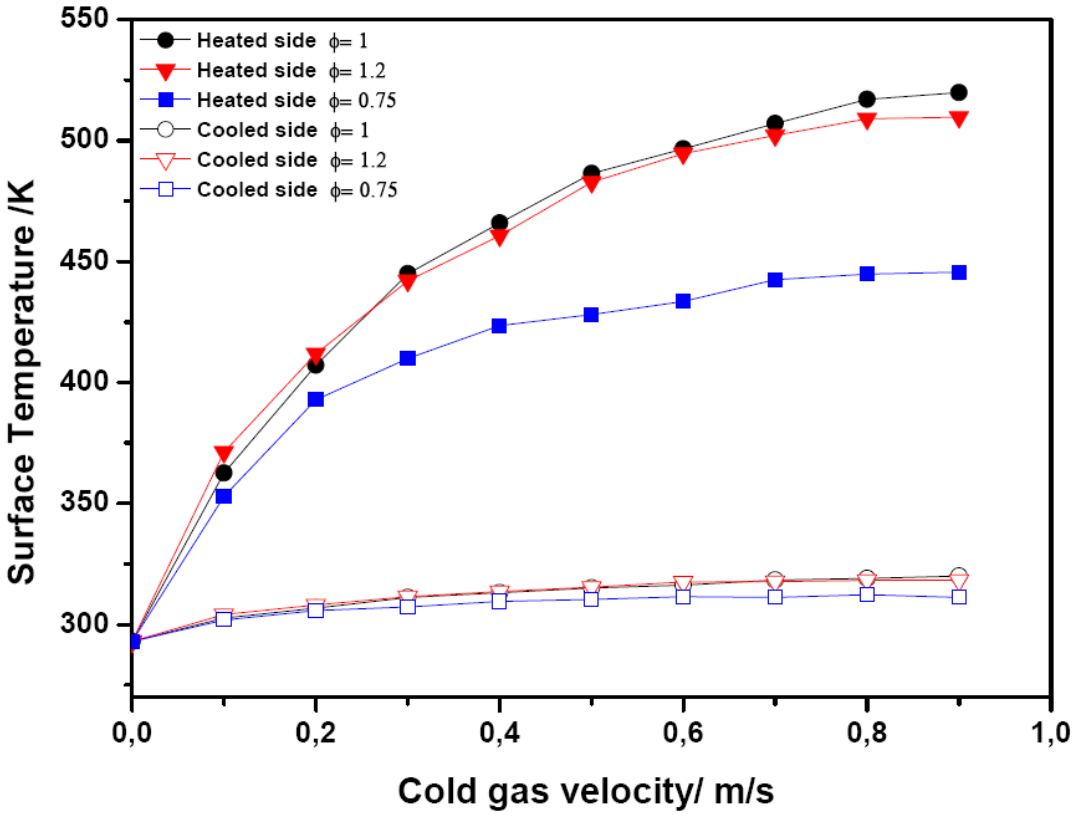

Figure 5.3: Surface temperature measurement at (H= 15 mm) for various equivalence ratios

Again, based on the measured temperatures on both sides of the plates, heat fluxes were calculated. Figure 5.4 shows the stagnation point heat fluxes at H= 15 mm for three stoichiometries. As mentioned above, the tendency temperature is also reflected on the heat flux. Therefore, seen in Figure 5.4, the difference between the stoichiometric and the rich flame is much smaller than the difference between the stoichiometric and the lean flame. However, for the low cold gas velocity, it can be seen that the difference in the heat flux between the three flames is relatively small in comparison with that at high cold gas velocity. For the low cold gas velocity, all three flames are burner-stabilized. The gradient for the stoichiometric flame is highest at the burner, leading to the highest heat loss for this flame. This in turn leads to similar maximum temperatures for the stoichiometric and rich flame, and reduces the difference

with lean flame, although the adiabatic flame temperature is higher for the stoichiometric one.

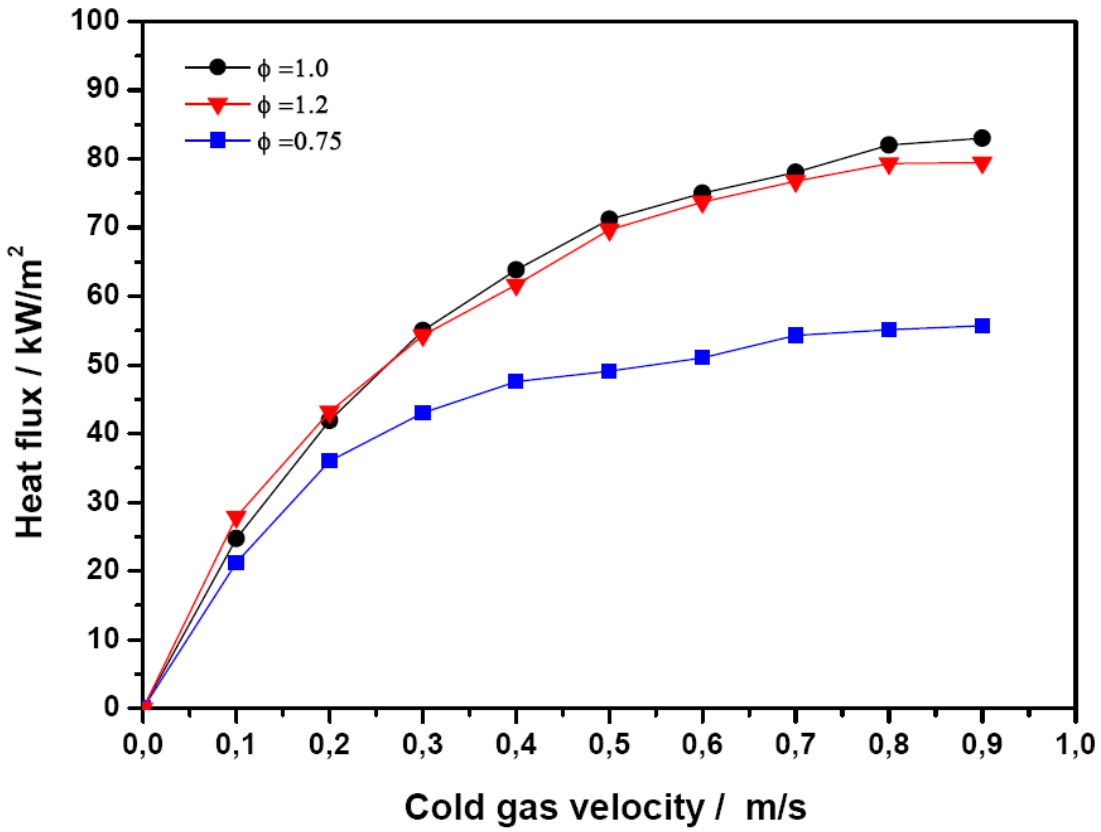

Figure 5.4: Stagnation point heat fluxes at (H= 15 mm) for various equivalence ratios

More importantly, the results indicate that the heat flux at the stagnation point increases by increasing the feed gas velocity. The larger supply of the air/fuel mixture provides more reactive gas species around the stagnation point, so that more heat is generated during the combustion process. One may also expect a linear relation between heat and feed gas velocity. But as seen in Figure 5.4, the slope becomes smaller when increasing the feed gas velocity. Specifically, the change in the slope is observed at cold gas velocity around 0.5 m/s for stoichiometric and rich flames. In a similar manner, it is observed at 0.3 m/s for lean flame. This change can be easily understood in terms of flame stabilization mechanisms. In other words, when the cold gas velocity is below the laminar burning velocity of 0.45 m/s for a

stoichiometric ethanol air flame [98, 99], the flame will be stabilized on the burner. In this regime, the heat transfer is strongly influenced by the mass flow rate; the reason for this is the large heat flux to the burner. Above this value, when the cold gas velocity is above the laminar burning velocity, the slope of heat flux with cold gas velocity is much lower; the velocity only slightly reduces the thickness of the boundary layer. This leads to a larger mass flux in the radial direction, but only weakly influences the heat transfer rate to the plate. It is likely this will change if flame quenching starts at even higher flow rates. The other possible reason is that the flame starts to detach from the burner and is stabilized on the stagnation plate; hence, the temperature gradient and the heat flux are only weakly influenced by the cold gas velocity.

Overall, these results show that intrinsic mechanisms of flame stabilization are most important for the heat flux from flames to walls. Generally, in most previous studies, convective heat transfer was discussed in terms of relationships between the Nusselt number and the Reynolds number. The first is a measure of the dimensionless temperature gradient at the surface, while the latter compares the inertia forces with the viscous forces. Accordingly, instead of using Reynold's number, the cold gas velocity relative to the free flame speed may be a more useful independent dimensionless parameter in the studies of heat transfer from flames.

For more explanation, it was necessary to study the effect of the equivalence ratio on the flame shape. Figure 5.5 shows the flame shapes, indicated from photographs taken by a digital camera. It is observed that a stable flame can be produced by increasing the equivalence ratio.

Comparing Figures 5.5 (a) and (b), the flame length is found to increase when burning a fuel-rich mixture. When the equivalence ratio increased, the flame become longer. Therefore, once the flame length is increased, the impingement causes more species to flow outward along the radial direction. In this case, more fuel will be consumed towards the wall-jet region, which results in more uniform distribution of heat flux on the impingement plate.

Comparing Figures 5.5 (b) and (c), as the gas-mixture velocity is increased, the flame is observed to become longer, which means that it becomes closer to the impingement surface and thus heat flux is enhanced. This is in agreement with the fact that heat transfer is enhanced by increasing the gas-mixture velocity.

Figure 5.5 (a) Flame shape
(V=0.3 m/s, ϕ=0.75)

Figure 5.5 (b) Flame shape
(V=0.3 m/s, ϕ=1.2)

Figure 5.5 (a) Flame shape
(V=0.4 m/s, ϕ=1.2)

5.1.1.3 Effect of burner-to-plate distance

The distance between the burner and the target plate is important from the perspective of heat transfer and flame stability, especially when the other operation conditions are fixed or cannot be altered easily. It is obvious that the separation distance will play a significant role for the design of heating equipment that makes use of direct flame jet impingement. Therefore, as mentioned in section 2.2.3, many studies have investigated the effect of plate-to-burner distance on the heat transfer. For the ethanol/air flame, the effect of this operational condition has not been tested yet, even though currently it is commonly used in domestic heating. In our case, stoichiometric ethanol/air flames were investigated at three burner-to-plate distances; namely H=15 mm, H=30 mm and H=60 mm. Figure 5.6 compares the measured temperatures for the three distances investigated experimentally.

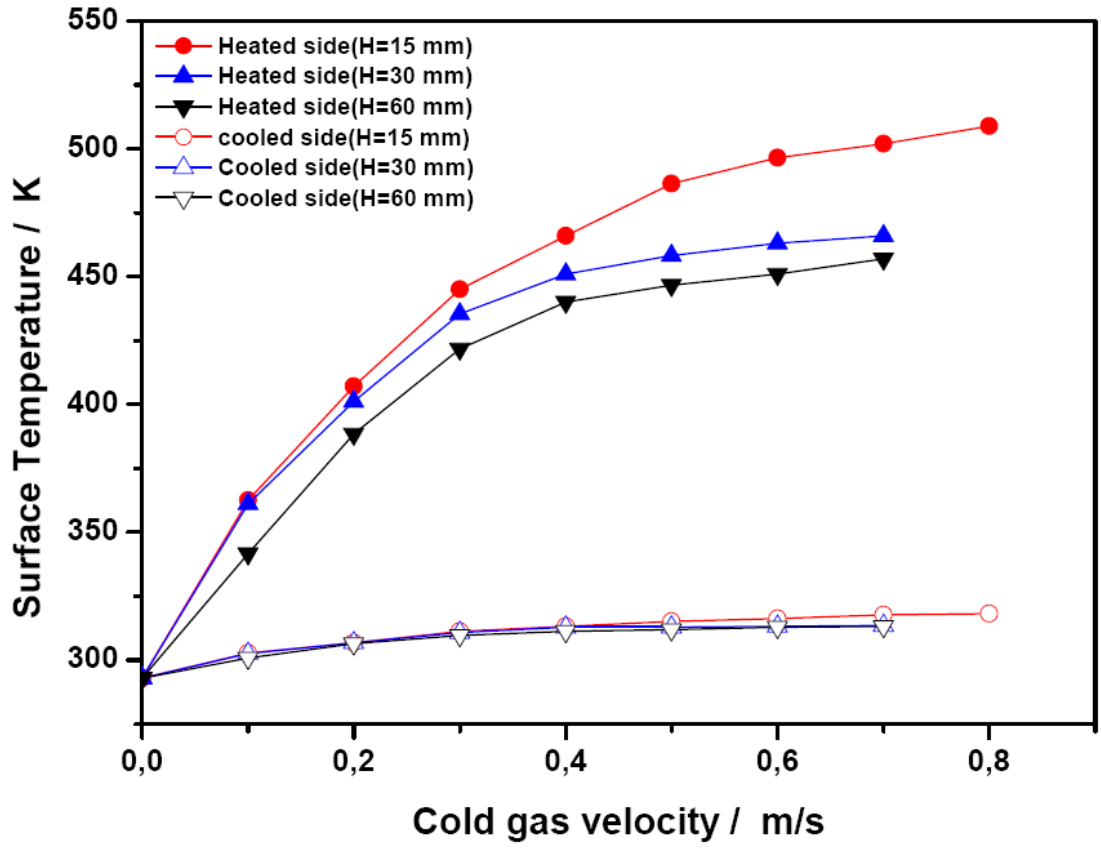

Figure 5.6: Surface temperature measurement for stoichiometric ethanol/air flames at various burner-to-plate distances

The temperatures on the hot side are highest for the small distance, with little difference between the temperatures on the water side. As previously noted, the main reason for that behaviour is the high convection coefficient on the water side. In other words, the thermal resistance on the water side is high because the inlet water temperature is relatively low (20°C). The water temperature remains nearly uninfluenced due to the high water flow rates; the wall temperatures also remain nearly constant on this side. For H= 15 mm, the temperature difference between the both sides vary between 59.8 K and 199.7 K. At H= 30 mm and H=60 mm, variation in the temperature differences are (58.8 K to 152.5 K) and (40 K to 143.7 K), respectively. These temperatures are used in the following for the heat flux evaluation

Figure 5.7 shows the experimental heat fluxes calculated for the stoichiometric ethanol/air flames at three different burner to plate distances. As can be shown the heat flux for the smallest distance is highest, while it is lower for the other two larger distances between the burner and the impingement plate. In the small separation distance around 15 mm, the high-temperature combustion gases impinge directly onto the plate surface to give the highest local heat flux at the stagnation point, as shown in Figure 5.7.

There are two potential reasons for this trend. First, the small value of separation distance may lead to high local heat flux concentration at a certain area, such as stagnation point, with less than optimal heating of the rest of the plate. Second, the small separation distance provided very high wall heat fluxes because of their close proximity to the plate and less heat loss to the atmosphere.

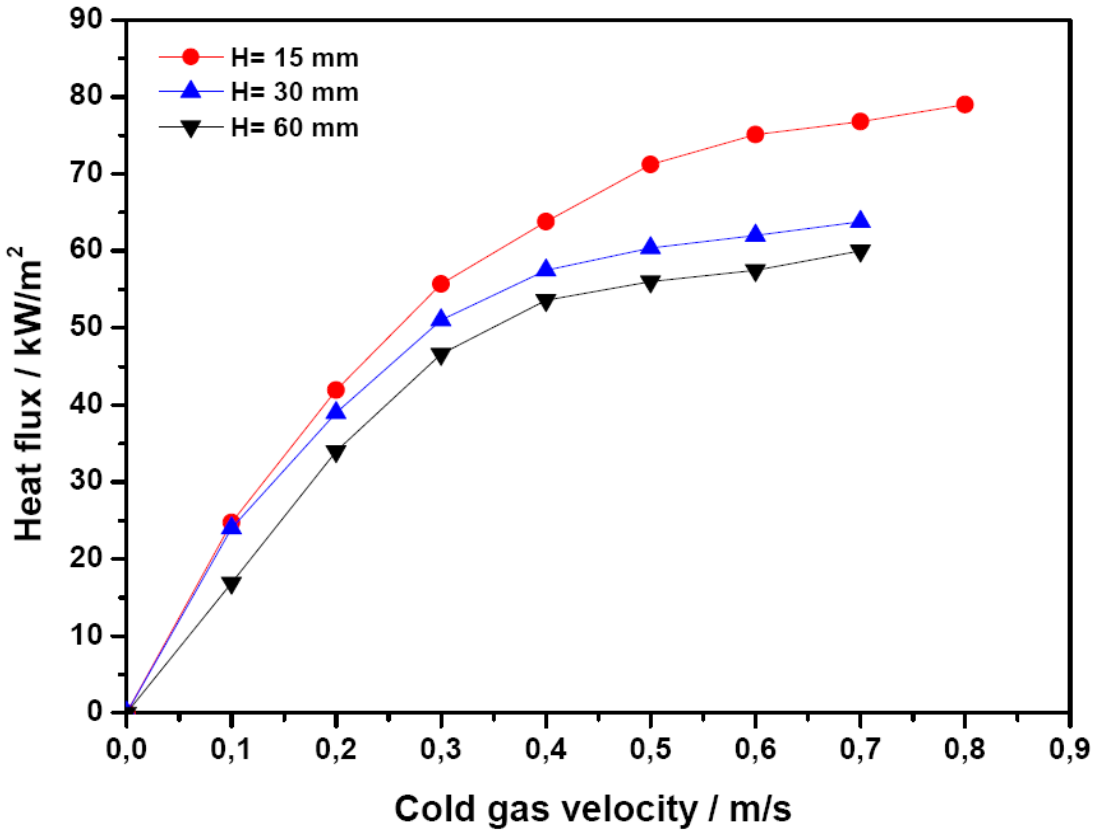

Figure 5.7: Stagnation point heat fluxes for stoichiometric ethanol/air flames at various burner-to-plate distances

Moreover, increasing the plate-to-burner distance will move the high-temperature outer layer of the flame away from the plate surface, which leads to a decline of heating performance. Dong et al. [36] found that the heat flux received by the impingement plate surface decreases when the distance between the potential core of the flame and the plate surface is excessively large.

5.1.1.4 Fuel type

In the gas-fired jet system, various gaseous fuels have been selected to produce the flame jet. Hydrocarbon fuel is most commonly used, which is oxidized by either air or pure oxygen [7]. Use of different gaseous fuels will certainly result with different thermal characteristics of the impinging flame jet system as well as its pollutant system.

In this present study, ethanol is selected as fuel. In order to investigate the effect of fuel type on the heat flux, Figure 5.8 compares the heat flux of the flames that produced by ethanol/air (current study) and methane/air [100]. All flames were investigated at the same operation conditions. The flames were stoichiometric and a plate-to-burner distance of 15 mm was set. The results of both flames are in good agreement within their error limits. Furthermore, the results show approximately the same behaviors. Therefore, it can accordingly be concluded that using methane or ethanol has no significant effect on the heat transfer of the flame. Chigier [30] suggested that there was no marked effect of fuel type on the convective heat transfer characteristics of the turbulent flame jet, but his experimental study was only conducted with heavy fuel oil and coke oven gas.

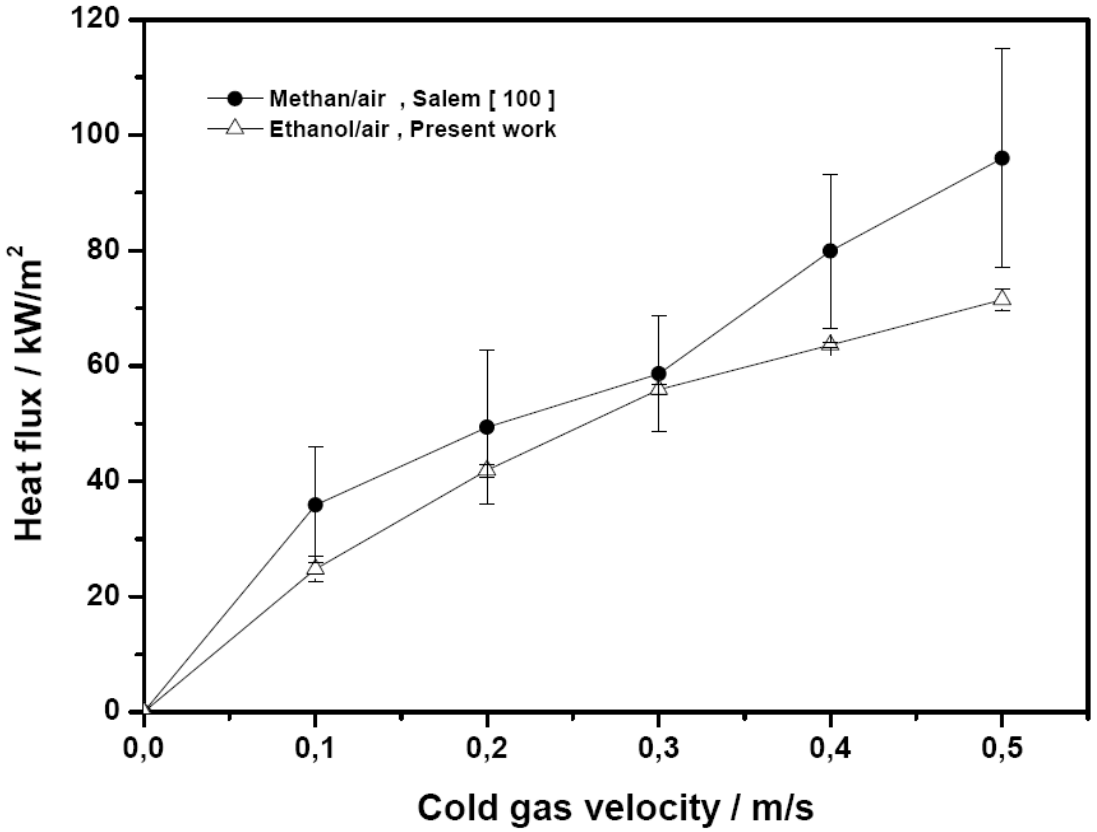

Figure 5.8: Comparison of the heat flux at the stagnation point from ethanol / air and methane/air flames

5.1.1.5 Oxidizer composition

The most important variable, after the physical configuration, is the oxidizer composition. The following subsection will present the effect of oxygen-enriched air and the effect of diluent addition.

5.1.1.5.1 Oxygen-enhanced air effects

A common way of specifying the oxidizer composition (Ω) is by calculating the O2 mole fraction in the oxidizer. It is well known that using an oxidizer with a higher concentration of oxygen than present in the air may enhance the combustion process. One result is an increase in the adiabatic equilibrium flame temperature [15]. Higher flame temperature lead to higher productivity in heating processes. Oxygen-enhanced combustion is now being used in some industrial technologies, such as rapid heating technology (RHT), which employs an oxygen/fuel impinging flame jet to the target surface [8]. Yet very few studies have used oxygen concentration levels between those of air and pure oxygen.

In this study, premixed oxygen-enriched air / ethanol flames were tested, with the oxidizer composition (Ω=0.21- 0.4). Figure 5.9 displays the surface temperatures as a function of cold gas velocity for a variable oxidizer composition (Ω). It is again shown that increasing the content in the oxidizer has significant influence on the heated side's surface temperature.

At higher values of Ω, the surface temperature increased. For example, at cold gas velocity 0.5 m/s, the surface temperatures on the hot side are 466 K at Ω=0.21, 486,34 K at Ω=0.3 and 504,19 K at Ω=0.4. In contrast, the cooled side surface temperatures are only slightly influenced by increasing Ω.

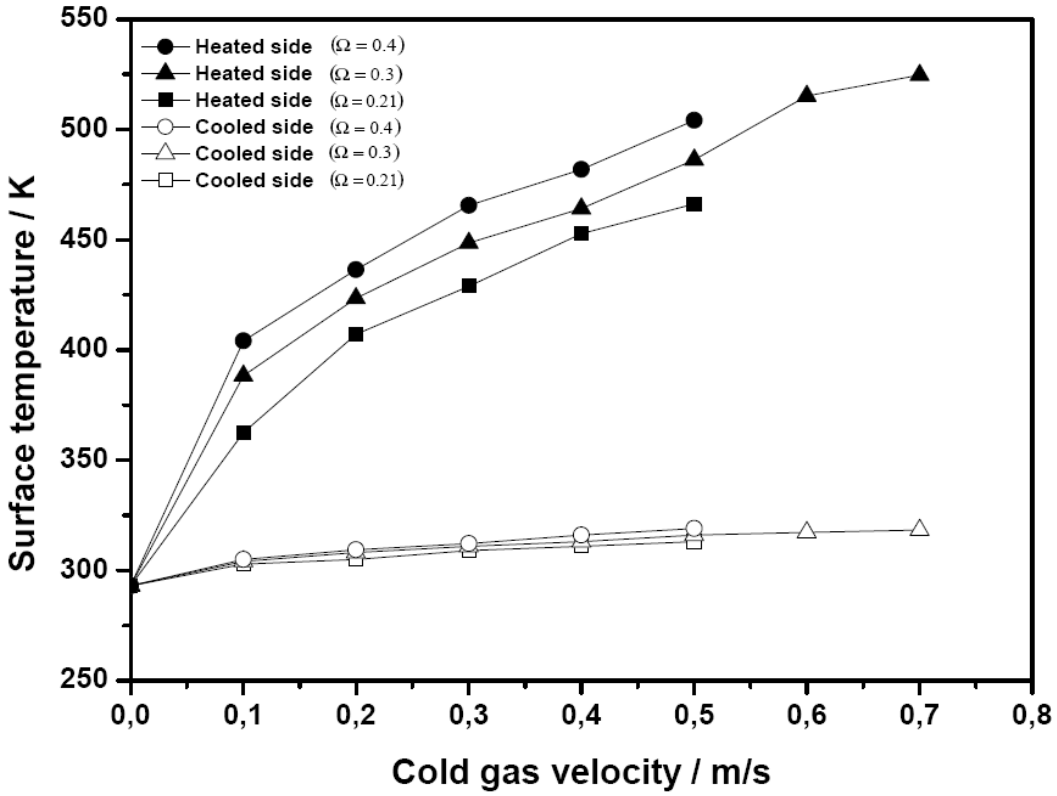

Figure 5.9: Surface temperature measurement at the stagnation point for stoichiometric ethanol/air flames with a variable oxidizer composition (Ω)

Figure 5.10 shows how the heat flux to the target varied as a function of the oxidizer composition (Ω) which is the O_2 content in the oxidizer, and as a function of the cold gas velocity. The heat flux increased by 20-65% as Ω increased from 0.21 to 0.4. The average was approximately 33%. The possible reason for this trend is discussed in the next paragraph. It is well known that the main heat transfer mechanism for impinging flames jets is forced convection. Increasing the oxidizer composition results in a higher flame temperature and burning velocity and therefore a higher gas velocity. Consequently, the forced convection will be enlarged [101]. To put it another way, the reaction rates drop by decrease the oxidizer compositionΩ. This also explains the lower heat flux as compared to the case with higher oxidizer composition.

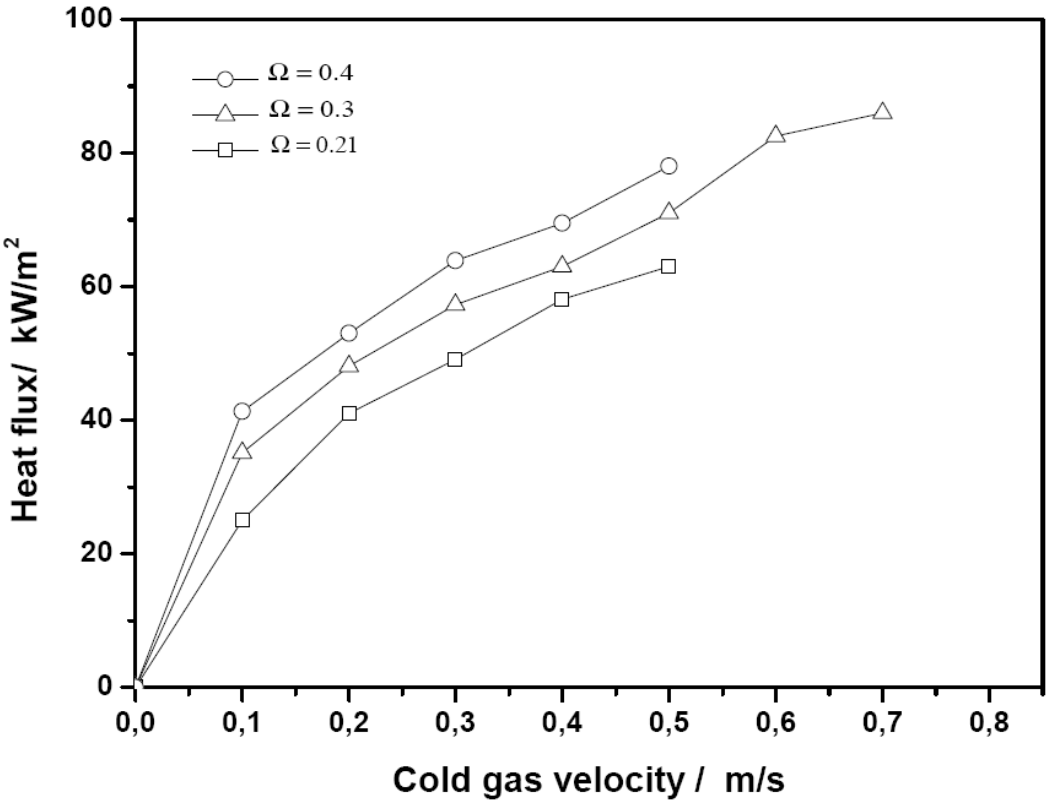

Figure 5.10: Stagnation point heat fluxes for stoichiometric ethanol/air flames with a variable oxidizer composition (Ω)

The heat flux is plotted vs oxidizer composition (Ω) for different cold gas velocities of 0.1 and 0.5 m/s, as shown in Figure 5.11. For all values of cold gas velocity, it was found that the heat flux increases as concentration of oxygen in oxidizer increases, and this effect is more significant at a relatively low gas velocity. At U=0.1 m/s, the heat flux increased by 65% as the fraction of oxygen Ω increased from 0.21 to 0.4 in the oxidizer stream. At U= 0.5 m/s, the heat flux increased by 23%.

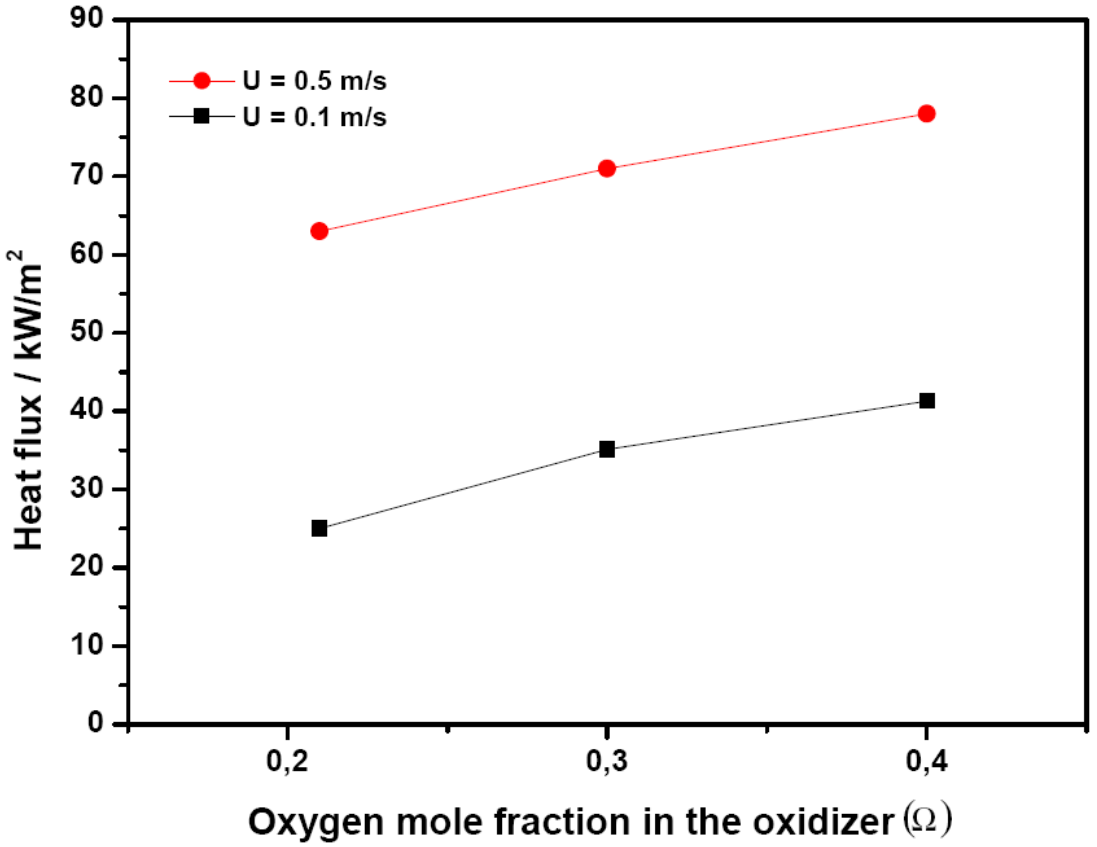

Figure 5.11: Stagnation point Heat fluxes for two different cold gas velocities, as a function of hydrogen concentration in fuel mixture

5.1.1.5.2 Comparison of the influence of inert gas additives

Additives such as N_2 and Ar are chemically inert. They do influence, however, the physical properties (e.g. conductivity, specific heat, etc.) of the mixture. Therefore, inert gas additives were used as dilution in the combustion processes.

In our present work, a stoichiometric ethanol/oxygen/argon flame is compared to ethanol/oxygen/nitrogen flame; both flames have the same quantity of ethanol and oxygen. Moreover, nitrogen and argon were added in proportions commonly used for air. Figure 5.12 displays the heat flux at the stagnation point for the two cases as a function of cold gas velocity.

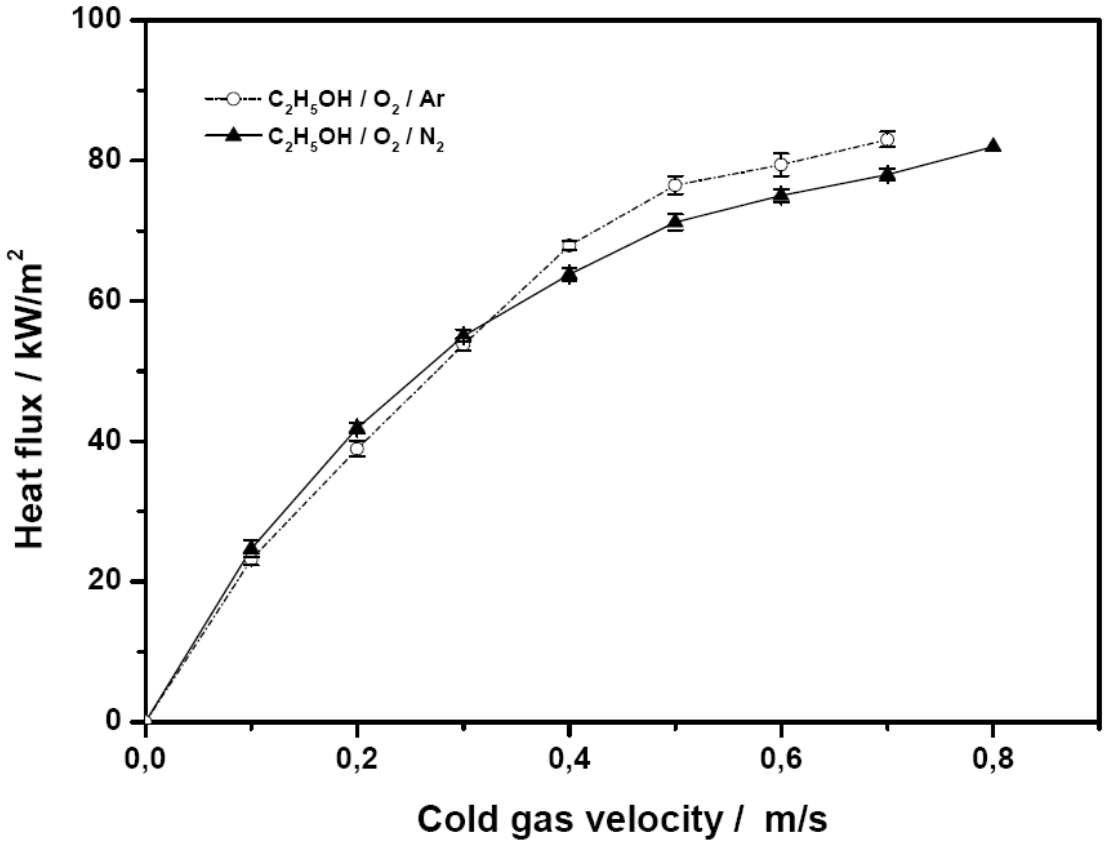

Figure 5.12: Stagnation point heat fluxes for stoichiometric ethanol/oxygen/argon and ethanol/oxygen /nitrogen flames

At low gas velocity, addition of nitrogen and argon to the ethanol/oxygen mixture produced almost similar effects. However, at higher gas velocity, it was found that the peak heat flux for ethanol/oxygen/argon flame is higher (7 % larger) than for ethanol/oxygen/nitrogen flame. This is due to the lower heat capacity of argon as compared to nitrogen. It is a result of the increase in flame temperature as well as the heat flux. In other words, adding inert gas with a relative high heat capacity, such as nitrogen, increases the total heat capacity of the fuel-oxygen-inert gas mixture; as a result, the mixture absorbs more heat during the combustion and reduces the temperature of combustion.

In addition, the inert gas addition seems to affect the flame speed by influencing the ratio of thermal conductivity to specific heat. Qiao et. al [102] showed that the capability of the diluents, inert gases, to reduce flame speed increases on the order of He < Ar < N2 < CO2, due to their increased specific heat and decreased transport rates. Accordingly, it was generally found a decrease in flame speed will cause a decrease in flame temperature.

5.1.2 Laminar premixed ethanol/hydrogen/air flames

Hydrogen and ethanol are currently recognized as promising fuels for many industrial applications because of their ability to be derived from various sources, many of which are renewable. Additionally, hydrogen, which is the cleanest burning chemical fuel, helps to reduce the pollutants such as soot and unburned hydrocarbons. Also, hydrogen is characterized as having the highest energy combustion energy of the chemical fuels and in terms of mass energy consumption, hydrogen exceeds ethanol by about five times [95]. Thus, hydrogen addition to the ethanol/air mixture improves the combustion efficiency.

This present work presents the effect of hydrogen addition on the impingement heat flux of ethanol/air flames. Ethanol-hydrogen-air flames with equivalence ratio of 1.0 and 0.75 and hydrogen mole fraction from 0 to 0.75 were investigated. Furthermore, stoichiometric ethanol-hydrogen-air flames were investigated at various plate-to-burner distance; namely H= 15 mm and H= 3 mm.

5.1.2.1 Hydrogen addition's effect on stoichiometric ethanol/air flames

Figure 5.13 shows the surface temperature measurement on both sides of the ceramic plate for four different hydrogen/ethanol/air flames as a function of cold gas velocity at H =15 mm, all mixtures being stoichiometric. The temperature levels on the cooled back side are only slightly affected by the fuel mixture. In contrast, the measured temperatures on the heated side are significantly affected by the hydrogen addition to the mixture. The temperature levels rise with flow velocity.

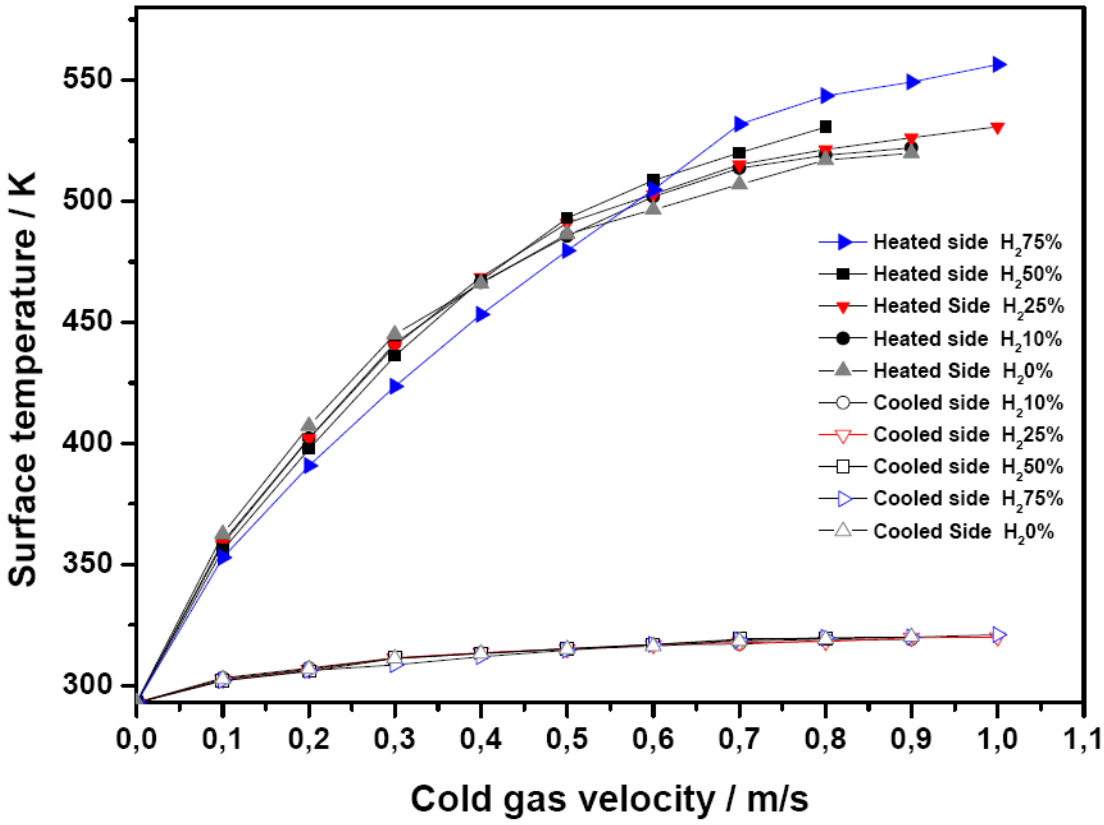

Figure 5.13: Surface temperatures measured for different hydrogen-ethanol fuel mixtures as a function of the cold gas velocity, at H= 15mm.

For instance, at flow gas velocity 0.1 m/s, the temperature difference at H_2 25% and H_2 75% are 56 and 50 K, respectively. At flow gas velocity 0.9 m/s, the temperature differences at H_2 25% and H_2 75% are 206 and 229 K, respectively. This trend is reflected on the calculated heat flux at the stagnation point. Based on the measured temperatures on both sides of the ceramic plate, the heat flux was calculated. Figure 5.14 shows the heat fluxes calculated for the investigated stoichiometric hydrogen/ethanol flames.

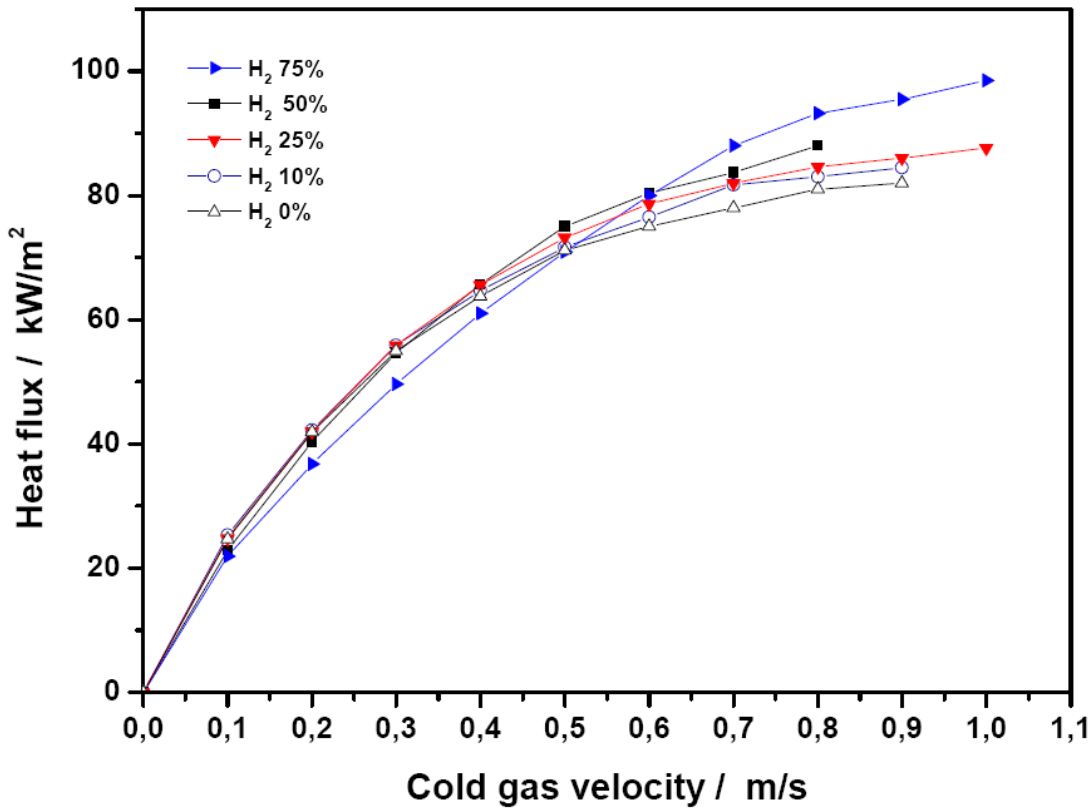

Figure 5.14: Calculated heat fluxes for different hydrogen-ethanol fuel mixtures, as a function of mass flux rate, at H= 15 mm.

It can be seen that the heat flux for all different hydrogen/ethanol flames rise with increasing flow gas velocity. For example, at fuel mixture content of 75% hydrogen, heat flux is at the stagnation point of around 21.9 kW/m^2 at 0.1 m/s and 95.5 kW/m^2 at 0.9 m/s. As mentioned previously, this is expected since the slower flames have a higher rate of heat to the burner. The increase in the heat flux continues significantly until the flow velocity equals the free flame speed. In this regime, the increase in heat flux mainly comes from the reduction of heat losses to the burner with increasing flow velocity. Interestingly, at low gas velocities, the results showed that the heat flux decreases as more hydrogen is added to the mixture. This is due to the fact that the hydrogen increases the free flame speed, which leads to increased flame stabilization on the burner. Thus, more heat is transferred to the burner at gas velocities below the free flame speed, reducing the maximum flame temperature. However, this trend changes at higher cold gas velocities. At high cold gas velocity,

the results indicated that increasing the hydrogen content in the mixture leads to increased heat flux. This trend is expected, because as it is well known that hydrogen addition increases the flame temperature. However, in the present case, this trend only appears later — specifically, when the cold gas velocity is higher than the free flame speed. In this case, the flame is stabilized at the stagnation plate and thus reduces the heat loss to the burner.

Figure 5.15 shows the heat flux as a function of hydrogen concentration in the fuel mixture at two different gas velocities; namely U=0.3 m/s and U=0.8 m/s. At U=0.3 m/s, the heat flux decreases approximately 10% by increasing the concentration of hydrogen (from 0% to 75%). Otherwise, at U= 0.8 m/s, the heat flux increases around 15%.

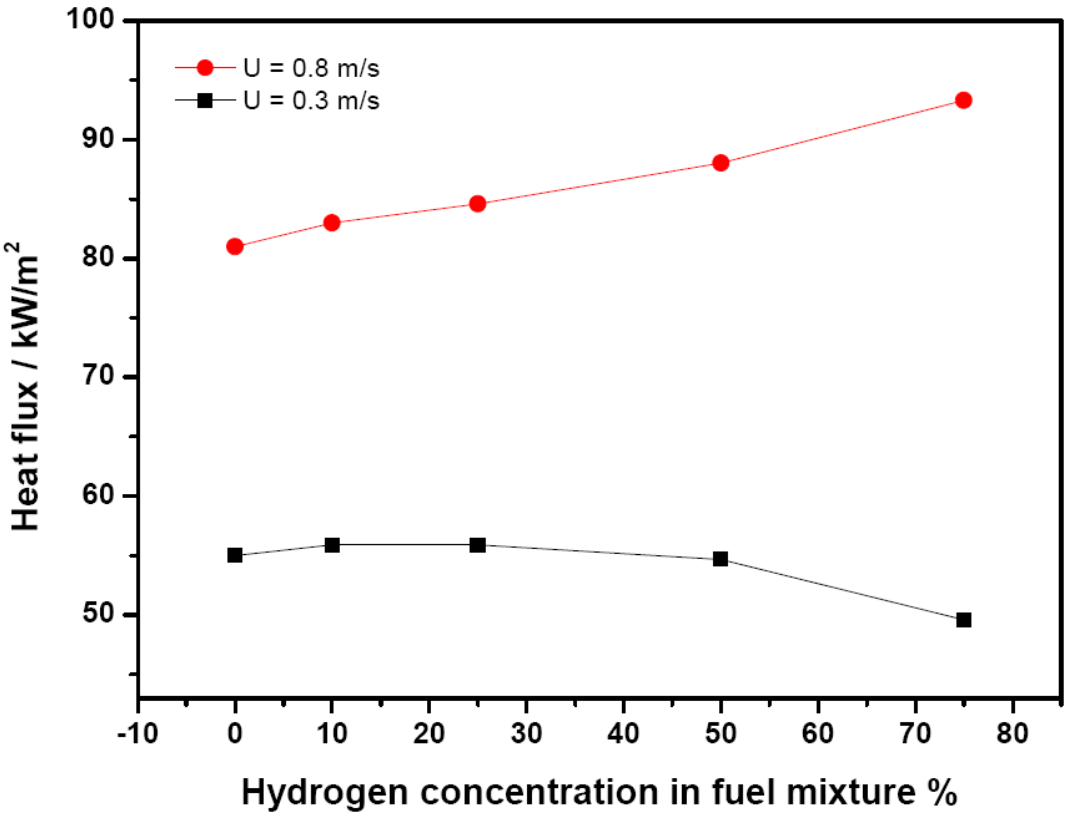

Figure 5.15: Heat flux calculated at the stagnation point for two different cold gas velocities, as a function of hydrogen concentration in fuel mixture

5.1.2.2 Effect of plate-to-burner distance

Figure 5.16 illustrates the influence of hydrogen addition on the heat flux at different plate-to-burner distances. For all hydrogen-ethanol mixtures, the results indicated that as the separation distance increased, the heat flux decreased.

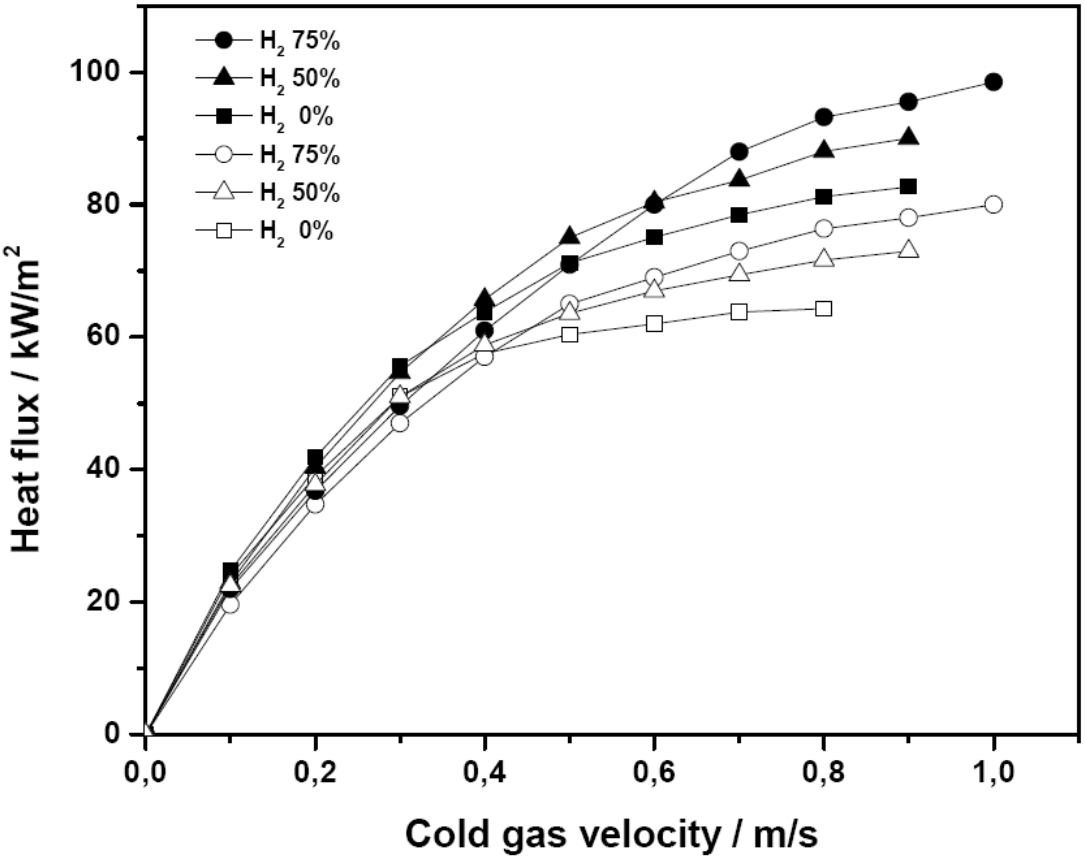

Figure 5.16: Heat flux at stagnation point for different hydrogen-ethanol fuel mixtures at various burner to plate distances (solid symbols: H=15 mm, hollow symbols: H=30mm)

In Figure 5.17, the heat flux is plotted vs the hydrogen mole fraction in fuel mixture for different gas velocities, namely 0.3 and 0.8m/s, and at plate-to-burner distances of 15 and 30 mm. At cold gas velocity 0.8 m/, it was found that increasing hydrogen fraction can raise the heat flux, whatever the plate-to-burner distance. On the contrary, at cold gas velocity 0.3 m/s, increasing the hydrogen fraction can reduce

the heat flux. This can be easily understood in terms of the stability mechanism of the flame.

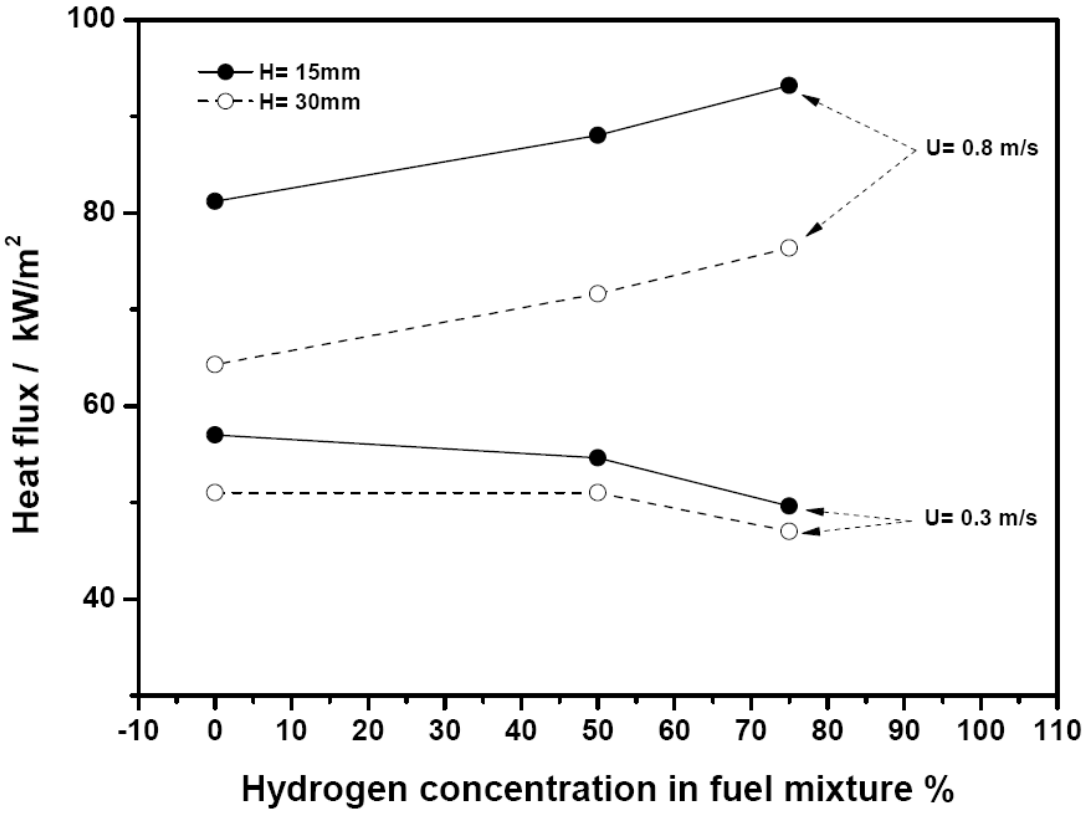

Figure 5.17: Heat flux as a function of hydrogen concentration in fuel mixture for cold gas velocities of 0.3 m/s and 0.8 m/s and at plate-to-burner distances of 15mm and 30mm

It is clear that increasing the separation distance causes a decrease in the heat flux, whatever the hydrogen fraction is for both two velocities. This trend is more significant for higher cold gas velocity (0.8 m/s). The likely reason for this trend is that, in the high gas velocity scenario, the flame is stable on the stagnation plate. Hence, any change in the separation distance between the burner and the plate has a remarkable effect on the heat flux at the stagnation point. Otherwise, in the low gas velocity case (0.3 m/s) the flame will be stabilized on the burner; thus the separation distance has relatively low influence on the heat flux, especially at high hydrogen mole fractions.

5.1.2.3 Effect of the equivalence ratio

In Figure 5.18, heat flux as a function of cold gas velocity is shown for both fuel-lean and stoichiometric hydrogen-ethanol-air flames. Regardless of the amount of hydrogen fraction in fuel mixture, it was observed that values of the heat flux for the stoichiometric flames are higher as compared to those for the lean flames. This is attributed to the availability of sufficient air for complete combustion of the fuel, which led to enhanced mixing and combustion in the impingement region. However, the main trend for lean flame is approximately similar to that of stoichiometric flame.

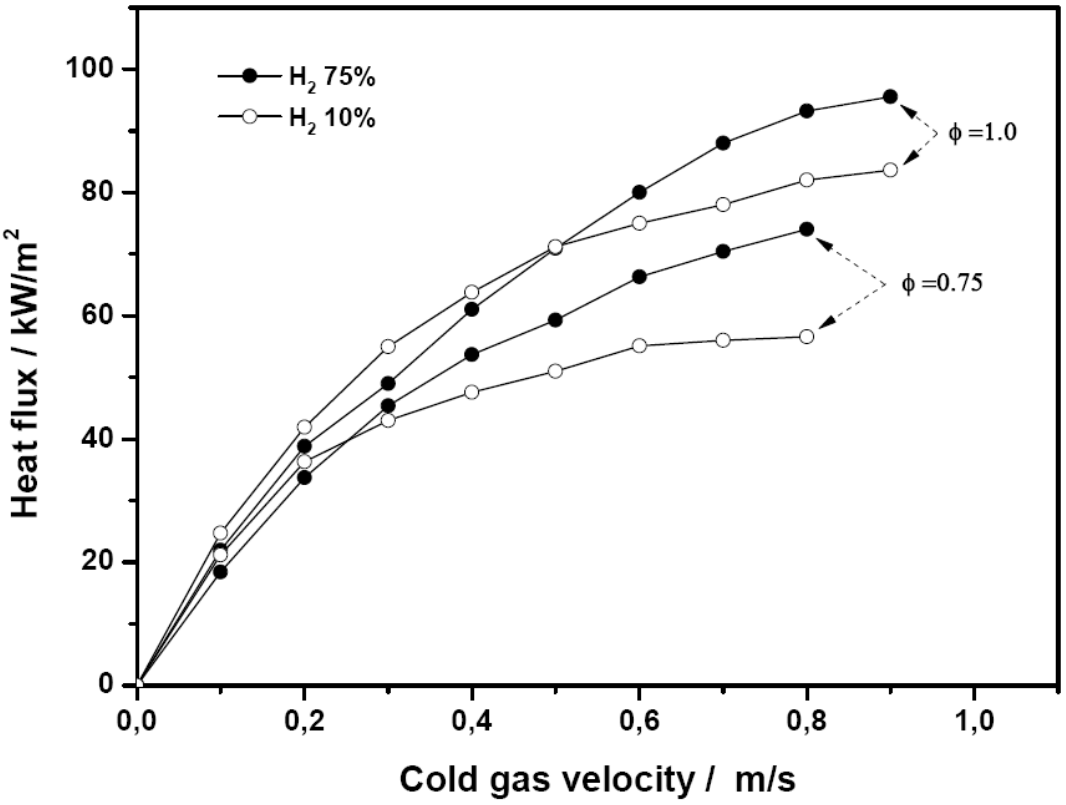

Figure 5.18: Heat flux at stagnation point as a function of cold gas velocity for different hydrogen-ethanol fuel mixtures, at equivalent ratios of 0.75 and 1.0

Furthermore, the results indicate that for the two equivalence ratios ϕ= 0.75 and 1.0, adding hydrogen to ethanol-air mixture will increase the heat flux; this effect is more significant in the case of a lean flame. For example, at gas velocity U = 0.8 m/s,

increasing the hydrogen fraction (from 10% to 75%) raise the heat flux around 31% and 14 % for the lean and stoichiometric flame, respectively.

5.2 Flame impinging on a flat plate at different angles

This configuration, seen in Figure 5.19, has importance in some applications —in particular, those applications that have constraints on positioning of the burner (or in some cases, due to the shape of the impingement surface). Even if a normal impingement is intended, the actual impingement may occur at an oblique angle relative to the surface. This is due to the influence of the flow from the neighboring jets, which causes the flame jet to deflect before impingement. However, this configuration has been largely ignored in research (for further details, see Chapter 2). In these studies [27-29], information about the impingement heat transfer from flame jets was rarely provided. Especially regarding when a flame is produced by burning ethanol in air. Due to the inclination between the burner and the target, the wall jet region is characterized into two regions, as shown in Figure 5.19. The direction toward which the nozzle is inclined is defined as the "uphill side" and the other direction is defined as the "downhill side" [28]. The effect of the inclination of an impinging ethanol/air flame on the heat flux was investigated. The flame was fixed with an equivalence ratio of 1.0. The heat flux were determined as a function of three parameters: (a) cold gas velocities in the range of 0.1-0.6 m/s (b) inclination angle of the flame jet relative to the plate in the range of 90-50° and (c) plate to burner distances, namely H=30 and 60 mm. The Heat flux is measure at the geometrical impingement point (O), as seen in Figure 5.18.

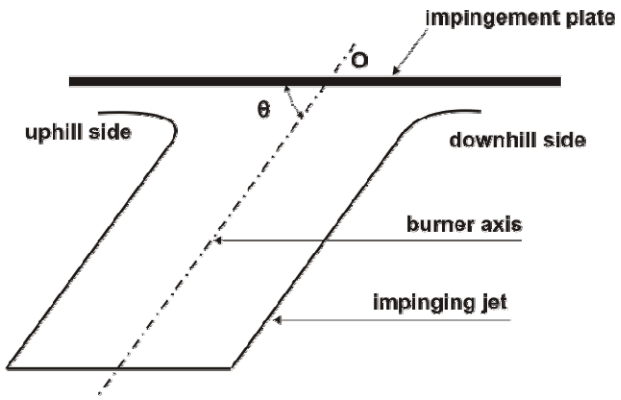

Figure 5.19: Flow regions of an inclined impinging flame jet

In figure 5.20, the measured surface temperatures on the both sides of the stagnation plate are plotted vs. cold gas velocity for different inclination angles θ of 50°, 70° and 90°, at constant separation distance H= 30mm. It can be observed that the maximum temperature difference for angels of 50°, 70° and 90° are 116, 131 and 138 K, respectively. The smaller the inclination angle, the lower the temperature difference between both sides of the plate.

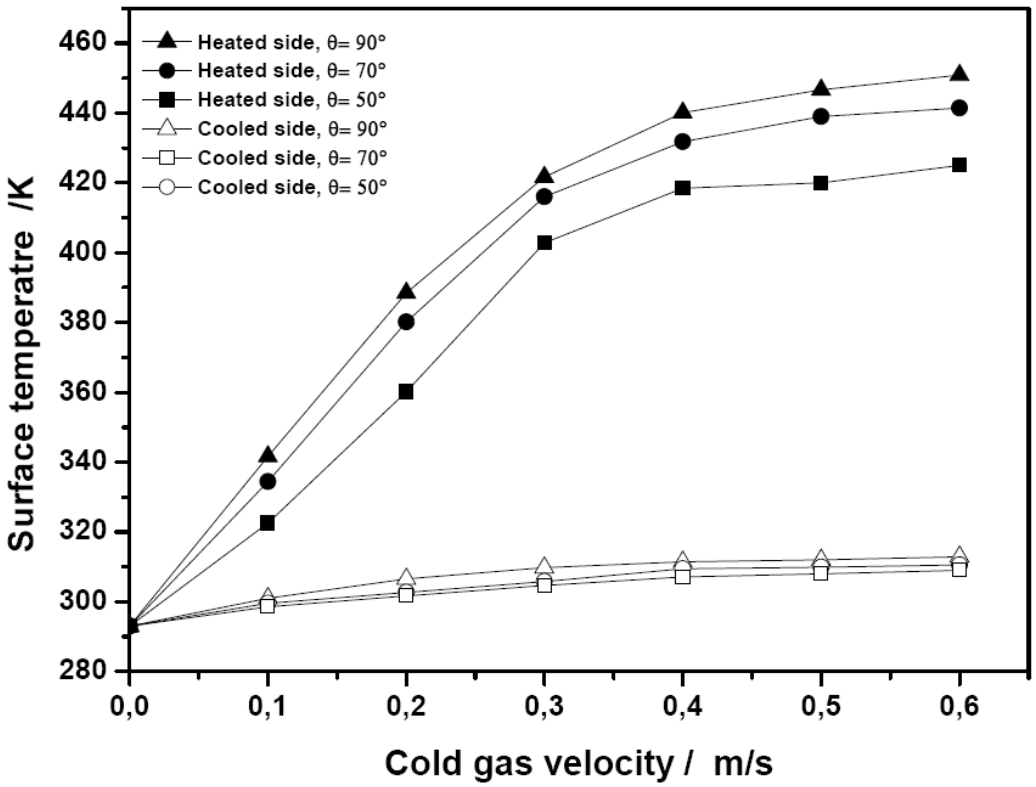

Figure 5.20: Surface temperature measurement for stoichiometric ethanol/air flames under different inclination angles, at H=30mm.

The trend of the measured surface temperatures is reflected in the calculated heat flux, as shown in Figure 5.21. Accordingly, the heat flux from a flame jet impinging on a flat plate is highly affected by the angle of incidence.

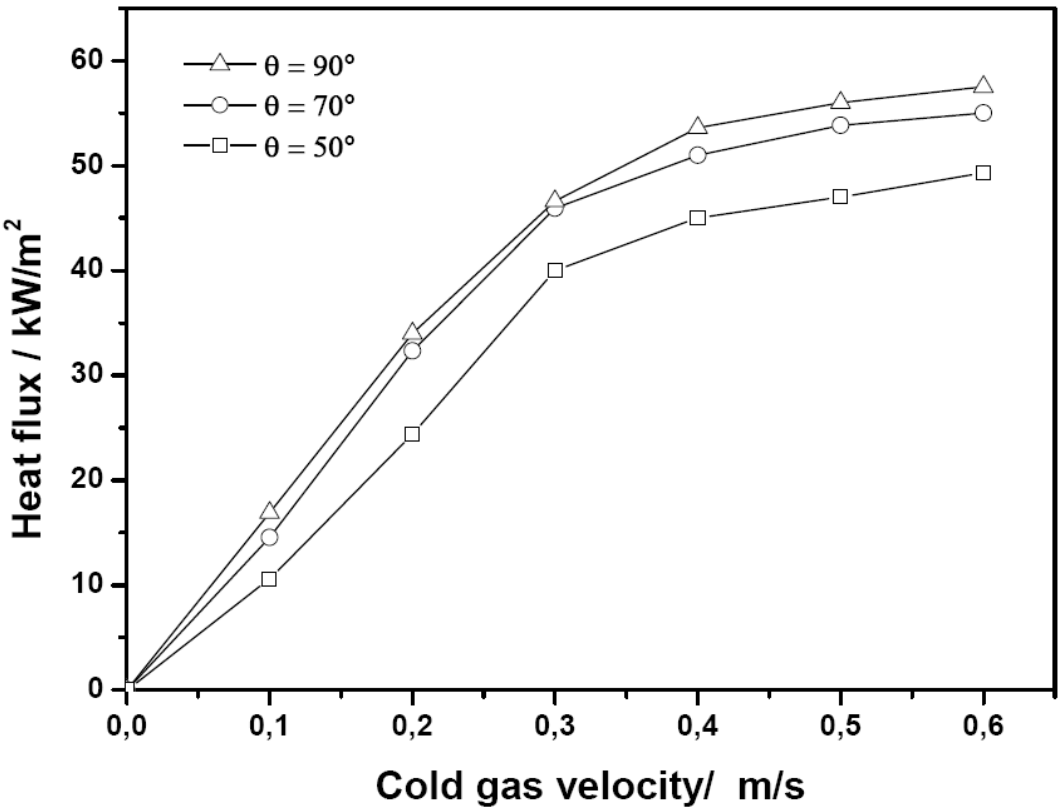

Figure 5.21: Heat flux calculated for stoichiometric ethanol/air flames under different inclination angles, at H=30mm.

Also in figure 5.21, it was found that the heat flux decreases whereas the cold gas velocity increases when the inclination angle is decreased. When the inclination angle is small, e.g. θ = 50°, the maximum heat flux calculated is 58 kW/m^2. The most likely reason for this trend is that decreasing the inclination angle leads to a shift in the location of maximum heat flux away from the geometrical impingement point to the uphill side (compression side). This is due to the change in the magnitude and direction of the velocity of the flame jet. Similar results were obtained by Dong et al. [28] for the premixed butane/air flame and by Kremer et al. [29] for partially premixed methane/air flame jets. According to Kremer et al. [29], the shifting of the maximum heat flux point was due to the unsymmetrical deformation of the flame reaction zone close to the plate. Furthermore, Sparrow and Lovell [103] stated that such phenomena was due to the asymmetric transport in the neighborhood of a local maximum, which caused the displacement of the maximum heat flux point. In other words, the fluid flow divides unevenly around the

impingement surface, and this lead to shift away the stagnation point from the geometrical point.

Figure 5.22 shows the heat flux as a function of the inclination angle for different cold gas velocities, namely U = 0.1 and 0.6 m/s, respectively. For all values of cold gas velocities, the heat flux increases progressively as the inclination angle is increasing. At U = 0.1 m/, the heat flux increased by 59% as the inclination angle increased from 50° to 90°. While at U = 0.6 m/s, the heat flux increased by 16%. That means that, for the range used of velocities in this study, the effect of the inclination angle on heat flux increases as the cold gas velocity decreases.

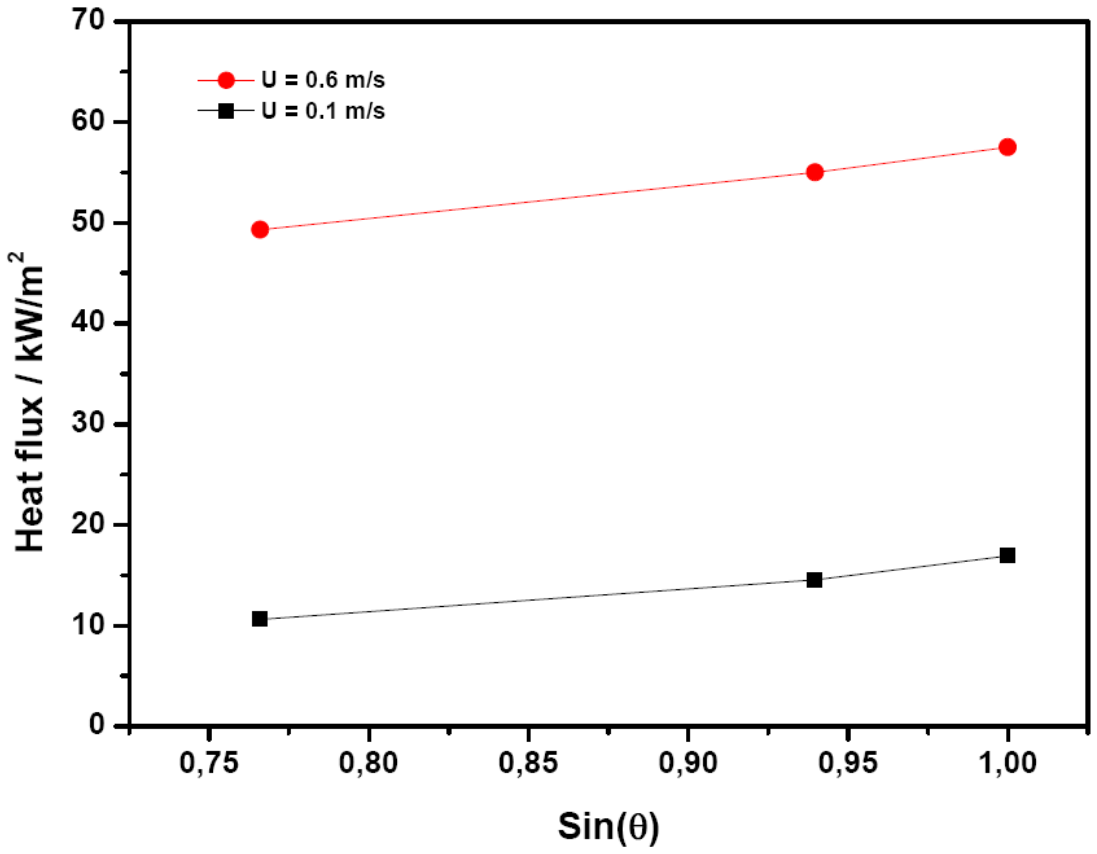

Figure 5.22: Heat flux calculated for stoichiometric ethanol/air flames as a function of inclination angles, at different cold gas velocities of 0.1 and 0.6 m/s

In order to understand the influence of the plate-to-burner distance on the heat flux corresponding to the inclination angle, the heat flux is plotted vs. plate-to-burner distance under different inclination angles of 50° and 90° and for different cold gas velocities of 0.1 and 0.6 m/s, as shown in Figure 5.23. For all values of inclination angle θ and cold gas velocity, it was found that the heat flux decreases as the plate-to-burner distance increases. As mentioned, this is expected because the small separation distance leads to high local heat flux concentration at certain area as compared with large separation distances. Figure 5.23 also shows that the heat flux increases as the cold gas velocity increases. Increasing the cold gas velocity enhances the complete combustion process, and improves the heat transfer coefficient from the flame to the impingement plate. Furthermore, for all inclination angles used in this study, it can be observed that the slope of the heat flux vs. plate-to-burner distance is approximately similar, whatever the cold gas velocity.

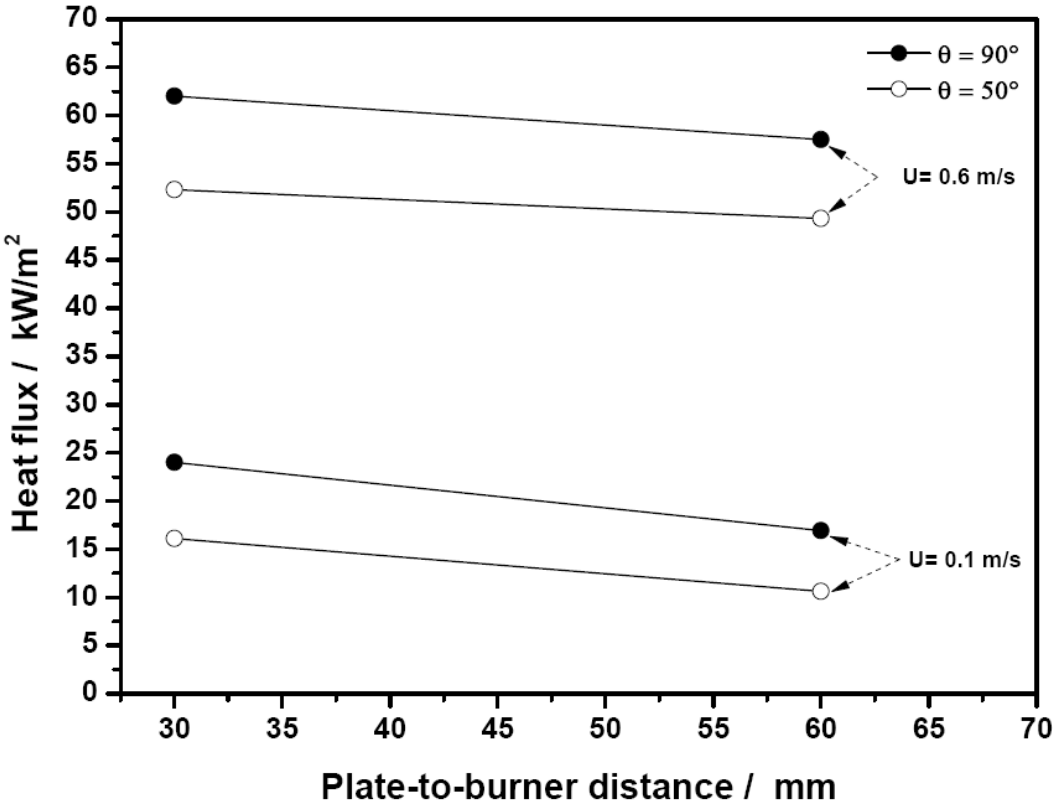

Figure 5.23: Heat flux calculated for stoichiometric ethanol/air flames as a function of plate-to-burner distance under different inclination angles of 50° and 90°, at different cold gas velocities of 0.1 and 0.6 m/s

To summarize, the plate-to-burner distance affects the heat flux but does not affect the shift of the maximum heat transfer point.

To explain the results more, in Figure 5.24, the heat flux is plotted vs the inclination angle for different values of plate-to-burner distance of 30 and 60 mm at constant value of cold gas velocity of 0.6 m/s. Again, for all values of inclination angles, it can be seen that the heat flux increases as the plate-to-burner distance is decreasing. At an inclination angle of 50 °, the heat flux increased by 7% as the plate-to-burner distance decreased from 60 mm to 30 mm. For normal impingement θ = 90°, the heat flux increased by 8%. For all values of the inclination angle in this present study, the influence of the separation distance between the burner and the flat surface on the heat flux is approximately similar.

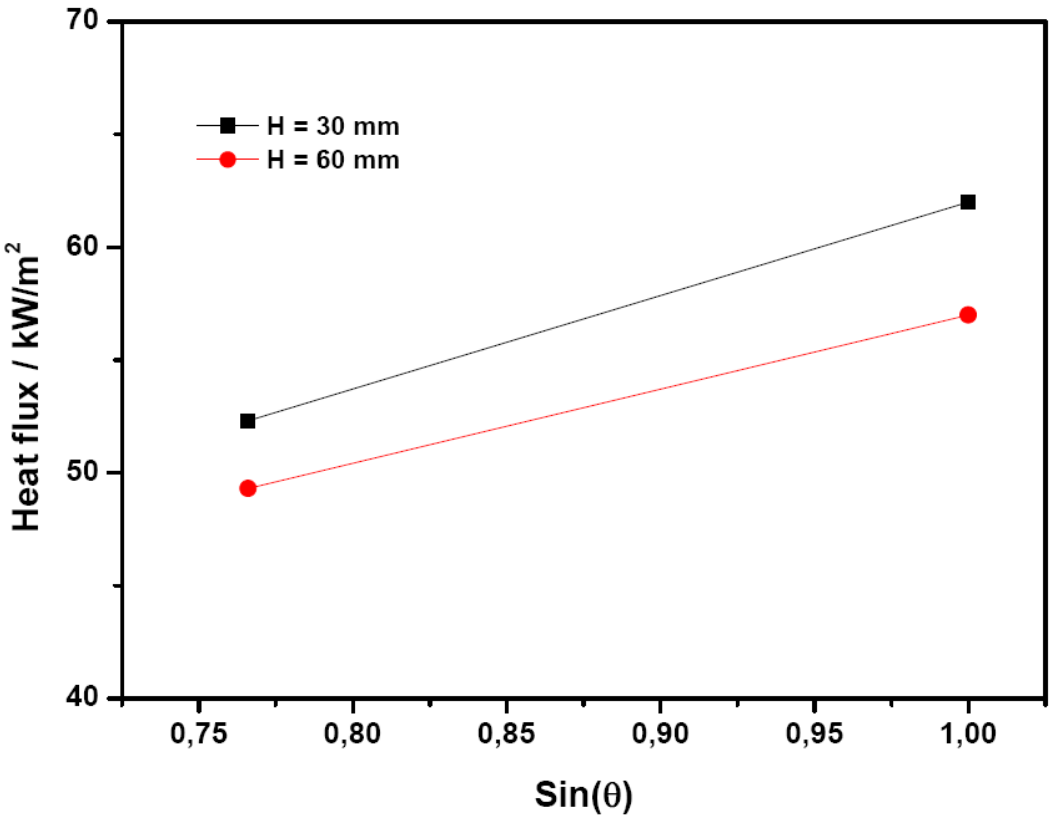

Figure 5.24**:** Heat flux calculated for stoichiometric ethanol/air flames as a function of inclination angles for constant cold gas velocity of 0.6 m/s and at different plate-to-burner distances of 30 and 60 mm

5.3 Flame impinging normally on a cylindrical surface

Flame impingement heating over curved surfaces, such as cylinders, is frequently applied in many industrial processes, e.g. heating round metal billets, the glass industry and in chemical plants. The studies, which cover impingement on curve surfaces, are rare and even out of those most of the studies are related to isothermal jet impingement on curved surfaces [26]. For more details about previous studies, see section 2.1.2.

In this present work, for flame impinging normally on a cylindrical surface, the surface temperature on the flame side was measured using thermographic phosphor. For the water side, the surface temperature was measured using thermocouple. Accordingly, the heat flux of stoichiometric ethanol/air flame impinging normally on a cylindrical surface was determined. The effects of cold gas velocities and the separation distance between the burner and the cylinder were investigated. Also, results were compared with a flat plate under identical operational condition. Moreover, in this configuration, shown in Figure 5.25, the cylinder axis is perpendicular to the burner axis.

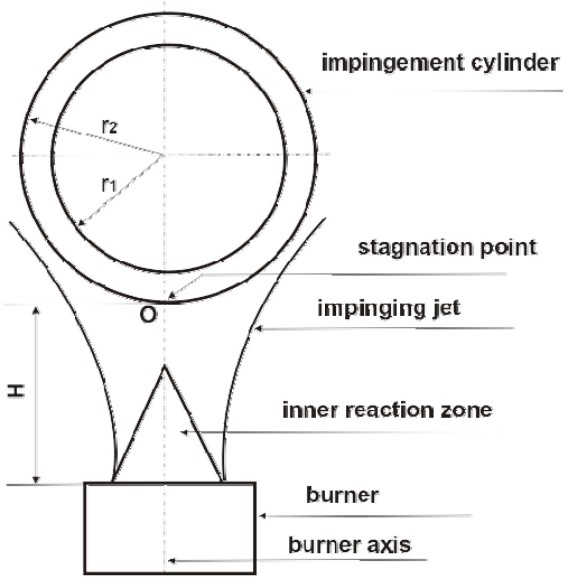

Figure 5.25: Flow field of flame impinging normally on a cylindrical surface

5.3.1 Stagnation point surface temperature and heat flux for stoichiometric flame

Figure 5.26 shows the measured surface temperature on both sides of the cylindrical surface for the stoichiometric ethanol/air flame, at a cylinder-to-burner distance of H = 60mm. It can be observed that the temperatures on both sides increase as the cold gas velocities increase. However, the surface temperatures on the cooled side are slightly influenced by the cold gas velocity as compared with those on the flame side. The reason for that was explained previously. Also, the temperature difference between both sides is increased. The difference in temperatures range from 21.8 K at U = 0.1 m/s to 140 K at U= 0.6 m/s.

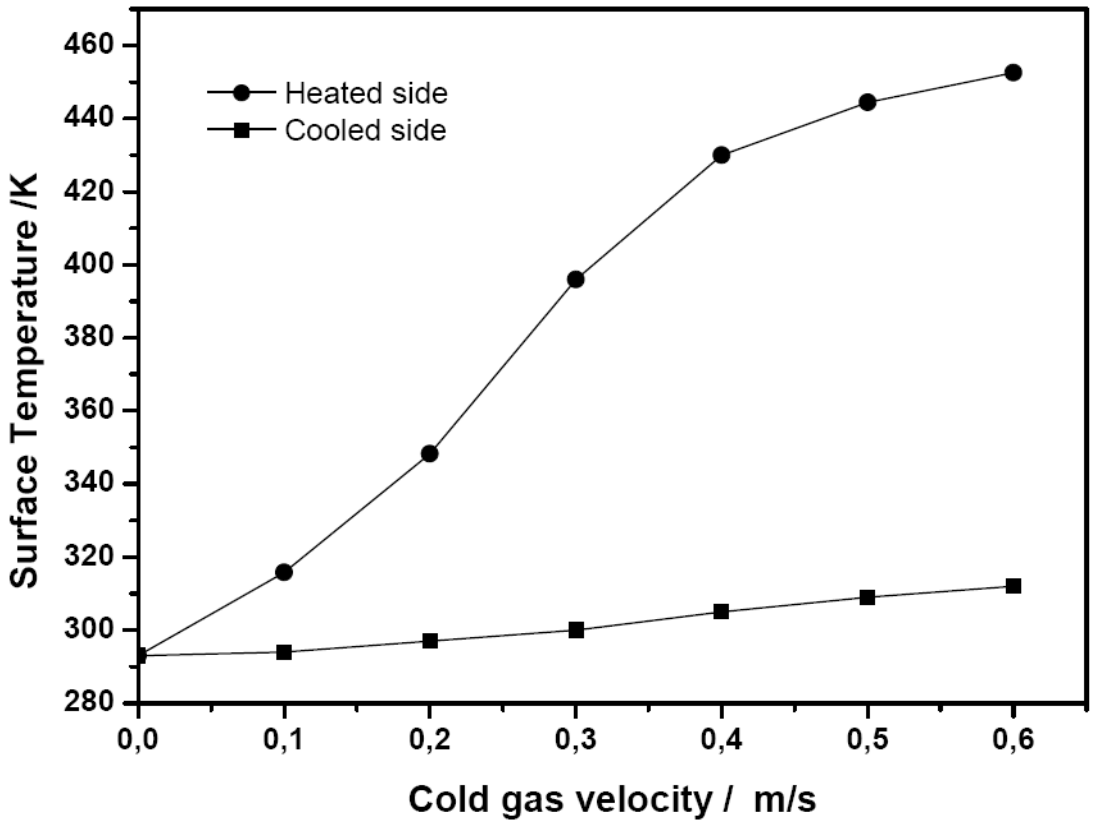

Figure 5.26: Surface temperature measurement for stoichiometric ethanol/air flames impinging normally on a cylindrical surface, at H= 60mm.

Based on the measured temperatures, the heat flux was calculated. In the case of hollow cylinder, the heat flux is not constant in the radial direction; it depends on cylinder radius (r). That is, as the radius increases from the inner wall to the outer wall, the heat flux area increases.

Figure 5.27 shows the comparison of heat flux at the outer and inner surface areas. As expected, the heat flux at the inner surface area is higher than those at the outer surface area. Furthermore, the heat flux increases as the cold gas velocity increases. The viscous effects are more dominant at the low cold gas velocity. Thus the boundary layer thickness is reduced at the stagnation region as the cold gas velocity increases; consequently, the heat flux increases.

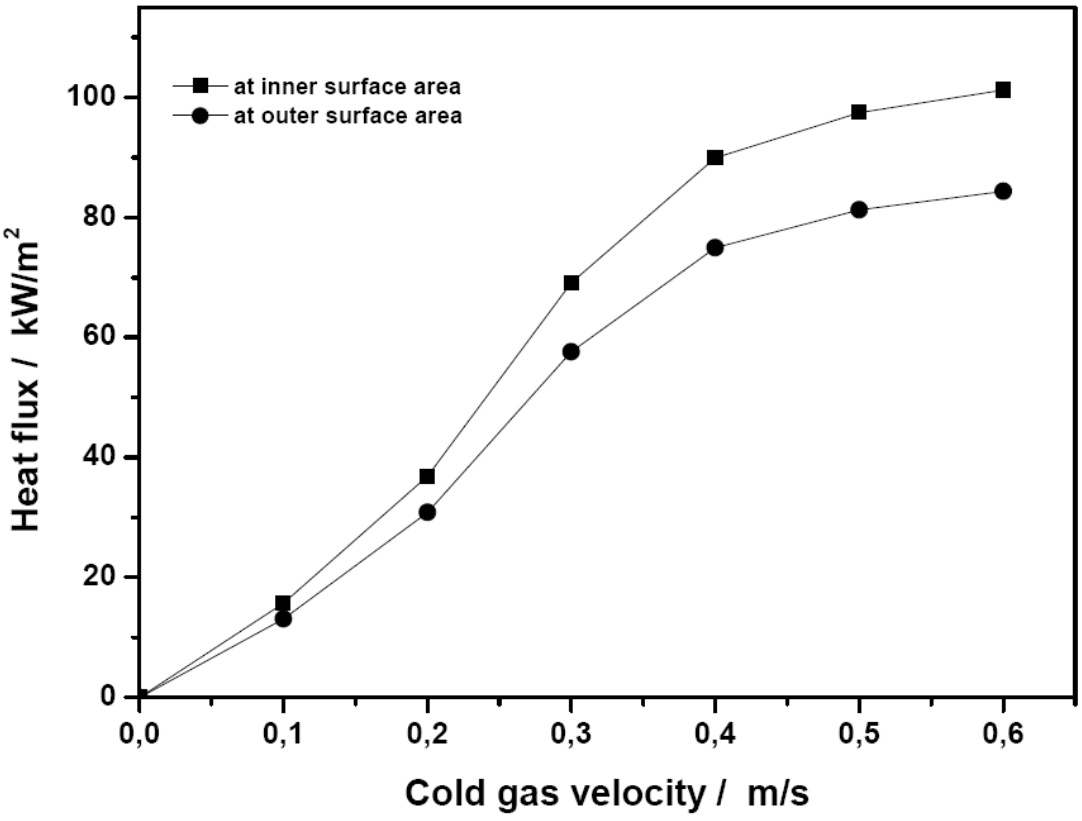

Figure 5.27: Comparison between the stagnation point heat flux at the outer and inner surface area for stoichiometric ethanol/air flame, at H = 60 mm

In most previous studies, the local heat flux was measured at the forward stagnation point of the pipe. In this study, the heat flux is calculated at the out surface area for all the following investigations.

5.3.2 Comparison of stagnation point heat flux results between flat and cylindrical surface

To understand more about the effect of the impingement surface configuration on the heat flux, particularly the curvature influence. Figure 5.28 shows comparison for stagnation point heat flux over flat pate and cylindrical surface for ϕ = 1.0 and H = 60mm.

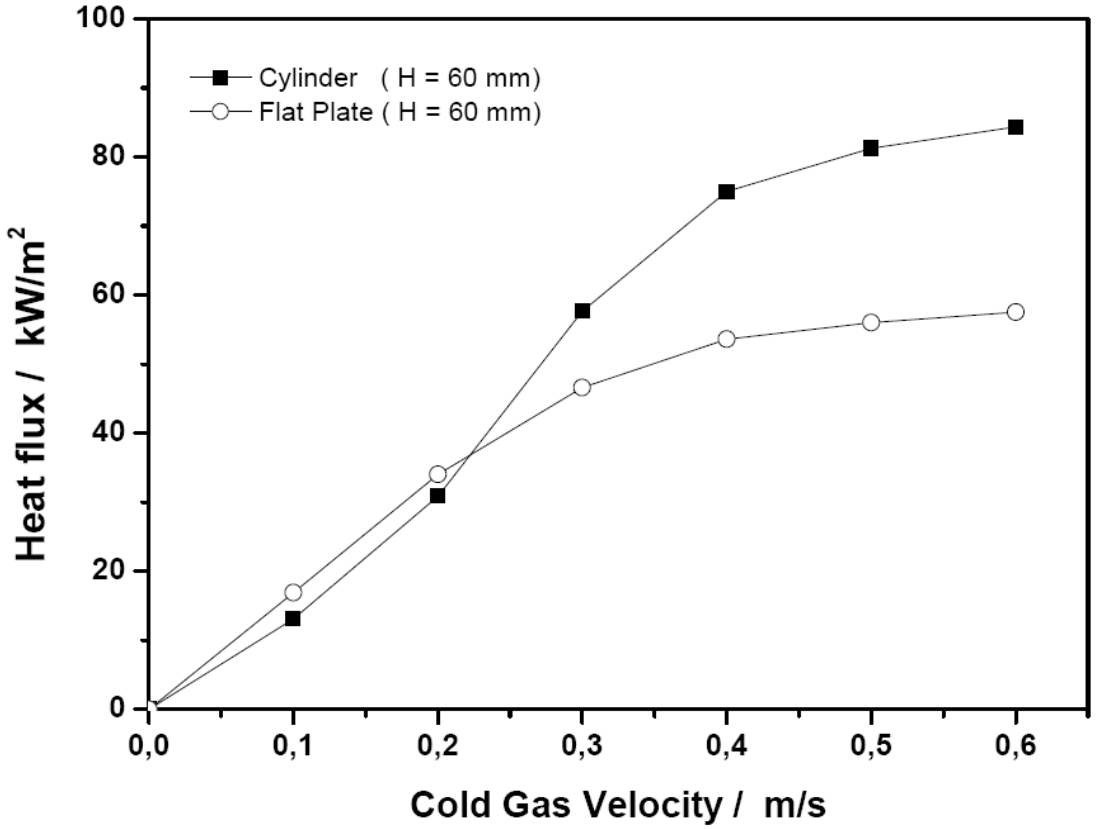

Figure 5.28: Comparison of stagnation point heat flux over the flat plate and cylindrical surface.

Regarding the stagnation point, at cold gas velocities higher than 0.2 m/s, the heat flux has the highest value in the cylindrical surface case compared to the flat plate case. The flat plate does not allow the fluid to diffuse easily as compared with the cylindrical surface; fluid cannot flow smoothly on the surface. Therefore, at the stagnation region, the formed boundary layer on the flat surface is thicker than those on the cylindrical surface. On the other hand, a cylindrical surface does not resist against gases motion, so the flow passes the surface without any shape of restriction, and hence the thermal boundary layer is thinner at the cylindrical surface. As a result, stagnation point heat flux was higher for the cylindrical surface. Chander and Ray [26] and Van der Meer [2] stated that the higher stagnation point heat flux at a cylindrical surface can be attributed to higher radial velocity gradient of the burnt gases just outside the boundary layer as compared to the flat plate. Moreover, this behavior can be interpreted by using the centrifugal force effect on a cylindrical surface. Since this force causes the flow to be more stable, and fluid flows more smoothly on the cylindrical surface in related to the flat plate, the formed thermal boundary layer is thinner at the cylindrical surface. Consequently, heat flux is higher than on the flat plate case.

Figure 5.29 shows the comparison between the stagnation point Nusselt number of a flat plate and cylindrical surface for ethanol/air flame jet and isothermal jet at ϕ=1.0 and with H = 60 mm. The Nusselt numbers were calculated using theoretical correlation (see equations 3.17 and 3.18). For impinging isothermal and flame jets, it can be observed that the Nusselt number has the higher value at the cylindrical surface as compared with the flat plate. Furthermore, the Nusselt number increases as the cold gas velocity increases for both cylindrical surface and flat plate. On the other hand, it was found the Nusselt number for the flame jet is higher those for the isothermal jet. This is behavior because the flames contain a lot of free radicals that will exothermically recombine close to and on the cold surface and augment the heat transfer. It is difficult to determine the Nusselt number from heat flux measurements because there are two unknowns, namely the temperature and heat transfer coefficient of the flame. Hence, it is not possible to compare the Nusselt number from the experimental measurements with those from the theoretical correlation.

In summary, based on the above results, it can be concluded that the impingement surface shape has a serious effect on the stagnation point heat flux**.**

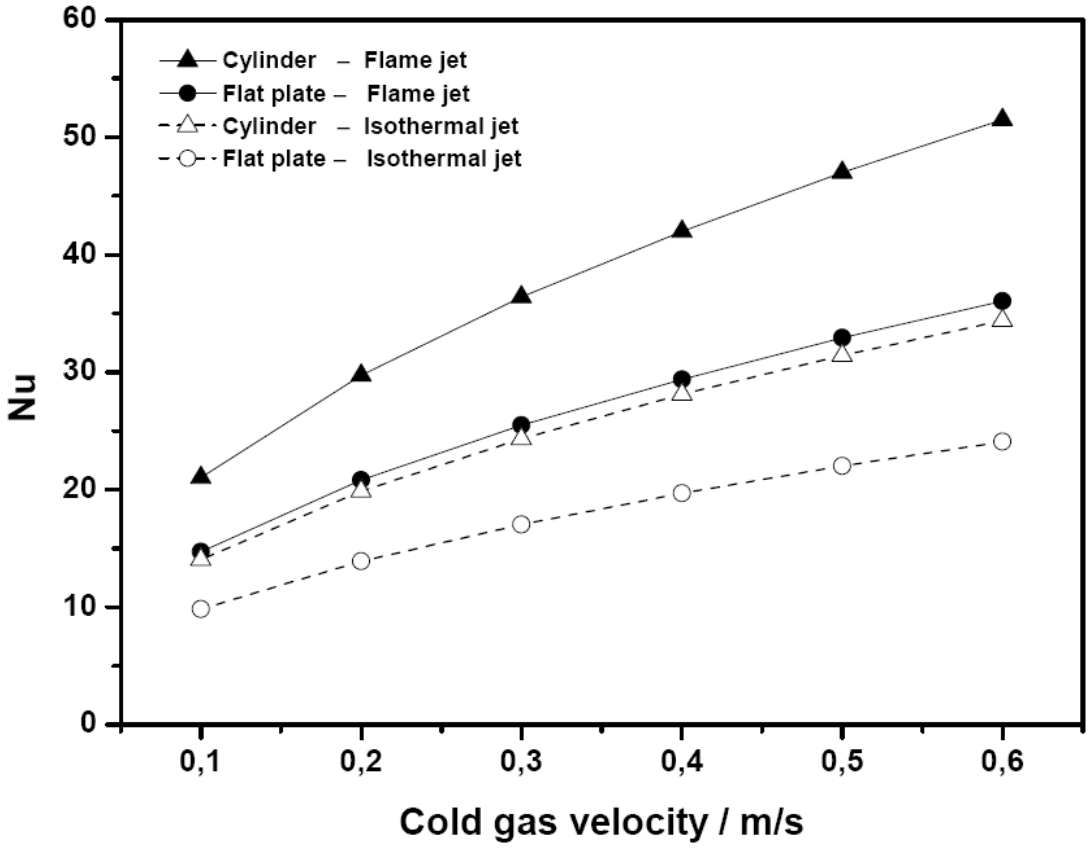

Figure 5.29: Comparison between the stagnation point Nusselt number of a flat plate and cylindrical surface, at ϕ =1.0 and with H = 60 mm

5.3.3 Effect of cylinder-to-burner distance (H)

Figure 5.30 shows the effect of cylinder-to-burner distance on the stagnation point heat flux for stoichiometric ethanol/air flame impinging normally on a cylindrical surface. It can be observed that heat flux increases as the separation distance decreases, as expected for the flat plate case (see section 5.1.1.3). This is due to the same reason that was discussed previously. In addition, when at a small separation distance, the tip of the inner reaction zone moved closer to the cylindrical surface

resulting in a higher stagnation point heat flux. This high value of heat flux can be attributed to high mean velocity and temperature of combustion products in the vicinity of the tip of the inner reaction zone.

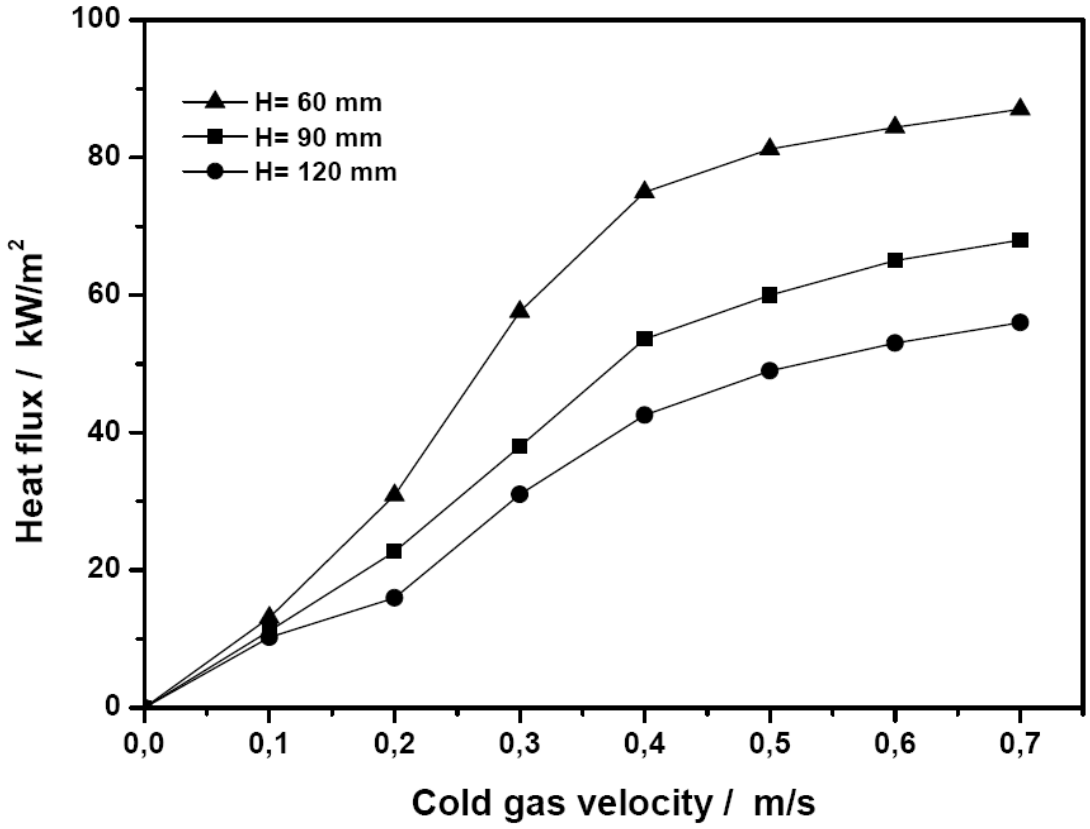

Figure 5.30: Stagnation point heat fluxes for stoichiometric ethanol/air flames at various burner-to-cylinder distances

5.4 Summary

All results of this experimental study are presented in this chapter. The main objective for this work is to study the heat flux at the stagnation point of an impinging flame jet. Three different configurations for flame impingement were investigated: (1) normal to a flat plate, (2) inclined to a flat plate, and (3) normal to a cylindrical surface in crossflow. In the first case, two different flames were

investigated; namely, ethanol/air flames and hydrogen/ethanol/air flames. In the other two cases, only ethanol/air flames were investigated.

This study examined the effects of the velocity of the air/fuel jet, thermal conductivity of the impingement surface, the equivalence ratio of the air fuel jet, the separation distance between the burner rim and the impingement surface, the oxidizer composition and the hydrogen concentration in the fuel mixture. Furthermore, stagnation point heat flux of ethanol/oxygen flames in the presence of two various inert gases — argon and nitrogen — were investigated. In addition, the effect of the angle of incidence between the burner and the impingement flat plate on stagnation point heat flux was tested. Also, the results of the cylindrical surface were compared with flat plate results under identical operating conditions.

Based on these results, the following conclusions can be drawn:

- Using impingement surface with low thermal conductivity improves the accuracy of measurements.
- When the cold gas velocity is increased, stagnation point heat flux received by the impingement surface increases; increasing the cold gas velocity enhances the heat transfer coefficient.
- When the separation distance between the burner and the impingement surface is increased, the heat flux is decreased; the small value of separation distance may leads to high local heat flux concentration in a certain area.
- The highest heat flux was for the stoichiometric flames, but much lower for lean flames. Furthermore, it was found that the heat flux for stoichiometric and rich flames is close to each other.
- Using oxidizers with a higher concentration of oxygen than is present in air leads to increase in the heat flux; increasing the oxygen concentration improves the combustion process.
- For a given diluent concentration at high cold gas velocity, ethanol/oxygen/argon flames produce a relatively high heat flux at the stagnation point as compared to ethanol/oxygen/nitrogen flames, due to the higher thermal diffusivity of argon.

- Increasing the concentration of hydrogen in a fuel mixture enhances the stagnation point heat flux. This is because the hydrogen enhances the flame temperature and consequently the heat transfer from the flame.
- Stagnation point heat flux decreases as the inclination angle is reduced. The maximum heat flux was at the normal impingement angle $\theta = 90°$.
- In comparison to flat plate, a cylindrical target has higher stagnation region heat fluxes.

6 Summary and conclusion

This research work was conducted to achieve a better understanding of the stagnation point heat flux characteristics of impinging flame jets, namely ethanol/air and ethanol/hydrogen/air flames. This study was essentially experimental. The method followed to determine the heat flux was as follow:

- The temperatures were measured from both sides of the impingement surface; namely flame impingement and water cooled side, using thermographic phosphor, which coating the impingement surface. Thermographic phosphor used in this study was chromium-doped aluminum oxide Al_2O_3:Cr (ruby) (chromium concentration = 1.1%). The coating was produced by the sol-gel method, which is very cheap and relatively simple to apply. Green light-emitting diodes (LEDs) were used as excitation source on both sides of the ceramic plate.
- Based on the temperature difference, the heat flux was calculated using a one-dimensional conduction equation.

According to the impingement surface shape, two experimental setups were and used. In the first one, a ceramic flat plate coated with thermographic phosphor was used as an impingement surface. Two flat plates of different ceramic materials were used separately as impingement surfaces to validate and improve the accuracy of measurements. The materials were alumina (λ=22.2 W/(m•K)) and yttria-stabilized zirconia (YSZ) (λ=2.5 W/(m•K)). Both plates were coated with thermographic phosphor. The flat plates were evenly cooled on the back side with the pressurized cooling water. In this setup, two different flames were tested: ethanol/air and hydrogen/ethanol/air flames. Moreover, in this setup, two different types of configurations were studied: flame impinging normally on a flat plate and flame impinging obliquely on a flat plate.

In the second experimental setup, a ceramic tube coated with thermographic phosphor was used as an impingement surface. It was evenly cooled on the inner surface with the pressurized cooling water. In this setup, the outer surface temperature was measured using thermographic phosphor. In contrast, the inner surface temperature was measured using thermocouple. This was due to the difficulty of using thermographic phosphor on the inner surface and the high associated cost. Since the inner surface temperatures almost remain constant due to the high convective nature of the cooling water, it does not affect the heat flux calculation accuracy. In this setup, only stoichiometric ethanol/air flames were investigated.

The major operation parameters include velocity of the air/fuel jet, equivalence ratio of the air/fuel jet, burner-to-impingement surface distance and oxygen mole fraction in oxidizer. They varied in the experiments, in order to examine their effect on the stagnation point heat flux. Other parameters affecting the impingement heat flux include: inert gas additives, hydrogen concentration in the fuel mixture and inclination angel of the flame jet relative to the flat plate. These too were investigated. In order to check the validity of results, at the beginning of our experimental work, the experimental results obtained from the flame impinging normally on a flat plate were compared with modeling results. The experimental results obtained from both experimental setups were discussed and also compared.

The main results of the present work can be summarized as follows:

- Ruby thin film has strong signal intensity and it can be easily excited using light emitting diode (LED). Also, it can be used to measure the impingement surface temperature behind the impinging flame jet without disturbance.

- At identical operational conditions, it was found that using yttria-stabilized zirconia plate as an impingement surface instead of alumina plate improves the heat flux accuracy margin from 13% to 2.3%.

- Trends for both the experimental and modeling results are similar. However, the results obtained experimentally have values that are less than those obtained using modeling. A possible reason for the discrepancy between the model and the measurements could be that the flame speed is not reproduced correctly by the model.

- When the cold gas velocity is increased, the stagnation point heat flux is enhanced. This is mainly due to the increasing supply of air and fuel. Also, increasing the gas velocity enhances the heat transfer coefficient and the thermal boundary layer thickness is reduced with cold gas velocity.

- From these experimental results, two distinct regimes can be distinguished: At low flow rates, the flame is burner-stabilized. In this regime, an increase of the cold gas velocity does not only increase the total combustion enthalpy flux but also reduces the heat loss to the burner. This leads to an increased flame temperature.

- When the plate-to-burner (H) is decreased, the stagnation point heat flux is increased. The relatively high stagnation point heat flux occurred when H= 15mm. The lowest stagnation point heat flux occurred when H = 60 mm.

- Stagnation point heat flux decreases severely when the equivalence ratio decreases from unity. Accordingly, the minimum stagnation point heat flux occurred at ϕ = 0.75. In contrast, the maximum heat flux occurred at ϕ = 1.0. On the other hand, when equivalence ratio is increased from 1.0 to 1.2, the heat flux at the stagnation point slightly decreases.

- Using an oxidizer with a higher percentage of oxygen than in air could enhance the heat flux at the stagnation point.

- As the inclination angle between the burner and the impingement surface reduces, the heat flux at the stagnation point decreases. The maximum heat flux was obtained at normal inclination angle $\theta = 90°$.
- In comparison to a flat plate, the cylindrical surface has a higher stagnation region heat flux.

Future work

The work contained within this thesis provides fundamental information on the stagnation point heat flux for premixed ethanol/air and hydrogen/ethanol/air impinging flame jets. Based on the present study, further work can be carried out in the following areas in order to improve understanding of the flame-impingement heat transfer processes:

- There are many other configurations that have not been explored and have relevance in the context of industrial applications. Some examples include flame impinging on square, rectangular and triangular shape bodies.
- Some more work is required regarding configurations such as flames moving parallel to a plane surface and flame striking normally on a rotating cylindrical surface.
- There are possible combinations of fuel, oxidizer and equivalence ratios that should tested. For example, no stoichiometric propane/air test has been done for flame impinging normal to a cylinder, even though the propane gas is commonly used in domestic heating applications.

References

1. Branch, M.C., et al., *Surface modification of polypropylene films by exposure to laminar, premixed methane-air flames.* Symposium (International) on Combustion, 1998. **27**(2): p. 2807-2813.

2. Meer, T.H.v.d., *Heat transfer from impinging flame jets*. 1987, Deflt University of Technology.

3. Viskanta, R., *Overview of Flame Impingement Heat Transfer: Fundamentals and Applications.* Proceeding of the Fourth Baltic Heat Transfer Conference, 2003: p. 143-158.

4. Baukal Jr, C.E. and B. Gebhart, *A review of empirical flame impingement heat transfer correlations.* International Journal of Heat and Fluid Flow, 1996. **17**(4): p. 386-396.

5. Baukal Jr, C.E. and B. Gebhart, *A Review of Flame Impingement Heat Transfer Studies Part 1: Experimental Conditions.* Combustion Science and Technology 1995. **104**(4-6): p. 339-357

6. Chander, S. and A. Ray, *Influence of burner geometry on heat transfer characteristics of methane/air flame impinging on flat surface.* Experimental Heat Transfer, 2006. **19**(1): p. 15-38.

7. Chander, S. and A. Ray, *Flame impingement heat transfer: A review.* Energy Conversion and Management, 2005. **46**(18-19): p. 2803-2837.

8. Baukal Jr, C.E., *Heat transfer in industrial combustion*. 2010: CRC press.

9. Allison, S.W. and G.T. Gillies, *Remote thermometry with thermographic phosphors: Instrumentation and applications.* Review of Scientific Instruments, 1997. **68**(7): p. 2615-2650.

10. Brübach, J., A. Dreizler, and J. Janicka, *Gas compositional and pressure effects on thermographic phosphor thermometry.* Measurement Science and Technology, 2007. **18**(3): p. 764.

11. Brübach, J., A. Patt, and A. Dreizler, *Spray thermometry using thermographic phosphors.* Applied Physics B, 2006. **83**(4): p. 499-502.

12. Brübach, J., et al., *Determination of surface normal temperature gradients using thermographic phosphors and filtered Rayleigh scattering.* Applied Physics B, 2006. **84**(3): p. 537-541.

13. Atakan, B., C. Eckert, and C. Pflitsch, *Light emitting diode excitation of Cr^{3+}: Al_2O_3 as thermographic phosphor: experiments and measurement strategy.* Measurement Science and Technology, 2009. **20**(7): p. 075304.

14. L. Dong, C.S.C.C.W.L.L., *Heat transfer characteristics of an impinging butane/air flame jet of low Reynolds number.* Experimental Heat Transfer, 2001. **14**(4): p. 265-282.

15. Baukal, C.E. and B. Gebhart, *Heat transfer from oxygen-enhanced/natural gas flames impinging normal to a plane surface.* Experimental thermal and fluid science, 1998. **16**(3): p. 247-259.

16. Kwok, L.C., *Heat transfer characteristics of slot and round premixed impinging flame jets.* Experimental Heat Transfer, 2003. **16**(2): p. 111-137.

17. Dong, L.L., C.S. Cheung, and C.W. Leung, *Heat transfer from an impinging premixed butane/air slot flame jet.* International journal of heat and mass transfer, 2002. **45**(5): p. 979-992.

18. Anderson, J.E. and E.F. Stresino, *Heat transfer from flames impinging on flat and cylindrical surfaces.* Journal of Heat Transfer, 1963. **85**(1): p. 49-54.

19. Van der Meer, T.H., *Stagnation point heat transfer from turbulent low Reynolds number jets and flame jets.* Experimental thermal and fluid science, 1991. **4**(1): p. 115-126.

20. Mizuno, K., R. Mittal, and R. Viskanta, *An experimental study of pre-mixed flame impingement heat transfer*, in *Proceedings of ASME heat transfer division*. 1996, In: Papper DW, et al., : New York. p. 245-252.

21. Milson, A. and N.A. Chigier, *Studies of methane and methane-air flames impinging on a cold plate.* Combustion and Flame, 1973. **21**(3): p. 295-305.

22. Zhang, Y. and K.N.C. Bray, *Characterization of impinging jet flames.* Combustion and Flame, 1999. **116**(4): p. 671-674.

23. Hargrave, G.K., M. Fairweather, and J.K. Kilham, *Forced convective heat transfer from premixed flames - Part 1: Flame structure.* International Journal of Heat and Fluid Flow, 1987. **8**(1): p. 55-63.

24. Hargrave, G.K., M. Fairweather, and J.K. Kilham, *Forced convective heat transfer from premixed flames - Part 2: Impingement heat transfer.* International Journal of Heat and Fluid Flow, 1987. **8**(2): p. 132-138.

25. Jackson, E.G. and J.K. Kilham, *Heat transfer from combustion products by forced convection.* Industrial & Engineering Chemistry, 1956. **48**(11): p. 2077-2079.

26. Chander, S. and A. Ray, *A. Heat transfer characteristics of laminar methane/air flame impinging normal to a cylinder.* . Expeimental Thermal and Fluid Science, 2007. **32**: p. 707-721.

27. Yan, X. and N. Saniei, *Heat transfer from an obliquely impinging circular, air jet to a flat plate.* International Journal of Heat and Fluid Flow, 1997. **18**(6): p. 591-599.

28. Dong, L.L., C.W. Leung, and C.S. Cheung, *Heat transfer characteristics of premixed butane/air flame jet impinging on an inclined flat surface.* Heat and Mass Transfer, 2002. **39**(1): p. 19-26.

29. Kremer, H., E. Buhr, and E. Haupt, *Heat transfer from turbulent free-jet flames to plane surfaces, in Heat Transfer in Flames,*. 1974, Scripta Book Company: Washington, D.C. p. 463-472.

30. Chigier, N.A., *Impinging jet flames.* Combustion and Flame, 1968. **12**(6): p. 575-586.

31. Schulte, E.H., *Impingement Heat-Transfer Rates from Torch Flames.* Journal of Heat Transfer, 1972. **94**(2): p. 231-233.

32. Baukal, C.E. and B. Gebhart, *Surface condition effects on flame impingement heat transfer.* Experimental thermal and fluid science, 1997. **15**(4): p. 323-335.

33. Mohr, J.W., J. Seyed-Yagoobi, and R.H. Page, *Heat transfer from a pair of radial jet reattachment flames.* Journal of Heat Transfer, 1997. **119**(3): p. 633-635.

34. Wu, J., J. Seyed Yagoobi, and R.H. Page, *Heat transfer and combustion characteristics of an array of radial jet reattachment flames.* Combustion and Flame, 2001. **125**(1): p. 955-964.

35. Mohr, J.W., J. Seyed-Yagoobi, and R.H. Page, *Heat transfer characteristics of a radial jet reattachment flame.* Journal of Heat Transfer, 1997. **119**(2): p. 258-264.

36. Dong, L.L., C.W. Leung, and C.S. Cheung, *Heat transfer of a row of three butane/air flame jets impinging on a flat plate.* International Journal of Heat and Mass Transfer, 2003. **46**(1): p. 113-125.

37. Woodruff, L. and W. Giedt, *Heat transfer measurements from a partially dissociated gas with high Lewis number.* Journal of Heat Transfer, 1966. **88**(4): p. 415-420.

38. Hou, S.-S. and Y.-C. Ko, *Effects of heating height on flame appearance, temperature field and efficiency of an impinging laminar jet flame used in domestic gas stoves.* Energy Conversion and Management, 2004. **45**(9): p. 1583-1595.

39. Malikov, G.K., et al., *Direct flame impingement heating for rapid thermal materials processing.* International journal of heat and mass transfer, 2001. **44**(9): p. 1751-1758.

40. Zhao, Z., T.T. Wong, and C.W. Leung, *Impinging premixed butane/air circular laminar flame jetâ€“â€“influence of impingement plate on heat transfer characteristics.* International journal of heat and mass transfer, 2004. **47**(23): p. 5021-5031.

41. Kilham, J.K. and M.R.I. Purvis, *Heat transfer from normally impinging flames.* Combustion Science and Technology, 1978. **18**(3-4): p. 81-90.

42. Baukal, C.E. and B. Gebhart, *A Review of Flame Impingement Heat Transfer Studies Part 2: Measurements.* Combustion Science and Technology, 1995. **104**(4-6): p. 359-385.

43. Fairweather, M., J. Kilham, and S. Nawaz, *Stagnation point heat transfer from laminar, high temperature methane flames.* International journal of heat and fluid flow, 1984. **5**(1): p. 21-27.

44. Omrane, A., et al. *Surface temperature measurement of flame spread using thermographic phosphors*. in *Proceedings of 7th IAFSS Symposium on Fire Safety Science*. 2002. IAFSS.

45. Janssens, M., *Fundamental thermophysical characteristics of wood and their role in enclosure fire growth*. 1991, Ghent University.

46. Alaruri, S., et al., *Mapping the surface temperature of ceramic and superalloy turbine engine components using laser-induced fluorescence of thermographic phosphor.* Optics and lasers in engineering, 1999. **31**(5): p. 345-351.

47. Allison, S.W., et al., *Monitoring permanent-magnet motor heating with phosphor thermometry.* Instrumentation and Measurement, IEEE Transactions on, 1988. **37**(4): p. 637-641.

48. Hubner, J.P., B.F. Carroll, and K.S. Schanze, *Heat-transfer measurements in hypersonic flow using luminescent coating techniques.* Journal of thermophysics and heat transfer, 2002. **16**(4): p. 516-522.

49. Salem, M., et al., *Heat flux measurements in stagnation point methane/air flames with thermographic phosphors.* Experiments in fluids, 2010. **49**(4): p. 797-807.

50. Wal, R.L.V., P.A. Householder, and T.W. Wright, *Phosphor thermometry in combustion applications.* Applied spectroscopy, 1999. **53**(10): p. 1251-1258.

51. Khalid, A.H. and K. Kontis, *Thermographic phosphors for high temperature measurements: principles, current state of the art and recent applications.* Sensors, 2008. **8**(9): p. 5673-5744.

52. Aldén, M., et al., *Thermographic phosphors for thermometry: a survey of combustion applications.* Progress in energy and combustion science, 2011. **37**(4): p. 422-461.

53. El-Mahallawy, F. and S.E.D. Habik, *Fundamentals and technology of combustion*. 2002: Elsevier.

54. Turns, S.R., *An introduction to combustion*. Vol. 287. 1996: McGraw-Hill New York.

55. Gaydon, A.G. and H.G. Wolfhard, *Flames: their structure, radiation and temperature*. 1979: Chapman & Hall London.

56. Warnatz, J.r., U. Maas, and R.W. Dibble, *Combustion: physical and chemical fundamentals, modeling and simulation, experiments, pollutant formation*. 2006: Springer.

57. Glassman, I. and R.A. Yetter, *Combustion, 2008*. Academic Press.

58. McAllister, S., J.-Y. Chen, and A.C. Fernandez-Pello, *Fundamentals of combustion processes*. 2011: Springer.

59. Bosschaart, K.J. and L.P.H. De Goey, *Detailed analysis of the heat flux method for measuring burning velocities.* Combustion and Flame, 2003. **132**(1): p. 170-180.

60. Bradley, J.N., *Flame and combustion phenomena.* 1969.

61. Fristrom, R.M. and A.A. Westenberg, *Flame structure, 1965*. McGraw-Hill.

62. Viskanta, R., et al., *Convective and radiative flame jet impingement heat transfer.* Int. J. Transport Phenom, 1998. **1**: p. 1-15.

63. Martin, H. *Heat and mass transfer between impinging gas jets and solid surfaces*. in *In: Advances in heat transfer. Volume 13. New York, Academic Press, Inc., 1977, p. 1-60.* 1977.

64. Milson, A., *Impinging jet flames*. 1972, Scheffield university.

65. Fairweather, M., J.K. Kilham, and S. Nawaz, *Stagnation point heat transfer from laminar, high temperature methane flames.* International journal of heat and fluid flow, 1984. **5**(1): p. 21-27.

66. Buyuk, E., *Heat transfer and flow structures around circular cylinders in cross flow.* Journal of Engineering and environmental science, 1999. **23**: p. 299-315.

67. Turns, S., *Thermal-fluid sciences: An integrated approach*. Vol. 1. 2006: Cambridge University Press.

68. Polat, S., et al., *Numerical flow and heat transfer under impinging jets: a review.* Annual Review of Heat Transfer, 1989. **2**(2).

69. Gray, W.A., J.K. Kilham, and R. Müller, *Heat transfer from flames.* NASA STI/Recon Technical Report A, 1976. **77**: p. 19244.

70. Zabetakis, M.G., *Flammability characteristics of combustible gases and vapors*. 1965, DTIC Document.

71. Baukal, C.E. and B. Gebhart, *A review of semi-analytical solutions for flame impingement heat transfer.* International journal of heat and mass transfer, 1996. **39**(14): p. 2989-3002.

72. Coffee, T.P. and J.M. Heimerl, *Transport algorithms for premixed, laminar steady-state flames.* Combustion and Flame, 1981. **43**: p. 273-289.

73. Popiel, C.O., T.H. van Der Meer, and C.J. Hoogendoorn, *Convective heat transfer on a plate in an impinging round hot gas jet of low Reynolds number.* International journal of heat and mass transfer, 1980. **23**(8): p. 1055-1068.

74. Kleijn, C.R., *Heat transfer from laminar impinging methane/air flames.* ASME-PUBLICATIONS-PVP, 2001. **424**: p. 259-270.

75. Rigby, J.R. and B.W. Webb, *An experimental investigation of diffusion flame jet impingement heat transfer*, in *Proceedings of the ASME/JSME thermal engineering joint conference*. 1995. p. 117-126.

76. Nawas, S., *Heat transfer from oxygen enriched methane falmes*. 1973 (PhD thesis), The University of Leeds.

77. Kays, W.M., M.E. Crawford, and B. Weigand, *Convective heat and mass transfer*. 2012: Tata McGraw-Hill Education.

78. Childs, P.R.N., J.R. Greenwood, and C.A. Long, *Review of temperature measurement.* Review of scientific instruments, 2000. **71**(8): p. 2959-2978.

79. Preston-Thomas, H., *The International Temperature Scale of 1990(ITS-90).* Metrologia, 1990. **27**(1): p. 3-10.

80. Bernhard, F., *Technische Temperaturmessung*. 2004: Springer DE.

81. Pflitsch, C., et al., *Sol–gel deposition of chromium doped aluminium oxide films (ruby) for surface temperature sensor application.* Chemistry of Materials, 2008. **20**(8): p. 2773-2778.

82. Seyfried, H., et al., *Laser-induced phosphorescence for surface thermometry in the afterburner of an aircraft engine.* Aiaa Journal, 2007. **45**(12): p. 2966-2971.

83. Williams, E.W. and H.B. Bebb, *Semiconductors and semimetals.* RK Willardson ed, 1972. **8**: p. 336.

84. Pankove, J.I., *Optical processes in semiconductors, 1971.* Dover Publications, New York.

85. Brübach, J., J. Janicka, and A. Dreizler, *An algorithm for the characterisation of multi-exponential decay curves.* Optics and Lasers in Engineering, 2009. **47**(1): p. 75-79.

86. Klein, L., *Sol-gel processing of silicates.* Annual Review of Materials Science, 1985. **15**(1): p. 227-248.

87. Bahlawane, N., *Novel sol-gel process depositing α-Al< sub> 2</sub> O< sub> 3</sub> for the improvement of graphite oxidation-resistance.* Thin Solid Films, 2001. **396**(1): p. 126-130.

88. Pflitsch, C., R. Siddiqui, and B. Atakan, *Phosphorescence properties of sol–gel derived ruby measured as functions of temperature and Cr3+ content.* Applied Physics A, 2008. **90**(3): p. 527-532.

89. Koechner, W., *Solid-state laser engineering, 1999.* Spriner-Verlag, Berlin-Heidelberg, New York.

90. Brübach, J., J. Feist, and A. Dreizler, *Characterization of manganese-activated magnesium fluorogermanate with regards to thermographic phosphor thermometry.* Measurement Science and Technology, 2008. **19**(2): p. 025602.

91. Seat, H.C. and J.H. Sharp, *Dedicated temperature sensing with c-axis oriented single-crystal ruby (Cr 3+: Al 2 O 3) fibers: temperature and strain dependences of R-line fluorescence.* Instrumentation and Measurement, IEEE Transactions on, 2004. **53**(1): p. 140-154.

92. Kline, S.J. and F.A. McClintock, *Describing uncertainties in single-sample experiments.* Mechanical engineering, 1953. **75**(1): p. 3-8.

93. Hemrick, J.G., et al., *Thermal conductivity of alumina measured with three techniques.* Journal of testing and evaluation, 2003. **31**(5): p. 438-442.

94. Goodwin, D.G., *An open-source, extensible software suite for CVD process simulation.* Chemical Vapor Deposition XVI and EUROCVD, 2003. **14**(40): p. 2003-08.

95. Al-Baghdadi, M., *Hydrogen–ethanol blending as an alternative fuel of spark ignition engines.* Renewable Energy, 2003. **28**(9): p. 1471-1478.

96. Kwok, L., *Heat transfer characteristics of slot and round premixed impinging flame jets.* Experimental Heat Transfer, 2003. **16**(2): p. 111-137.

97. Sinha, A. and S. Chander. *Numerical investigation of flame jet impingement on a flat plate*. in *proceedings of the 37th national conference on fluid mechanics and fluid power*. Decmber 16-18, 2010.

98. Egolfopoulos, F.N., D.X. Du, and C.K. Law. *A study on ethanol oxidation kinetics in laminar premixed flames, flow reactors, and shock tubes*. in *Symposium (International) on Combustion*. 1992. Elsevier.

99. Gülder, O.L., *Laminar burning velocities of methanol, ethanol and isooctane-air mixtures*, in *Symposium (international) on combustion*. 1982, Elsevier. p. 275-281.

100. Elmnefi, M.S., *New Optical Method for Heat Flux Measurements in Stagnation Point Laminar Methane/Air Flames and Hydrogen/Methane/Air Flames using Thermographic Phosphors*. 2010, Duisburg, Essen, Univ., Diss., 2010.

101. Remie, M., et al., *Analysis of the heat transfer of an impinging laminar flame jet.* International journal of heat and mass transfer, 2007. **50**(13): p. 2816-2827.

102. Qiao, L., et al., *Burning Velocities and Flammability Limits of Premixed Methane/Air/Diluent Flames in Microgravity*. 2008.

103. Sparrow, E.M. and B.J. Lovell, *Heat transfer characteristics of an obliquely impinging circular jet.* Journal of Heat Transfer, 1980. **102**(2): p. 202-209.

Appendix Mechanical Drawings

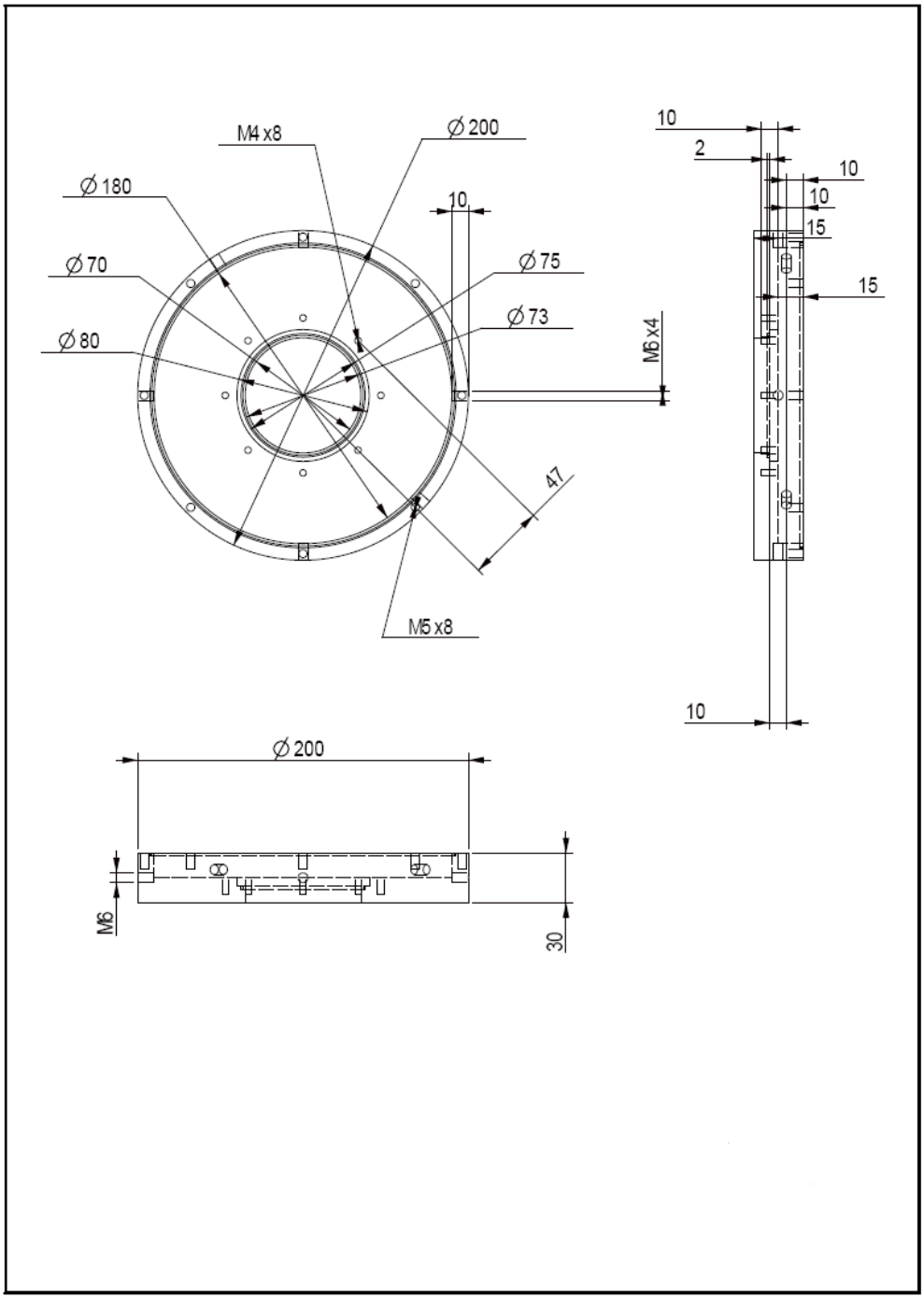

The water streamed Disc (Flat plate experimental-setup)

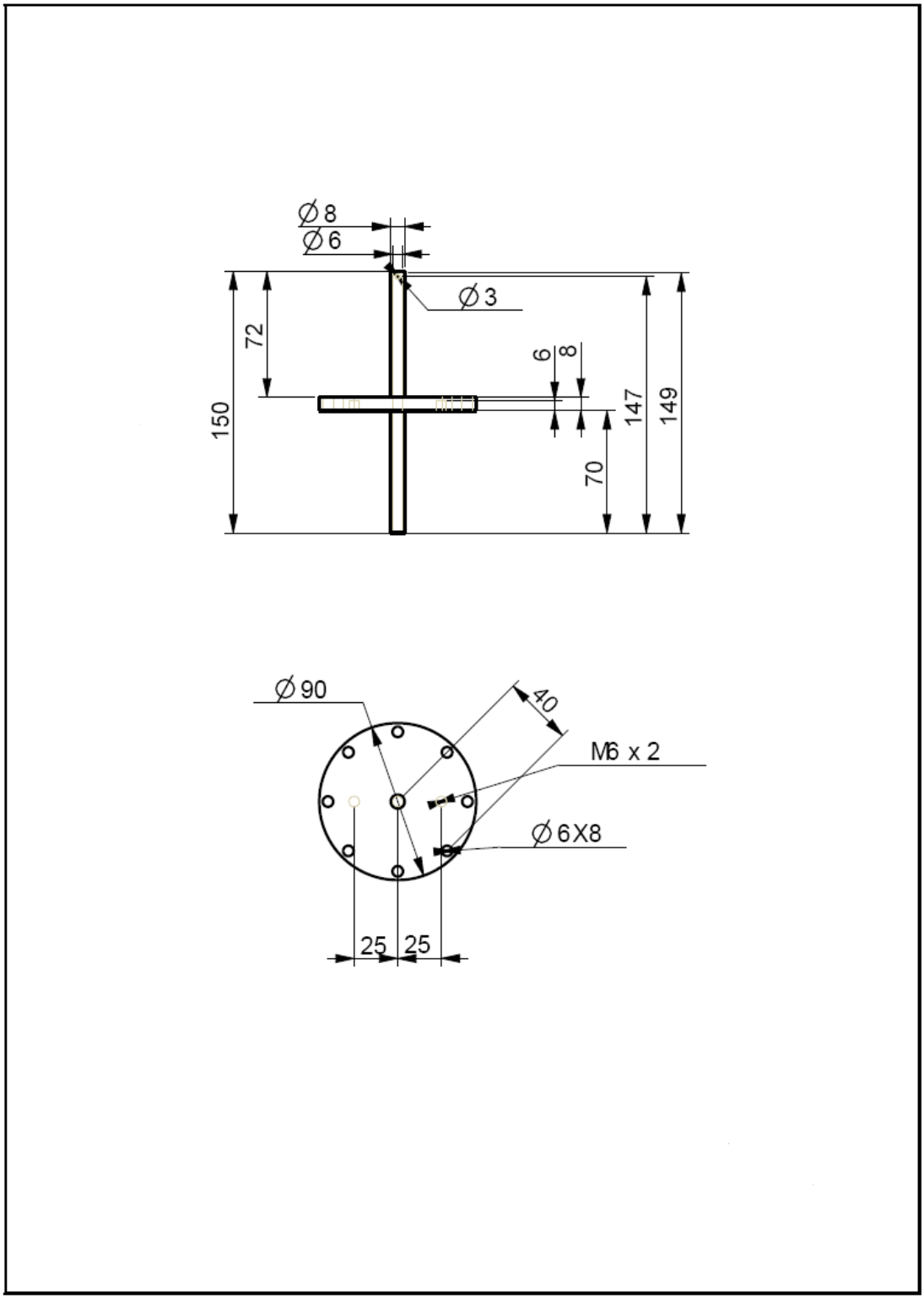

Water inlet stainless-steel flange (cylindrical surface experimental-setup)

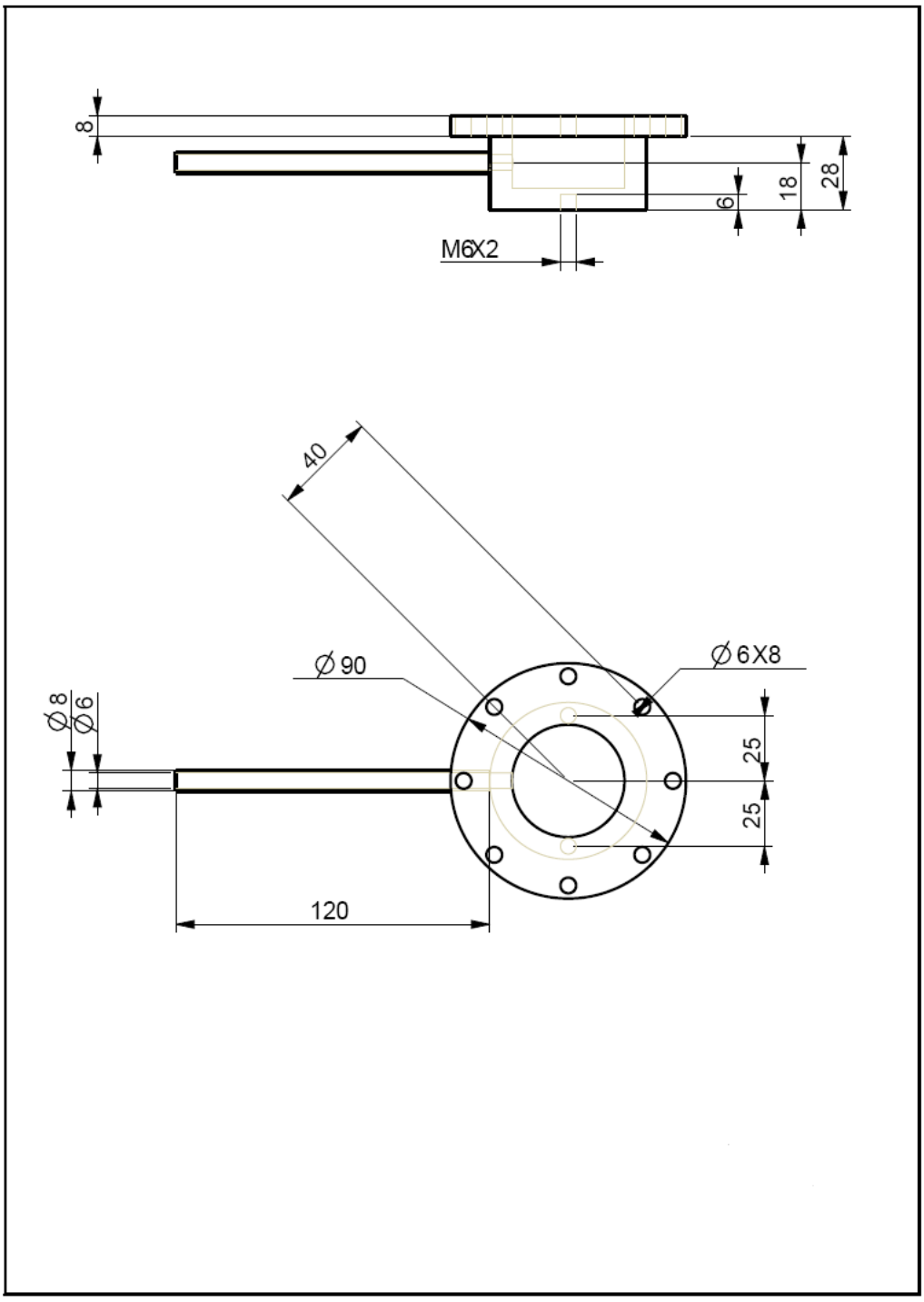

Water outlet stainless-steel flange (cylindrical surface experimental-setup)

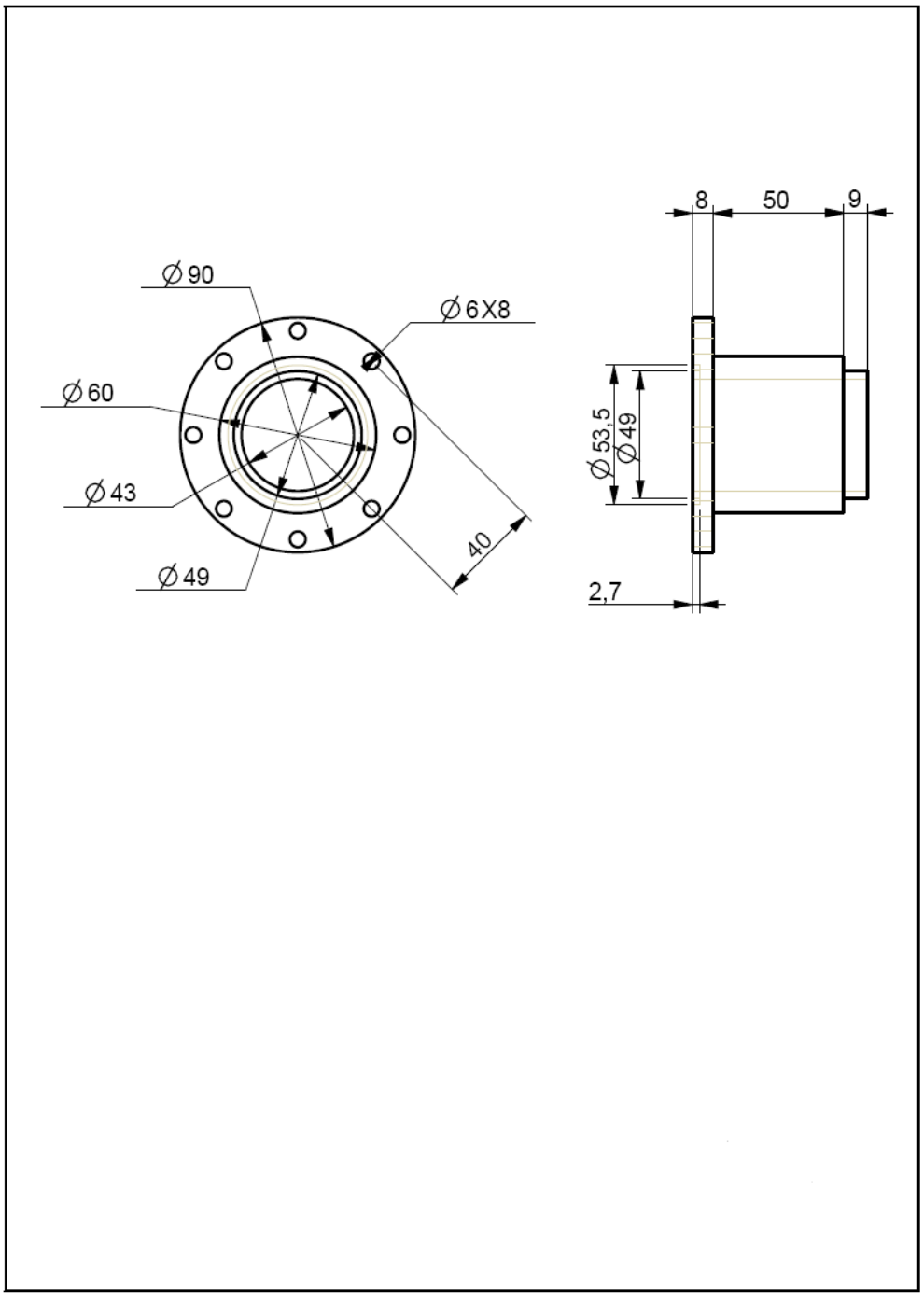

Brass flange adaptor for ceramic pipe (cylindrical surface experimental-setup)

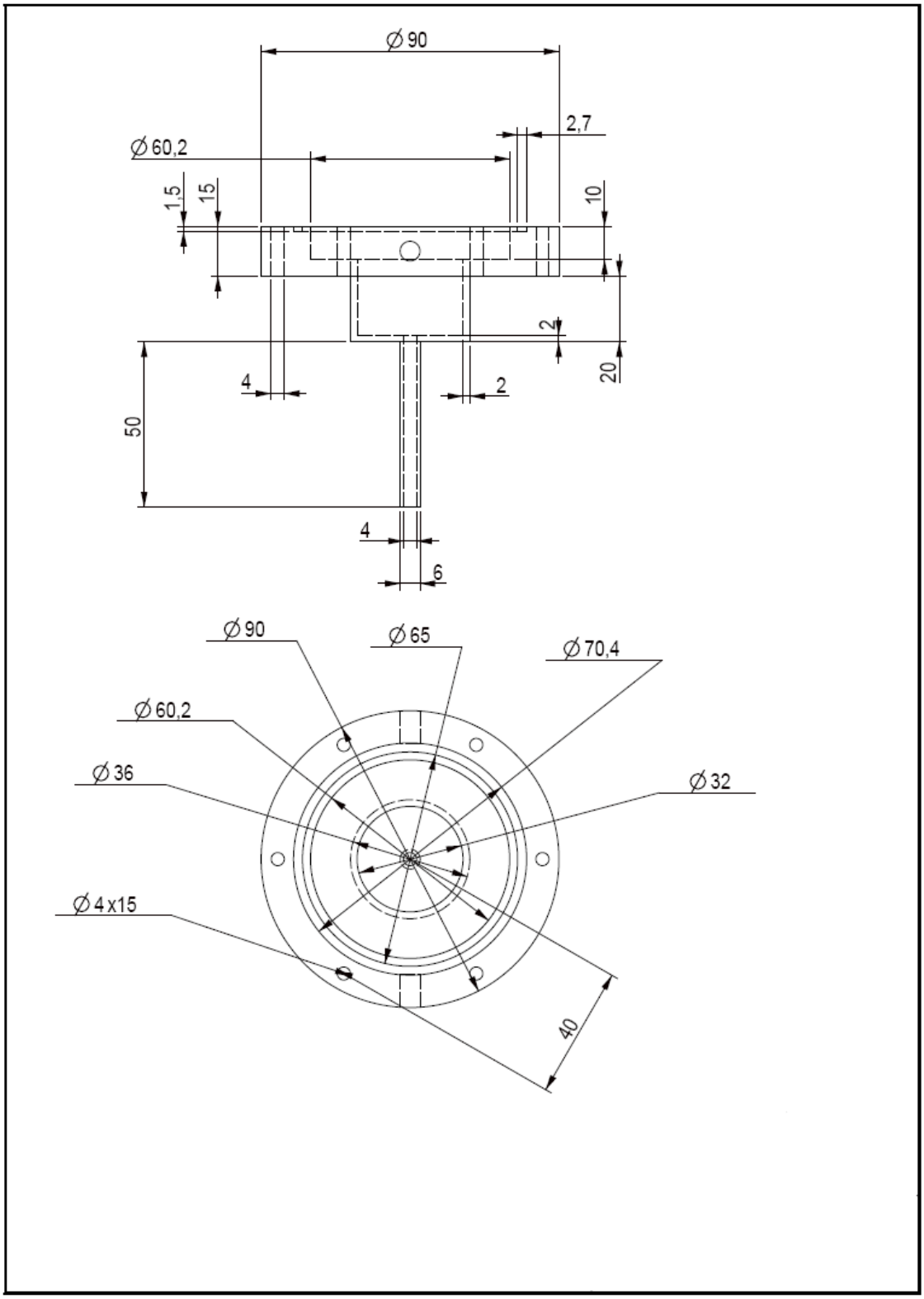

The flat burner housing

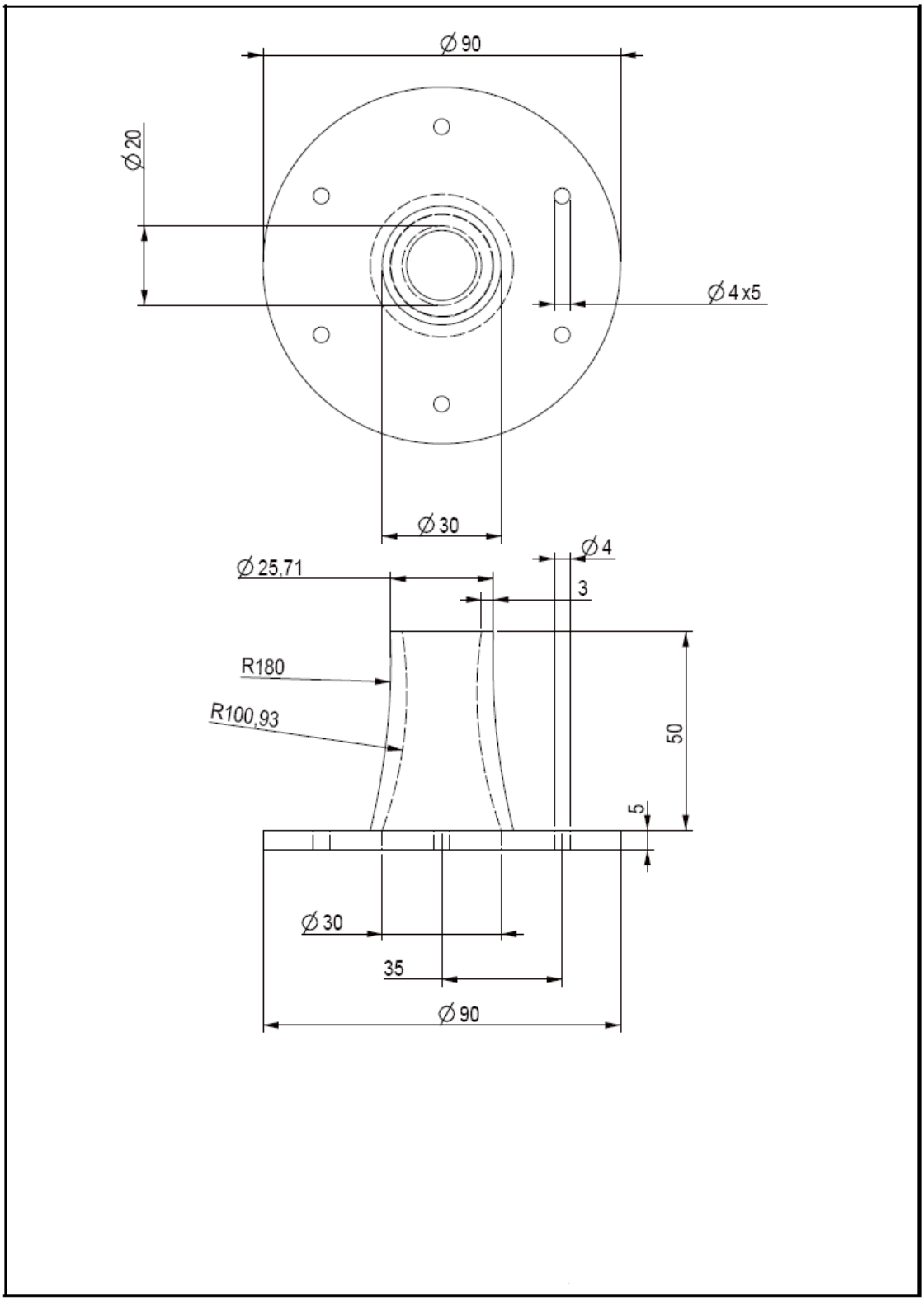

The nozzle burner

Curriculum Vitae

Der Lebenslauf ist in der Online-Version aus Gründen des Datenschutzes nicht enthalten.

Curriculum Vitae

Der Lebenslauf ist in der Online-Version aus Gründen des Datenschutzes nicht enthalten.

Curriculum Vitae

Der Lebenslauf ist in der Online-Version aus Gründen des Datenschutzes nicht enthalten.